

**ISTANBUL TECHNICAL UNIVERSITY ★ GRADUATE SCHOOL**

**MULTI-MODAL NEUROIMAGING DATA PREDICTION:  
ESTIMATION OF CONNECTIONAL BRAIN TEMPLATE AND  
MULTIGRAPH  
CLASSIFICATION WITH APPLICATION TO GENDER FINGERPRINTING**



**Ph.D. THESIS**

**Nada CHAARI**

**Department of Management Engineering**

**Management Engineering Program**

**NOVEMBER 2021**



**ISTANBUL TECHNICAL UNIVERSITY ★ GRADUATE SCHOOL**

**MULTI-MODAL NEUROIMAGING DATA PREDICTION:  
ESTIMATION OF CONNECTIONAL BRAIN TEMPLATE AND  
MULTIGRAPH  
CLASSIFICATION WITH APPLICATION TO GENDER FINGERPRINTING**

**Ph.D. THESIS**

**Nada CHAARI  
(507162015)**

**Department of Management Engineering**

**Management Engineering Program**

**Thesis Advisor: Prof. Dr. Hatice CAMGÖZ AKDAĞ  
Thesis Co-Advisor: Assist. Prof. Dr. Islem REKİK**

**NOVEMBER 2021**



**İSTANBUL TEKNİK ÜNİVERSİTESİ ★ LİSANSÜSTÜ EĞİTİM ENSTİTÜSÜ**

**ÇOKLU MODAL NÖROGÖRÜNTÜLEME VERİ TAHMİNİ:  
BAĞLANTILI BEYİN ŞABLONUNUN TAHMİNİ VE CİNSİYET  
PARMAK İZİ UYGULAMASI İLE ÇOKLU GRAFİK SINIFLANDIRMA**

**DOKTORA TEZİ**

**Nada CHAARI  
(507162015)**

**İşletme Mühendisliği Anabilim Dalı**

**İşletme Mühendisliği Programı**

**Tez Danışmanı: Prof. Dr. Hatice CAMGÖZ AKDAĞ  
Eş Danışman: Assist. Prof. Dr. Islem REKİK**

**KASIM 2021**



Nada CHAARI, a Ph.D. student of ITU Graduate School student ID 507162015, successfully defended the dissertation entitled “MULTI-MODAL NEUROIMAGING DATA PREDICTION: ESTIMATION OF CONNECTIONAL BRAIN TEMPLATE AND MULTIGRAPH CLASSIFICATION WITH APPLICATION TO GENDER FINGERPRINTING”, which she prepared after fulfilling the requirements specified in the associated legislations, before the jury whose signatures are below.

**Thesis Advisor :**     **Prof. Dr. Hatice CAMGÖZ AKDAĞ**     .....  
Istanbul Technical University

**Co-advisor :**         **Assist. Prof. Dr. Islem REKİK**     .....  
Istanbul Technical University

**Jury Members :**     **Prof. Dr. Başar ÖZTAYŞI**     .....  
Istanbul Technical University

**Prof. Dr. Sezi ÇEVİK ONAR**     .....  
Istanbul Technical University

**Prof. Dr. Selim ZAİM**     .....  
Istanbul Sabahattin Zaim University

**Doç. Dr. Tuncay ÖZCAN**     .....  
Istanbul Technical University

**Dr. Öğr. Üyesi Adnan ÇORUM**     .....  
Bahçeşehir University

**Date of Submission : 10 October 2021**

**Date of Defense : 11 November 2021**



## **FOREWORD**

This report is my thesis for the doctorate degree of management engineering program in Istanbul Technical University. The research is conducted at BASIRA (Brain And Signal Research And Analysis) Laboratory and funded by TÜBİTAK (The Scientific and Technological Research Council of Turkey) under the 2023 project entitled ‘A Devising Reproducible PRedictive Intelligence in MEDicine (RePRIME) for Early Neurological Disorder Diagnosis from Minimal Medical Data’ between June 2020 and September 2021. I would like to express my sincere gratitude to my both supervisors Asst. Prof. Islem REKİK and Dr. Prof. Hatice CAMGÖZ AKDAĞ for their great support and guidance during my research process, their invaluable feedbacks on every step of my research project, and their continuous encouragement during hard times of my research.

In truth, I could not have achieved my current level of success without my mother Maha, my sister Hana, and my little brother Aziz who supported me with love, understanding, and absolute patience during these months while I was working on my graduation project. A special thanks to my soulmate Selman for his priceless and continuous support during my long Ph.D. journey.

NOVEMBER 2021

Nada CHAARI  
(Ph.D student)



## TABLE OF CONTENTS

	<u>Page</u>
<b>FOREWORD</b> .....	vii
<b>TABLE OF CONTENTS</b> .....	ix
<b>ABBREVIATIONS</b> .....	xiii
<b>LIST OF TABLES</b> .....	xv
<b>LIST OF FIGURES</b> .....	xvii
<b>SUMMARY</b> .....	xxix
<b>ÖZET</b> .....	xxxiii
<b>1. INTRODUCTION</b> .....	<b>1</b>
1.1 Gender Difference and Brain Connectivity .....	1
1.2 Connectional Fingerprint of Heterogeneous Multimodal Data .....	3
1.3 Graph Theory, Connectomes, and Multigraph .....	4
1.3.1 Multigraph integration .....	6
1.3.2 Multigraph classification.....	7
1.4 Contributions and Road-map.....	9
<b>2. LITERATURE REVIEW</b> .....	<b>15</b>
2.1 Related Works of Integration Models.....	15
2.2 Related Works of Multigraph Classification Methods .....	17
2.3 Related Works of Single-view and Multi-view Integration Methods.....	20
<b>3. METHODOLOGY</b> .....	<b>25</b>
3.1 Proposed Multi-View Clustering and Fusion Network (MVCF-Net) .....	25
3.1.1 MVCF-Net overview .....	25
3.1.2 Feature extraction and similarity networks construction .....	26
3.1.3 Multi-view clustering using optimization manifolds .....	26
3.1.4 Individual-based non-linear fusion of connectional brain network views .....	32
3.1.5 Linear fusion .....	33
3.1.6 Evaluation strategies .....	33
3.1.6.1 Evaluation strategy of connectional brain template representativeness.....	35
3.1.6.2 Evaluation strategy of connectional brain template discriminability .....	36
Identification of top discriminative ROIs using the estimated CBTs .....	36
Reproducibility of top discriminative ROIs.....	37
3.2 Multigraph Integration and Classifier Networks (MICNet) .....	38
3.2.1 MICNet overview.....	38
3.2.2 Problem definition .....	40
3.2.3 Multigraph integration and thresholding step.....	42
3.2.4 Multigraph classification.....	44
3.2.4.1 Classification with hierarchical embedding.....	44
3.2.4.2 Graph convolution networks (GCN) classifier .....	46

3.2.4.3 Loss.....	46
3.3 CBT Estimation Methods.....	47
3.3.1 Single-graph fusion methods.....	48
3.3.2 Multigraph fusion methods.....	51
3.3.3 CBT evaluation measures.....	53
3.3.3.1 CBT centeredness test.....	54
3.3.3.2 CBT discriminativeness reproducibility test.....	54
3.3.3.3 CBT node-wise similarity comparison.....	57
Hubness behaviour test.....	57
Segregation behaviour test.....	60
Integration behaviour test.....	61
3.3.3.4 CBT graph-edit distances-based comparison.....	61
3.3.3.5 CBT global-level similarity comparison.....	63
<b>4. RESULTS AND DISCUSSIONS.....</b>	<b>65</b>
4.1 Results and Discussion of Our Proposed MVCF-Net Method.....	66
4.1.1 Experimental results.....	66
4.1.1.1 Evaluation dataset and preprocessing pipeline.....	66
4.1.1.2 Method parameters.....	67
4.1.1.3 Methods comparison.....	69
4.1.1.4 CBT representativeness and centeredness.....	69
4.1.1.5 CBT discriminability.....	71
4.1.2 Discussion.....	75
4.1.2.1 Parameters impacts.....	75
4.1.2.2 CBT representativeness and centeredness.....	76
4.1.2.3 CBT discriminability.....	78
4.1.2.4 Limitations and future directions.....	81
4.2 Results and Discussion of Our Proposed MICNet Method.....	82
4.2.1 Experimental results.....	82
4.2.1.1 Evaluation dataset and preprocessing pipeline.....	82
4.2.1.2 Method parameters.....	83
4.2.1.3 Methods comparison.....	83
4.2.1.4 Classification performance.....	84
4.2.2 Discussion.....	84
4.2.2.1 Quantitative analysis.....	85
4.2.2.2 Qualitative analysis.....	86
4.2.2.3 Limitation and future directions.....	91
4.3 Results and Discussion of Our Comparative Study of Connectional Brain Templates in Network Neuroscience.....	93
4.3.1 Experimental results.....	93
4.3.1.1 Evaluation datasets.....	93
4.3.1.2 Parameter settings.....	94
4.3.1.3 Evaluation strategies.....	95
4.3.2 Discussion.....	95
4.3.2.1 CBT centeredness test.....	95
4.3.2.2 CBT discriminativeness reproducibility test.....	96
4.3.2.3 CBT node-wise similarity comparison.....	98
4.3.2.4 CBT global-level similarity test.....	104
4.3.2.5 CBT distance-based similarity test.....	106

4.3.2.6 Limitation and future directions .....	107
<b>5. CONCLUSIONS.....</b>	<b>111</b>
<b>REFERENCES.....</b>	<b>115</b>
<b>APPENDICES.....</b>	<b>127</b>
APPENDIX A: .....	129
<b>CURRICULUM VITAE.....</b>	<b>135</b>





## ABBREVIATIONS

<b>AD</b>	: Alzheimers disease
<b>ADNI</b>	: Alzheimer’s Disease Neuroimaging Initiative
<b>CBT</b>	: Connectional Brain Template
<b>CFs</b>	: Connectional Features
<b>CMN</b>	: Cortical morphological network
<b>cMGI-Net</b>	: cluster-based Multi-Graph Integrator Networks
<b>CNN</b>	: Convolutional Neural Network
<b>CMs</b>	: Centrality Measures
<b>DiffPool</b>	: Differentiable graph Pooling module
<b>DGN</b>	: Deep Graph Normalizer Network
<b>GCN</b>	: Graph Convolutional Network
<b>GDL</b>	: Geometric Deep Learning
<b>GED</b>	: Graph Edit Distance
<b>GNN</b>	: Graph Neural Network
<b>GSP</b>	: Genomics Superstruct Project
<b>GT</b>	: Ground Truth
<b>KL</b>	: Kullback-Leibler
<b>KNN</b>	: K-Nearest Neighbors
<b>LH</b>	: Left Hemisphere
<b>LMCI</b>	: Late Mild Cognitive Impairment
<b>MKL</b>	: Multiple Kernel Learning
<b>MKML</b>	: Multi-Kernel Manifold Learning
<b>MRI</b>	: Magnetic Resonance Imaging
<b>MVCF-Net</b>	: Multi-View Clustering and Fusion Network
<b>NAG-FS</b>	: Network Atlas-Guided Feature Selection
<b>netNorm</b>	: network Normalizer
<b>MICNet</b>	: Multigraph Integration and Classifier Network
<b>PET</b>	: Positron Emission Tomography
<b>rfMRI</b>	: resting-state functional Magnetic Resonance Imaging
<b>RH</b>	: Right Hemisphere
<b>ROI</b>	: Regions Of Interest
<b>RNN</b>	: Recurrent Neural Network
<b>SCA</b>	: SNF-Clustering-Average
<b>SIMLR</b>	: Single-cell Interpretation via Multikernel Learning
<b>SM-netFusion</b>	: Supervised Multi-topology network cross-diffusion
<b>SNF</b>	: Similarity Network Fusion
<b>SVM</b>	: Support Vector Machine



## LIST OF TABLES

	<u>Page</u>
<b>Table 3.1</b> : Major mathematical notations used in this paper.....	28
<b>Table 3.2</b> : MVCF-Net Algorithm: Joint Multi-View Network Clustering and Fusion.....	34
<b>Table 3.3</b> : Major mathematical notations used in this paper. ....	40
<b>Table 4.1</b> : Data distribution of female/male dataset. ....	67
<b>Table 4.2</b> : Matching rate in % between the top 15 discriminative ROIs distinguishing between male and female populations identified by (i) MKL and (ii) the difference between the estimated CBTs by SNF-Clustering-Average (SCA) and our method for the right and left hemispheres (RH and LH).....	72
<b>Table 4.3</b> : Matching rate in % between the top 20 discriminative ROIs distinguishing between male and female populations identified by (i) MKL and (ii) the difference between the estimated CBTs by SCA and our method for the right and left hemispheres (RH and LH). ....	75
<b>Table 4.4</b> : <i>Data description of female/male distributions</i> .....	83
<b>Table 4.5</b> : <i>Comparing the classification performance metrics by our proposed method (MICNet) and benchmark methods for gender classification. Our model MICNet is represented by our integration and our classifier (DIFF). The benchmark methods used for comparison include different integration techniques and classifiers. The integration methods are: similarity network fusion technique (SNF) [1], normalization method (netNorm) [2], simple average (average), weighted linear average (linear) and our integration. The classifiers are graph convolutional networks (GCN) [3] and the classification block (DIFF) that we integrated in our model. All models include thresholding as mentioned in the above sections.</i> ....	85
<b>Table 4.6</b> : Data distribution for M/F and AD/LCMI datasets. Each view in the connectomic datasets contains 35 nodes, and 4 views are fully connected. ....	94
<b>Table 4.7</b> : Matching rate in % between the top $k$ (10, 15, 20, and 20) discriminative ROIs distinguishing between AD and LMCI populations, and between male and female populations identified by (i) MKL [4] and CBT-based single-view fusion methods and (ii) MKL [4] and CBT-based multigraph fusion methods for the right and left hemispheres (RH and LH).....	98



## LIST OF FIGURES

	<u>Page</u>
<b>Figure 1.1</b> : <i>Brain graph analysis. From confusing messy to neat organisation.</i> .....	5
<b>Figure 1.2</b> : <i>Brain graph as a matrix (connectome).</i> .....	5
<b>Figure 1.3</b> : <i>Diagram of conventional multigraph classification and integration tasks. a) Given a multigraph, typical classification methods including [5] aims to concatenate the multiple vectorized views. The stacked feature vectors are fed into an independent classification model. b) Proposed method integrates the views of the same sample into a single-view graph. Next, the fused multigraph is fed into the classification block. Both blocks work in an end-to-end manner which makes the integration block contributes to the discriminativeness and the global classification performance of the model.</i> .....	9
<b>Figure 1.4</b> : <i>Roadmap of the thesis work</i> .....	14
<b>Figure 3.1</b> : <i>Pipeline of the proposed MVCF-Net framework for connectional brain template (CBT) estimation using multi-view brain networks. First, for a given brain network view and for each subject, we extract features by vectorizing the upper off-diagonal part of each brain connectivity matrix. Second, we compute the Euclidian distance between each pair of subjects using their corresponding features vectors to eventually derive a multi-view similarity matrix. Third, we perform multi-view network clustering based on manifold optimization method [6] to partition subjects into shared and differential clusters across views. Fourth, we linearly average all brain networks in each cluster as they lie close to each other, producing local CBTs. Next, for each cluster, we non-linearly fuse its local CBTs across each view using similarity network fusion (SNF) since the local CBTs might lie far from each other. This produces a cluster-specific CBT. Last, we average all cluster-specific CBTs across all clusters, thereby generating the global population CBT.</i> .....	27

**Figure 3.2** : *Multi-view clustering using manifold optimization.* For each view  $m$  lying on a manifold  $\mathcal{M}_m$ , first, we calculate pairwise distance matrix between subjects. Second, for each view  $m$ , we derive the similarity matrices using K-nearest neighbor (KNN) method and compute the Laplacian matrix. Then, for each view  $m$ , we partition all subjects into clusters while preserving their alignment using multi-view spectral clustering. Thus, both consistent and differential clusters can be identified simultaneously. To do that, we solve the optimization problem for each view:  $\min \text{trace}(\mathbf{U}_m^T \mathbf{L} \mathbf{U}_m)$  where  $\mathbf{U}_m$  is a vector representing the initial partition of  $N$  subjects into  $N_c$  cluster. The optimization process includes three steps: first we project the negative gradient on the tangent vector to the manifold  $m$  and we obtain the direction  $\eta_m$ . Second, we update  $\mathbf{U}_m$  by adding a multiple of this direction to its previous measurement. Third, we retract the new  $\mathbf{U}_{m+1}$  to the manifold using single value decomposition. Finally, as  $\mathbf{U}$  converges, we compute k-means clustering to obtain the final label vector partitioning the  $N$  subjects into  $N_c$  clusters for each network view. ... 30

**Figure 3.3** : *Identification of regions of interest (ROIs) scores using MVCF-Net method.* First, we calculate the absolute difference between two estimated connectional brain templates (CBTs) to generate the absolute difference matrix. Secondly, we aggregate the column elements of each row in the absolute difference matrix to produce a score vector assigning the weight for each ROI. Finally, we decreasingly rank the elements of score vector to get the top discriminative ROIs. .... 37

**Figure 3.4** : *Identification of the top discriminative ROIs using multiple kernel learning (MKL).* First, we linearize the multi-view brain connection networks for training and testing brain networks through the vectorization of the upper triangular part of each population matrices to generate a feature vector for each brain network. Second, for each view  $m$ , we apply MKL based on support vector machine (SVM) to obtain a weight vector  $\mathbf{x}_m$  quantifying the discriminability of each brain feature (i.e., brain connectivity between two anatomical regions of interest (ROIs)). Next, by summing the weight vectors  $x_m$  across views, we obtain the total weight vector  $\mathbf{x}$  for a particular ROI. We then use anti-linearization to transform the weight vector into a matrix where each element represents the connectivity weight between two ROIs. Specifically, anti-linearization is the inverse of features vectorization where the weight vector represents the upper triangular part of the resulting symmetrical connectivity matrix. By aggregating the columns of the resulting matrix, we obtain the score vector denoting the discriminative power of each ROI. Finally, we rank brain ROIs according to their highest scores... 39

- Figure 3.5** : *Overview of our multigraph integration and classification (MICNet) architecture.* MICNet performs classification of multigraphs with heterogeneous views. We first integrate a multigraph at a subject-level. The integration block extracts single-view graphs from the original multigraphs. These single-view graphs contain the most relevant edge attributes. Next, we introduce the outputs of the integration block to a subject-specific thresholding filter. This step generates binary matrices representing single-view graphs with binary edge attributes. This step selects the connections having most relevant connectivity weights, thereby emphasizing the most discriminative and representative edges used as subject fingerprints. We feed these graphs to a GNN-based classification architecture which performs several graph convolutions to get final prediction. We transform the single-view graph through a sequence of embedding and pooling layers into predicted labels..... **41**
- Figure 3.6** : *Multigraph integration pipeline.* For a given multigraph, this block consists in the fusion of the multigraph views at a subject-level. We compute the subject-level integrated template by stacking different convolution operations. At each layer, we perform a multiplication of a multigraph tensor convolution output and the resulting tensor of the previous layer. After computations of all layers, we calculate the mean of the resulting tensor over the channels. The resulting tensor represents a single view-graph obtained after integration of the original views. .... **42**
- Figure 3.7** : *Illustration of our proposed MICNet graph classification model with one pooling layer.* We initialize  $\mathbf{A}^{[0]}$  as the adjacency matrix of the graph obtained after thresholding step and  $\mathbf{H}^{[0]}$  as an identity matrix  $\mathbf{I}_n$ . On one hand, we run a GNN-based architecture to obtain the embedding tensor  $\mathbf{Z}^{[0]}$ . Then, we multiply  $\mathbf{Z}^{[0]}$  by  $\mathbf{A}^{[0]}$  to obtain the new adjacency matrix  $\mathbf{A}^{[1]}$ . On the other hand, we run another GNN-based architecture to get the assignment matrix  $\mathbf{S}^{[0]}$  containing the new nodes representation in the new clusters. Next, we multiply  $\mathbf{Z}^{[0]}$  by the softmax output of  $\mathbf{S}^{[0]}$  to get the new nodes embedding matrix  $\mathbf{H}^{[1]}$ . We run a separated GNN-based architecture using  $\mathbf{Z}^{[1]}$  and  $\mathbf{H}^{[1]}$  to obtain the updated output embeddings tensor of nodes  $\mathbf{Z}^{[1]}$ . This whole process represents the 1<sup>st</sup> pooling layer and it is repeated  $n_p$  times. After the final layer computations, we use all the embedding tensors  $\{\mathbf{Z}^{[i]}\}_{i=0}^{n_p}$  to classify the graph using a dedicated GNN-based architecture. .... **47**
- Figure 3.8** : *The schema illustrates connectional brain templates (CBTs) estimated by a) single-graph fusion methods for a given population of single-view brain networks: network atlas-guided feature selection (NAG-FS) [7], similarity network fusion (SNF) [1] and supervised multi-topology network cross-diffusion (SM-netFusion) [8]; and b) multi-graph integration methods for a population of multi-view connectomic brain data: multi-view networks normalizer (netNorm) [2], SNF-Clustering-Average (SCA) [9], multi-view clustering and fusion (MVCF-Net) [10], cluster-based multi-graph integrator networks (cMGI-Net) [11]. .... **49***

<b>Figure 3.9</b>	: Diagram illustrating the criteria used to evaluate the performance of the connectional brain templates generated for single-view graph integration methods and multi-view graphs fusion methods. This includes first graph centeredness using Frobenius distance, second the graph-derived biomarker reproducibility where we identify the overlap of top $k$ discriminative nodes (ROIs) computed by the graph fusion methods and by an independent biomarker selection method, third the global-level similarity using both modularity and global efficiency measures, fourth the graph distance-based similarity where we compute Hamming and Jaccard distances. Finally, we include the graph node-wise similarity where we evaluate three behavior for the graph: integration behavior using participation coefficient, segregation behavior using local efficiency, and hubness behavior using the following centrality metrics: PageRank [12], Katz centrality [13], node strength [14], random-walk centrality [15], information centrality [16], Laplacian centrality [17], eigenvector centrality [18], and betweenness centrality [19].	55
<b>Figure 3.10</b>	: Analysis diagram illustrating the types of comparative study to evaluate single-view and multigraph fusion methods. We conduct method-based analysis where we evaluate the CBTs generated by the fusion methods against the ground truth using frobenius distance, centrality metrics, Kullback-Leibler divergence, modularity, local efficiency, and global efficiency measures. We also conduct ROIs-based analysis to evaluate the CBTs at the node-scale, where we recompute both centrality metrics and local efficiency, and we add the participation coefficient. Lastly, we include method-to-method analysis using a pairwise comparison between graph fusion methods, where we compute three measures: KL-divergence, Hamming distance and Jaccard distance.	60
<b>Figure 4.1</b>	: Average Frobenius distance between the estimated CBT by MVCF-Net and all CMNs in the left (LH) and right (RH) hemispheres as we vary the number of selected neighbors for KNN.	68
<b>Figure 4.2</b>	: Average Frobenius distance between the estimated CBT by SNF-Clustering-Average (SCA) [9] and all CMNs in the left (LH) and right (RH) hemispheres as we vary the number of selected neighbors for KNN.	69
<b>Figure 4.3</b>	: Average Frobenius distance between the estimated morphological CBT and all CMNs in the left (LH) and right (RH) hemispheres using our method MVCF-Net in comparison with SNF-Clustering-Average (SCA) [9] as we vary the number of selected views constructing the CMNs from 2 to 4 views. Each bar represents the average Frobenius distance and its standard deviation of all possible combinations for a given number of views.	70

<b>Figure 4.4</b>	: Average Pearson correlation between the estimated morphological CBT and all CMNs in the left (LH) and right (RH) hemispheres using our method MVCF-Net in comparison with SNF-Clustering-Average (SCA) [9] as we vary the number of selected views constructing the CMNs from 2 to 4 views. Each bar represents the average Pearson correlation and its standard deviation of all possible combinations for a given number of views..	<b>70</b>
<b>Figure 4.5</b>	: Evaluation of the normalized Frobenius distance between the estimated morphological CBT and all multi-view brain networks for male and female populations in left and right hemispheres (LH and RH) using our method MVCF-Net in comparison with SNF-Clustering-Average (SCA) [9].....	<b>73</b>
<b>Figure 4.6</b>	: Evaluation of Pearson correlation between the estimated morphological CBT and all multi-view brain networks for male and female population in left and right hemispheres (LH and RH) using our method MVCF-Net in comparison with SNF-Clustering-Average (SCA) [9].....	<b>73</b>
<b>Figure 4.7</b>	: Top 5 discriminative regions of interest (ROIs) in left (LH) and right (RH) hemispheres distinguishing between gender populations revealed by computing the absolute difference between male and female CBTs by MVCF-Net. ....	<b>77</b>
<b>Figure 4.8</b>	: <i>Evaluating the discriminability of the estimated population specific connectional brain template by MVCF-Net.</i> We identify the top 15 discriminative ROIs using multiple-kernel learning (MKL) and the absolute difference between male and female CBTs in the right and left hemispheres (RH and LH). For each of top identified 15 ROIs, we display their discriminative weight. ....	<b>78</b>
<b>Figure 4.9</b>	: <i>a) Testing the effect of normalization on the accuracy performance using 5 folds cross-validation. b)Testing the effect of thresholding on the accuracy performance using 5 fold cross-validation.</i> For a) and b), the left and right barplots display the accuracy obtained using left and right hemisphere datasets, respectively. In each plot of a), the left bar shows the result obtained by our model after normalization of the data using min-max technique. The right bar shows the results obtained by our model without data normalization. In each plot of b), the bars correspond to three types of filters: mean thresholding, median thresholding and without thresholding. The thresholding step was applied between integration and classification blocks of our model. These barplots point out the contribution of the different thresholding strategies to the global model accuracy for both datasets (left and right hemispheres). ....	<b>87</b>

**Figure 4.10** : a) Average connectivity matrices across all the subjects of each class after multigraph integration with the respective top 5 connectivity weights using MICNet on left hemisphere dataset. b) Average connectivity matrices across all the subjects of each class after multigraph integration with the respective top 5 connectivity weights using MICNet on right hemisphere dataset. For a) and b), the two figures at the left and the two figures at the right correspond to the male and female class subjects, respectively. Each heatmap is obtained by computing the average of each connectivity of all subjects for a specific class after integration block. The heatmaps reflect the distributions of the assigned weights by the multigraph integration step. Circular graphs display the most important connectivities for each class based on the edge weights after integration. .... 89

**Figure 4.11** : Region-wise distribution of the learned discriminative weights in MICNet for both datasets (right hemisphere and left hemisphere). We extracted these weights from the first graph convolution layer of the classification block. These learned weights are obtained by the end-to-end learning process to deliver accurate prediction of classes. These weights reflect the most discriminative brain regions distinguishing between male and female classes. .... 92

**Figure 4.12** : Centeredness comparison of connectional templates generated by **A**) single-view integration methods including network atlas-guided feature selection (NAG-FS) [7], similarity network fusion (SNF) [1], and supervised multi-topology network cross-diffusion (SM-netFusion) [8]; and **B**) multi-graph fusion methods including multi-view networks normalizer (netNorm) [2], SNF-Clustering-Average (SCA) [9], multi-view clustering and fusion (MVCF-Net) [10], cluster-based multi-graph integrator networks (cMGI-Net) [20], and deep graph normalizer (DGN) [11]. Charts illustrate the mean Frobenius distance between the connectional templates learned from the training sets and networks of the samples in the testing set using a 5-fold cross-validation strategy. We reported the average distance for each cross-validation fold as well as the average across folds (“Mean” bars on the right). For multi-graph fusion methods comparison, DGN achieved the lowest mean Frobenius distance to the population multi-view networks with a high statistical significance demonstrated by a two-tailed paired t-test (all  $p < 0.0001$ ) for DGN-SCA, DGN-netNorm, DGN-MVCFNet, and DGN-cMGI-Net pairs for AD-LH, AD-RH, LMCI-LH and LMCI-RH groups. LH: left hemisphere. RH: right hemisphere. AD: Alzheimer’s disease. LMCI: Late Mild Cognitive Impairment. As for single-view fusion methods comparison, SM-netFusion significantly achieved the lowest mean Frobenius distance to the population single-view networks (all  $p < 0.0001$ ) using two-tailed paired t-test for SM-netFusion-NAGFS, and SM-netFusion-SNF pairs for AD-LH, AD-RH, LMCI-LH and LMCI-RH datasets. .... 97

**Figure 4.13** : Comparison of the average topological distributions across 5-fold cross-validation of PageRank [12], Katz centrality [13], node strength [14], random-walk centrality [15], information centrality [16], Laplacian centrality [17], eigenvector centrality [18], and betweenness centrality [19] of templates generated by **A**) SNF [1], NAG-FS [7], and SM-netFusion [8] against the ground truth distribution for a population of single-view network; and **B**) netNorm [2], SCA [9], MVCF-Net [10], cMGI-Net [20], and DGN [11] against the ground truth distribution for a population of multi-view network for AD and LMCI datasets in the left and right hemispheres. ....101

**Figure 4.14** : This chart displays the average topological distributions of PageRank [12], Katz centrality [13], node strength [14], random-walk centrality [15], information centrality [16], Laplacian centrality [17], eigenvector centrality [18], and betweenness centrality [19] measures across the nodes (ROIs) of the learned templates generated by **A**) SNF [1], NAG-FS [7], and SM-netFusion [8] against the ground truth distribution of a population of single-view networks; and **B**) netNorm [2], SCA [9], MVCF-Net [10], cMGI-Net [20], and DGN [11] against the ground truth distribution of a population of multi-view network for the AD and LMCI datasets in the left and right hemispheres. For multi-graph fusion methods comparison, DGN achieved the highest average distribution comparing to the average distribution of other multigraph fusion methods with a high statistical significance demonstrated by a two-tailed paired t-test (all  $p < 0.0001$ ) for DGN-SCA, DGN-netNorm, DGN-MVCFNet, and DGN-cMGI-Net pairs for AD (LH), AD (RH), LMCI (LH) and LMCI (RH) groups, except for the random-walk centrality measures. For single-view fusion methods comparison, SM-netFusion significantly achieved the maximum average distribution comparing to SNF and NAG-FS for all centrality measures except the betweenness centrality and node strength for AD (LH), AD (RH), LMCI (LH) and LMCI (RH) datasets. ....102

**Figure 4.15** : Average of Kullback-Liebler divergence distribution across 5-fold cross validation between the ground truth distribution and the average topological distributions of the learned connectional templates generated by **A)** single-view fusion methods (SNF [1], NAG-FS [7],and SM-netFusion [8]); and **B)** multigraph fusion methods (SCA [9], netNorm [2], MVCF-Net [10], cMGI-Net [20], and DGN [11]). The topological measures include PageRank [12], Katz centrality [13], node strength [14], random-walk centrality [15], information centrality [16], Laplacian centrality [17], eigenvector centrality [18], and betweenness centrality [19]. Charts illustrate that for multi-graph fusion methods comparison, DGN achieved the minimum mean KL-divergence distribution and the narrowest dispersion range with a high statistical significance demonstrated by a two-tailed paired t-test (all  $p < 0.0001$ ) for DGN-SCA, DGN-netNorm, DGN-MVCFNet, and DGN-cMGI-Net pairs for AD-LH, AD-RH, LMCI-LH and LMCI-RH groups. For single-view fusion methods comparison, SM-netFusion significantly achieved the lowest mean KL-divergence distribution to the population single-view networks (all  $p < 0.0001$ ) using two-tailed paired t-test for SM-netFusion-NAGFS, and SM-netFusion-SNF pairs for AD-LH, AD-RH, LMCI-LH and LMCI-RH datasets. [Box plot legend: median (midline), box (25th and 75th percentiles), and whiskers (extrema)].....105

**Figure 4.16** : Dissimilarity between the possible pairs combination of **A)** single-view and **B)** multigraph fusion methods using KL-divergence for the AD and LMCI in the left and the right hemispheres.....106

**Figure 4.17** : Region-wise local efficiency distribution of connectional brain templates generated by **A)** SNF [1], NAG-FS [7], and SM-netFusion [8] against the ground truth distribution for single-view fusion methods comparison; and **B)** netNorm [2], SCA [9], MVCF-Net [10], cMGI-Net [20], and DGN [11] against the ground truth for multi-graph integration methods using 5-fold cross-validation for the AD and LMCI populations in the left and right hemispheres. For multi-graph fusion methods comparison, DGN achieved the most similar distribution to the ground truth while SM-netFusion displayed the closest distribution. ....107

**Figure 4.18** : Charts display the average local efficiency distribution across regions (ROIs), modularity, global efficiency, and participation coefficient of connectional brain templates estimated by **A**) single-view fusion methods (SNF [1], NAG-FS [7], and SM-netFusion [8]) and **B**) multigraph fusion methods (netNorm [2], SCA [9], MVCF-Net [10], cMGI-Net [20], and DGN [11]) against the ground truth for AD-LH, LMCI-LH, AD-RH, and LMCI-RH groups using 5-fold cross validation. Remarkably, DGN achieved the highest scores including average local efficiency distribution over regions, modularity, participation coefficient, and global efficiency comparing to other multigraph fusion methods with a high statistical significance demonstrated by a two-tailed paired t-test (all  $p < 0.0001$ ) for DGN-SCA, DGN-netNorm, DGN-MVCFNet, and DGN-cMGI-Net pairs for AD-LH, AD-RH, LMCI-LH and LMCI-RH groups. While for the single-view integration methods comparison, SM-netFusion significantly outperformed SNF and NAG-FS for AD and LMCI datasets in both hemispheres (all  $p < 0.0001$ ).....108

**Figure 4.19** : Pairwise distance comparison of the learned connectional templates generated by **A**) single-view fusion methods (SNF [1], NAG-FS [7], and SM-netFusion [8]); and **B**) multigraph fusion methods (netNorm [2], SCA [9], MVCF-Net [10], cMGI-Net [20], and DGN [11]) using Hamming distance and Jaccard distance measures for AD and LMCI populations in the left and right hemispheres.....108

**Figure A.1** : Centeredness comparison of connectional templates generated by **A**) single-view integration methods including network atlas-guided feature selection (NAG-FS) [7], similarity network fusion (SNF) [1], and supervised multi-topology network cross-diffusion (SM-netFusion) [8]; and **B**) multi-graph fusion methods including multi-view networks normalizer (netNorm) [2], cluster-based network fusion (SCA) [9], multi-view clustering and fusion (MVCF-Net) [10], cluster-based multi-graph integrator networks (cMGI-Net) [20], and deep graph normalizer (DGN) [11]. Charts illustrate the mean Frobenius distance between the connectional templates learned from the training sets and networks of the samples in the testing set using a 5-fold cross-validation strategy. We reported the average distance for each cross-validation fold as well as the average across folds (“Mean” bars on the right). For multi-graph fusion methods comparison, DGN achieved the lowest mean Frobenius distance to the population multi-view networks with a high statistical significance demonstrated by a two-tailed paired t-test (all  $p < 0.0001$ ) for DGN-SCA, DGN-netNorm, DGN-MVCFNet, and DGN-cMGI-Net pairs for M-LH, M-RH, F-LH and F-RH groups. LH: left hemisphere. RH: right hemisphere. M: Male population. F: Female population. As for single-view fusion methods comparison, SM-netFusion significantly achieved the lowest mean Frobenius distance to the population single-view networks (all  $p < 0.0001$ ) using two-tailed paired t-test for SM-netFusion-NAGFS, and SM-netFusion-SNF pairs for M-LH, M-RH, F-LH and F-RH datasets.....129

**Figure A.2** : Comparison of the average topological distributions across 5-fold cross-validation of PageRank [12], Katz centrality [13], node strength [14], random-walk centrality [15], information centrality [16], Laplacian centrality [17], eigenvector centrality [18], and betweenness centrality [19] of templates generated by **A**) SNF [1], NAG-FS [7], and SM-netFusion [8] against the ground truth distribution for a population of single-view network; and **B**) netNorm [2], SCA [9], MVCF-Net [10], cMGI-Net [20], and DGN [11] against the ground truth distribution for a population of multi-view network for M and F datasets in the left and right hemispheres.....130

**Figure A.3** : This chart displays the average topological distributions of PageRank [12], Katz centrality [13], node strength [14], random-walk centrality [15], information centrality [16], Laplacian centrality [17], eigenvector centrality [18], and betweenness centrality [19] measures across the nodes (ROIs) of the learned templates generated by **A)** SNF [1], NAG-FS [7], and SM-netFusion [8] against the ground truth distribution of a population of single-view networks; and **B)** netNorm [2], SCA [9], MVCF-Net [10], cMGI-Net [20], and DGN [11] against the ground truth distribution of a population of multi-view network for the M and F datasets in the left and right hemispheres. For multi-graph fusion methods comparison, DGN achieved the highest average distribution comparing to the average distribution of other multigraph fusion methods with a high statistical significance demonstrated by a two-tailed paired t-test (all  $p < 0.0001$ ) for DGN-SCA, DGN-netNorm, DGN-MVCFNet, and DGN-cMGI-Net pairs for M (LH), M (RH), F (LH) and F (RH) groups, except for the random-walk centrality measures. For single-view fusion methods comparison, SM-netFusion significantly achieved the maximum average distribution comparing to SNF and NAG-FS for all centrality measures except the betweenness centrality and node strength for M (LH), M (RH), F (LH) and F (RH) datasets.....131

**Figure A.4** : Average of Kullback-Liebler divergence distribution across 5-fold cross validation between the ground truth distribution and the average topological distributions of the learned connectional templates generated by **A)** single-view fusion methods (SNF [1], NAG-FS [7], and SM-netFusion [8]); and **B)** multigraph fusion methods (SCA [9], netNorm [2], MVCF-Net [10], cMGI-Net [20], and DGN [11]). The topological measures include PageRank [12], Katz centrality [13], node strength [14], random-walk centrality [15], information centrality [16], Laplacian centrality [17], eigenvector centrality [18], and betweenness centrality [19]. Charts illustrate that for multi-graph fusion methods comparison, DGN achieved the minimum mean KL-divergence distribution and the narrowest dispersion range with a high statistical significance demonstrated by a two-tailed paired t-test (all  $p < 0.0001$ ) for DGN-SCA, DGN-netNorm, DGN-MVCFNet, and DGN-cMGI-Net pairs for M-LH, M-RH, F-LH and F-RH groups. For single-view fusion methods comparison, SM-netFusion significantly achieved the lowest mean KL-divergence distribution to the population single-view networks (all  $p < 0.0001$ ) using two-tailed paired t-test for SM-netFusion-NAGFS, and SM-netFusion-SNF pairs for M-LH, M-RH, F-LH and F-RH datasets. [Box plot legend: median (midline), box (25th and 75th percentiles), and whiskers (extrema).]132

**Figure A.5** : Dissimilarity between the possible pairs combination of **A)** single-view and **B)** multigraph fusion methods using KL-divergence for the M and F in the left and the right hemispheres.133

**Figure A.6** : Pairwise distance comparison of the learned connectional templates generated by **A**) single-view fusion methods (SNF [1], NAG-FS [7], and SM-netFusion [8]); and **B**) multigraph fusion methods (netNorm [2], SCA [9], MVCF-Net [10], cMGI-Net [20], and DGN [11]) using Hamming distance and Jaccard distance measures for M and F populations in the left and right hemispheres.....133

**Figure A.7** : Region-wise local efficiency distribution of connectional brain templates generated by **A**) SNF [1], NAG-FS [7], and SM-netFusion [8] against the ground truth distribution for single-view fusion methods comparison; and **B**) netNorm [2], SCA [9], MVCF-Net [10], cMGI-Net [20], and DGN [11] against the ground truth for multi-graph integration methods using 5-fold cross-validation for the M and F populations in the left and right hemispheres. For multi-graph fusion methods comparison, DGN achieved the most similar distribution to the ground truth while SM-netFusion displayed the closest distribution. ....134

**Figure A.8** : Charts display the average local efficiency distribution across regions (ROIs), modularity, global efficiency, and participation coefficient of connectional brain templates estimated by **A**) single-view fusion methods (SNF [1], NAG-FS [7], and SM-netFusion [8]) and **B**) multigraph fusion methods (netNorm [2], SCA [9], MVCF-Net [10], cMGI-Net [20], and DGN [11]) against the ground truth for M-LH, F-LH, M-RH, and F-RH groups using 5-fold cross validation. Remarkably, DGN achieved the highest scores including average local efficiency distribution over regions, modularity, participation coefficient, and global efficiency comparing to other multigraph fusion methods with a high statistical significance demonstrated by a two-tailed paired t-test (all  $p < 0.0001$ ) for DGN-SCA, DGN-netNorm, DGN-MVCFNet, and DGN-cMGI-Net pairs for M-LH, M-RH, F-LH and F-RH groups. While for the single-view integration methods comparison, SM-netFusion significantly outperformed SNF and NAG-FS for M and F datasets in both hemispheres (all  $p < 0.0001$ ). ....134

**MULTI-MODAL NEUROIMAGING DATA PREDICTION:  
ESTIMATION OF CONNECTIONAL BRAIN TEMPLATE AND MULTIGRAPH  
CLASSIFICATION WITH APPLICATION TO GENDER FINGERPRINTING**

**SUMMARY**

The work developed in this Ph.D. thesis concerns the design of machine learning and geometric deep learning models that estimate a holistic representation of a population of multigraph brain connectivity and use the learnable integration networks for classification tasks with application to gender fingerprinting. Male and female brains are demonstrated to be highly distinguishable. Understanding sex differences in the brain has implications for elucidating variability in the incidence and progression of the disease, psychopathology, and differences in psychological traits and behavior. Decoding the brain construct using diverse neuroimaging techniques seems to be the ultimate pursuit of neuroscientists as well as brain-imaging analysts to extract the difference in genders' brains, thus boosting the neurological disorder diagnosis and prognosis related to sex. Currently, where an increasing number of brain imaging is being collected to investigate both women and man brains at their different modalities, more advanced analytical tools are required to meet new challenges revealed by large, complex, and multi-source sets of brain networks. On one hand, the estimation of a connectional brain template (CBT) integrating a population of brain networks while capturing shared and differential connectional patterns across individuals remains unexplored in gender fingerprinting. On the other hand, multigraphs with heterogeneous views present one of the most challenging obstacles to classification tasks due to their complexity. Several works based on feature selection have been recently proposed to disentangle the problem of multigraph heterogeneity. However, such techniques have major drawbacks. First, the bulk of such works lies in the vectorization and the flattening operations, failing to preserve and exploit the rich topological properties of the multigraph. Second, they learn the classification process in a dichotomized manner where the cascaded learning steps are pieced in together independently. Hence, such architectures are inherently agnostic to the cumulative estimation error from step to step. To overcome these drawbacks, in this thesis, we propose a medical computer-aided diagnosis tool enabling us to address the key challenges related to brain networks collected from multiple sources/modalities. First, we proposed how to estimate representative and centered brain network atlases, which can be leveraged to identify discriminative brain connectivities between male and female populations across heterogeneous datasets. Perhaps one of the greatest scientific challenges is to create a representative map of a brain network population acting as a connectional fingerprint. A very recent concept -connectional brain template (CBT), presents a powerful tool for capturing the most important and

discriminative traits of a specific population while preserving its topological patterns. The idea of a CBT is to integrate a population of heterogeneous brain connectivity networks into a unified representation. Specifically, we present the first study to estimate gender-specific CBTs using multi-view cortical morphological networks (CMNs) estimated from conventional T1-weighted magnetic resonance imaging (MRI). Specifically, each CMN view is derived from a specific cortical attribute (e.g. thickness), encoded in a network quantifying the dissimilarity in morphology between pairs of cortical brain regions. To this aim, we propose Multi-View Clustering and Fusion Network (MVCF-Net), a novel multi-view network fusion method, which can jointly identify consistent and differential clusters of multi-view datasets in order to capture simultaneously similar and distinct connectional traits of samples. Our MVCF-Net method estimates a representative and well-centered CBTs for male and female populations, independently, to eventually identify their fingerprinting regions of interest (ROIs) in four main steps. First, we perform multi-view network clustering model based on manifold optimization which groups CMNs into shared and differential clusters while preserving their alignment across views. Second, for each view, we linearly fuse CMNs belonging to each cluster, producing local CBTs. Third, for each cluster, we non-linearly integrate the local CBTs across views, producing a cluster-specific CBT. Finally, by linearly fusing the cluster-specific centers we estimate a final CBT of the input population. MVCF-Net produced the most centered and representative CBTs for male and female populations and identified the most discriminative ROIs marking gender differences. The most two gender-discriminative ROIs involved the lateral occipital cortex and pars opercularis in the left hemisphere and the middle temporal gyrus and lingual gyrus in the right hemisphere. Second, to address the major issues in classifying complex data, we put forward an integration learning which fuses multigraphs brain connectomes with the aim to boost classification performance using the integrated networks. Specifically, we introduce Multigraph Integration and Classifier Network (MICNet), the first end-to-end graph neural network-based model for multigraph classification. First, we learn a single-view graph representation of a heterogeneous multigraph using a GNN based integration model. The integration process in our model helps tease apart the heterogeneity across the different views of the multigraph by generating a subject-specific graph template while preserving its geometrical and topological properties. Second, we classify each integrated template using a geometric deep learning block which enables us to grasp the salient graph features of a specific population. We train, in end-to-end fashion, these two blocks using a single objective function to optimize the classification performance. We evaluate our MICNet in gender classification using brain multigraphs derived from different cortical measures. We demonstrate that our MICNet significantly outperformed its variants thereby showing its great potential in multigraph classification. Finally, we review current graph integration methods that estimate well-centered and representative brain connectional templates (CBTs) for populations of single-view and multigraph brain networks. Then, we conducted a comparison study on these generated CBTs by single-view and multigraph fusion methods to evaluate their performances, separately, based on the following criteria: centeredness, discriminability (biomarker-reproducibility), and topological soundness (node-level similarity, global-level similarity, and distance-based similarity). We demonstrate that deep graph normalizer (DGN) method significantly outperforms other multi-graph and all single-view integration methods for estimating CBTs using

a variety of healthy and disordered datasets in terms of centeredness, discriminability (i.e., graph-derived biomarkers reproducibility that disentangle the typical from the atypical connectivity variability), and preserving the topological traits at both local and global graph-levels.





**ÇOKLU MODAL NÖROGÖRÜNTÜLEME VERİ TAHMİNİ:  
BAĞLANTILI BEYİN ŞABLONUNUN TAHMİNİ VE CİNSİYET  
PARMAK İZİ UYGULAMASI İLE ÇOKLU GRAFİK SINIFLANDIRMA**

**ÖZET**

Bu doktora tezinde geliştirilen çalışmada, çoklu grafik beyin bağlantısı popülasyonunun bütünsel bir temsilini tahmin eden ve cinsiyet parmak izine uygulama ile sınıflandırma görevleri için öğrenilebilir entegrasyon ağlarını kullanan makine öğrenimi ve geometrik derin öğrenme modellerinin tasarımı ile ilgilidir. Erkek ve kadın beyinlerinin son derece ayırt edilebilir olduğu gösterilmiştir. Beyindeki cinsiyet farklılıklarını anlamak, hastalığın görülme sıklığı ve ilerlemesindeki değişkenliği, psikopatolojiyi ve psikolojik özellikler ve davranışlardaki farklılıkları aydınlatmak için çıkarımlara sahiptir. Çeşitli nörogörüntüleme tekniklerini kullanarak beyin yapısını deşifre etmek, sinirbilimcilerin yanı sıra beyin görüntüleme analistlerinin cinsiyetlerin beyinlerindeki farkı ortaya çıkarmak için nihai arayışı gibi görünüyor, böylece nörolojik bozukluk teşhisini ve cinsiyetle ilgili prognozu güçlendiriyor. Şu anda, hem kadın hem de erkek beyinlerini farklı modalitelerinde araştırmak için artan sayıda beyin görüntülemenin toplandığı yerde, büyük, karmaşık ve çok kaynaklı beyin ağları setlerinin ortaya çıkardığı yeni zorlukların üstesinden gelmek için daha gelişmiş analitik araçlara ihtiyaç duyulmaktadır. Bir yandan, bireyler arasında paylaşılan ve farklı bağlantı kalıplarını yakalarken bir beyin ağları popülasyonunu bütünleştiren bir bağlantısal beyin şablonunun (CBT) tahmini, cinsiyet parmak izinde keşfedilmemiş kalır. Öte yandan, heterojen görünümlere sahip çoklu grafikler, karmaşıklıkları nedeniyle sınıflandırma görevlerinin önündeki en zorlu engellerden birini sunar. Son zamanlarda, çoklu grafik heterojenliği sorununu çözmek için öznitelik seçimine dayalı birkaç çalışma önerilmiştir. Bununla birlikte, bu tür tekniklerin önemli dezavantajları vardır. İlk olarak, bu tür çalışmaların büyük kısmı vektörleştirme ve düzleştirme işlemlerinde yatmakta olup, çoklu grafiğin zengin topolojik özelliklerini koruyamamakta ve kullanamamaktadır. İkinci olarak, kademeli öğrenme adımlarının bağımsız olarak bir araya getirildiği, sınıflandırma sürecini ikiye bölünmüş bir şekilde öğrenirler. Bu nedenle, bu tür mimariler, adım adım kümülatif tahmin hatasına doğal olarak agnostiktir. Bu dezavantajların üstesinden gelmek için, bu tezde, birden fazla kaynaktan/modaliteden toplanan beyin ağlarıyla ilgili temel zorlukları ele almamızı sağlayan tıbbi bilgisayar destekli bir teşhis aracı öneriyoruz. İlk olarak, heterojen veri kümelerinde erkek ve kadın popülasyonları arasındaki ayrımcı beyin bağlantılarını belirlemek için kullanılacak temsili ve merkezlenmiş beyin ağı atlaslarının nasıl tahmin edileceğini önerdik. Belki de en büyük bilimsel zorluklardan biri, bağlantı parmak izi görevi gören bir beyin ağı popülasyonunun temsili bir haritasını oluşturmaktır. Çok yeni bir kavram olan bağlantısal beyin şablonu (CBT), belirli bir popülasyonun topolojik modellerini korurken en önemli ve ayırt edici özelliklerini

yakalamak için güçlü bir araç sunar. Bir BDT fikri, heterojen beyin bağlantı ağlarından oluşan bir popülasyonu birleşik bir temsile entegre etmektir. Spesifik olarak, geleneksel T1 ağırlıklı manyetik rezonans görüntüleme (MRI) tahmin edilen çok görüntülü kortikal morfolojik ağları (CMN'ler) kullanarak cinsiyete özgü CBT'leri tahmin eden ilk çalışmayı sunuyoruz. Spesifik olarak, her CMN görünümü, kortikal beyin bölgeleri çiftleri arasındaki morfolojideki farklılığı ölçen bir ağda kodlanmış belirli bir kortikal öznelikten (örn. kalınlık) türetilir. Bu amaçla, aynı anda benzer ve farklı bağlantı verilerini yakalamak için çoklu görünüm veri kümelerinin tutarlı ve farklı kümelerini ortaklaşa tanımlayabilen yeni bir çoklu görünüm ağ füzyon yöntemi olan Çoklu Görünüm Kümeleme ve Füzyon Ağı (MVCF-Net) öneriyoruz. örneklerin özellikleri. MVCF-Net yöntemimiz, erkek ve kadın popülasyonları için temsili ve iyi merkezli CBT'leri bağımsız olarak tahmin ederek, parmak izi alan ilgi bölgelerini (ROI'ler) dört ana adımda tanımlar. İlk olarak, CMN'leri paylaşılan ve diferansiyel kümeler halinde gruplandırırken görünüm arasındaki hizalarını koruyan manifold optimizasyonuna dayalı bir çoklu görünüm ağ kümeleme modeli gerçekleştiriyoruz. İkinci olarak, her görünüm için, yerel CBT'ler üreterek, her küme için CMN'leri doğrusal olarak birleştiririz. Üçüncüsü, her küme için, küme için, küme için, küme için yerel CBT'leri görünüm arasında doğrusal olmayan bir şekilde bütünleştiririz. Son olarak, küme için, küme için, küme için, küme için yerel CBT'leri doğrusal olarak birleştirerek, girdi popülasyonunun nihai bir CBT'sini tahmin ederiz. MVCF-Net, erkek ve kadın popülasyonları için en merkezli ve temsili CBT'leri üretti ve cinsiyet farklılıklarına işaret eden en ayırmacı ROI'leri belirledi. Cinsiyete dayalı en fazla iki ROI, sol hemisferde lateral oksipital korteks ve pars opercularis ve sağ hemisferde orta temporal girus ve lingual girus ile ilgiliydi. İkinci olarak, karmaşık verilerin sınıflandırılmasındaki ana sorunları ele almak için, entegre ağları kullanarak sınıflandırma performansını artırmak amacıyla çoklu grafik beyin bağlantılarını birleştiren bir entegrasyon öğrenimi ortaya koyduk. Spesifik olarak, çoklu grafik sınıflandırması için ilk uçtan uca grafik sinir ağı tabanlı model olan Multigraph Integration and Classifier Network'ü (MICNet) tanıtıyoruz. İlk olarak, GNN tabanlı bir entegrasyon modeli kullanarak heterojen bir çoklu grafiğin tek görünüşlü bir grafik temsiliğini öğreniyoruz. Modelimizdeki entegrasyon süreci, geometrik ve topolojik özelliklerini korurken konuya özel bir grafik şablonu oluşturarak çoklu grafiğin farklı görünümü arasındaki heterojenliği ayırmaya yardımcı olur. İkinci olarak, belirli bir popülasyonun göze çarpan grafik özelliklerini kavramamızı sağlayan bir geometrik derin öğrenme bloğu kullanarak her bir entegre şablonu sınıflandırıyoruz. Sınıflandırma performansını optimize etmek için tek bir amaç fonksiyonu kullanarak bu iki bloğu uçtan uca bir şekilde eğitiyoruz. MICNet'imizi farklı kortikal ölçümlerden elde edilen beyin multigraflarını kullanarak cinsiyet sınıflandırmasında değerlendiriyoruz. MICNet'imizin varyantlarından önemli ölçüde daha iyi performans gösterdiğini ve böylece çoklu grafik sınıflandırmasındaki büyük potansiyelini gösterdiğini gösterdik. Son olarak, tek görüntülü ve çok grafikli beyin ağlarının popülasyonları için iyi merkezli ve temsili beyin bağlantı şablonlarını (CBT'ler) tahmin eden mevcut grafik entegrasyon yöntemlerini gözden geçiriyoruz. Ardından, performanslarını aşağıdaki kriterlere göre ayrı ayrı değerlendirmek için tekli görünüm ve çoklu grafik füzyon yöntemleriyle oluşturulan bu CBT'ler üzerinde bir karşılaştırma çalışması gerçekleştirdik: merkezlilik, ayırt edilebilirlik (biyobelirteç-tekrarlanabilirlik) ve topolojik sağlamlık (düğüm düzeyinde benzerlik, küresel kaldırma benzerliği ve mesafeye dayalı benzerlik). Derin grafik normalleştirici (DGN) yönteminin, merkezlilik, ayırt edilebilirlik (yani, çözülen grafikten türetilen

biyobelirteçler yeniden üretilebilirliği) açısından çeşitli sağlıklı ve düzensiz veri kümelerini kullanarak CBT'leri tahmin etmek için diğer çoklu grafik ve tüm tek görünüm entegrasyon yöntemlerinden önemli ölçüde daha iyi performans gösterdiğini ortaya koymuş (tipik olanı atipik bağlantı değişkenliğinden ayıran grafikten türetilen biyobelirteçler tekrarlanabilirliği) ve hem yerel hem de küresel grafik düzeylerinde topolojik özellikleri korunması sağlanmıştır.





## 1. INTRODUCTION

The aim of this chapter is to present valuable role of morphological brain connectomes to investigate gender difference and its impact on the brain diseases using integration concept. *Section* 1.1 describes brain connectivity networks extracted from different sources of Magnetic resonance imaging to investigate gender difference and its impact on the human health. *Section* 1.2 describes the connectional fingerprint concept of heterogeneous multimodal data. Then, detailed descriptions of connectomes, multigraph integration, and multigraph classification are provided in *section* 1.3. *Section* 1.4 describes in detail the road map and the contributions of this thesis.

### 1.1 Gender Difference and Brain Connectivity

The brain construct encodes subtle differences in the anatomy and the cognitive function, as well as the human behaviors between men and women. For instance, gender has demonstrated a substantial influence on many areas of brain and behavior, including emotion, memory, perception, language, and other cognitive domains cahill2006sex. For example, men perform better in mental rotation and visuospatial perception processing, whereas women have advantages in verbal memory and fluency and in the speed of articulation hamilton2008cognition. These differences emerge during foetus development period where research has shown that male fetuses appear to involute fewer overproduced cortical neurons than females [21]. Morphologically, men have a larger brain than do women. Prior studies have suggested that focal differences of Gray Matter (e.g., cortical thickness) between males and females might account for their behavioral differences [22, 23].

Moreover, gender is an important determinant of human health. In fact, plenty of studies have shown that several brain disorders can be related to gender. This difference in disorder between men and women could explain in part that the male brain undergoes greater functional impairments from early brain damage whereas the

female brain exhibits a higher incidence and prevalence of dementia [24]. Hence, it is important to first pin down gender differences in the healthy human brain. This can potentially help devise a personalized treatment for different neurological disorders, tailored for male and female populations, respectively.

On the other hand, emerging neuroimaging studies have reported gender effects on the structural organization of White Matter, indicating an important role for brain connectivity between brain regions in sexual dimorphism [25, 26]. Specifically, structural magnetic resonance brain imaging (sMRI) and diffusion magnetic resonance brain imaging (dMRI) data have revealed substantial gender differences in white matter-based anatomical connectivity. Structural MRI data further demonstrated gender differences in the connectivity revealed by morphometric correlation among brain areas. Functional connectivity derived from functional neuroimaging such as resting state functional magnetic resonance brain imaging (fMRI) and Positron Emission Tomography (PET) data is also modulated by gender. Moreover, male and female human brains display differences in the network topology that represents the organizational patterns of brain connectivity across the entire brain. Hence, we resort to modeling the brain as a network, where the interaction between regions (connectivities) becomes a biological feature of interest to capture the functional, morphological and topological differences between genders.

Despite this growing body of research on such networks and how they encode for gender differences, however, there is still a large gap in the literature where cortical morphological networks (CMN) remain unexplored with respect to gender. In fact, CMN where each network models the relationship in morphology between different cortical brain regions quantified using a specific measurement (e.g., cortical thickness), have not been investigated with respect to gender differences in the human brain. On the other hand, based on the tension theory of cerebral cortex morphogenesis suggesting that cortical morphology reflects the underlying changes in the structural and functional connectome [27], recent studies have started exploring morphological connections of the cortex and how they are altered by neurological disorders including dementia [28, 29] and autism [9, 30], and how they are linked

to cognition and genomics [31]. The majority of these seminal works applied machine learning on brain morphological network datasets and demonstrated their potential in unraveling the cortical brain construct from a connective viewpoint while leveraging minimal financial resources for brain scanning without the need of costly and time-consuming fMRI and DWI. A landmark work investigated gender differences in cortical morphological complexity [23] in independent as opposed to interactive brain regions; however, no previous studies investigated how gender influences morphological connections.

## **1.2 Connective Fingerprint of Heterogeneous Multimodal Data**

Exploring data from the aforementioned neuroimaging sources in the previous paragraph (e.g., functional MRI, structural MRI, diffusion MRI, PET imaging) provides multiple modalities spanning the healthy and disordered brain spectrum. Specifically, multimodal brain imaging has shown tremendous potential for neurological disorder diagnosis, where each imaging modality offers specific information for learning more holistic and informative data representations. For instance, connections in brain networks derived from resting fMRI encode correlations in functional activity among brain regions, whereas DTI networks provide information concerning structural connections (i.e., white matter fiber paths) between these nodes [32–34]. Joining both networks results in two different modalities of brain connectivity, leading to a variability of the data. Therefore, it is unsurprising that understanding brain network connectivity across different modalities has long been a central goal of neuroscience and has recently catalyzed an unprecedented era of large-scale initiatives and collaborative projects to map brain networks more comprehensively and in greater detail than ever before.

Understanding how the brain's structural, morphological, and functional levels interlink offer more comprehensive picture of the brain facets construction [35]. However, analyzing these multi-modal connectomic data (brain networks) together, remains challenging due to the large inter-modality variations in different views of connectivity networks and the heterogeneity of connective brain networks across the population samples [36, 37]. Nonetheless, mapping brain networks of a whole

population into a single representation is useful to capture the most shared and representative brain signature across a population [38].

However, an individual signature of a particular subject differs from one to another, making the identification of biomarkers associated with a specific population harder. Mostly, these biomarkers are important in disentangling the typical from the atypical variations across the population samples and extracting their different patterns. For example, numerous studies have started to emphasize the importance of looking for commonalities and differences in neurobiological and psychiatric changes across brain disorders [29, 39, 40], which may improve our ability to understand the differences between comorbid disorders such as autism and dementia. Consequently, extracting an integral connectional fingerprint of heterogeneous brain networks of a given population while preserving their common and distinct patterns remains a critical pursuit towards assisting researchers to develop novel integration models.

### **1.3 Graph Theory, Connectomes, and Multigraph**

Since brain network has undeniably a complex structure, understanding the relationship between these connectivities across different modalities is very challenging task before moving to the brain networks integration. This brings us to the concept of graphs and the graph theory approach where they have been crucial in recent efforts to represent and comprehend the function and structure of complex systems. First, mapping the brain network as graph where nodes represent the brain regions and edges between nodes represent the anatomical connections between these neural elements is an essential step to analyse the brain using those graph theoretical methods [41, 42]. Then, applying graph theory methods provides a really powerful way to quantitatively describe the topological organisation of brain connectivity (e.g, patterns). They give a way of transforming the confusing messy into a neat organization (Figure 1.1) where we can directly make inferences for the topological organization of this network.

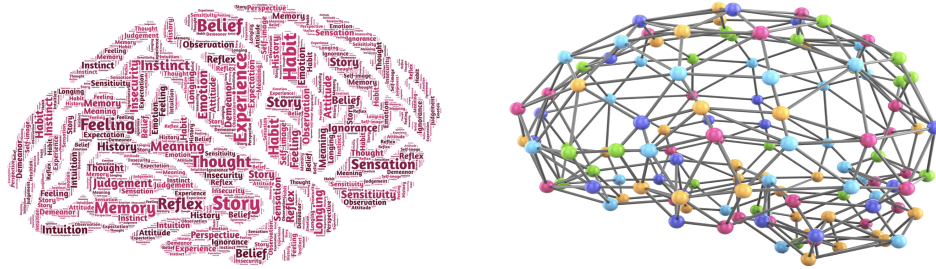


**Figure 1.1 :** Brain graph analysis. From confusing messy to neat organisation.

In the same context, the concept of "connectome" was introduced by [38] where they assign to each brain graph a matrix representing all possible pairwise connections between the brain regions. Specifically, the graph nodes denoting different brain regions are represented by the rows or columns of the matrix, and the connection (edges) between two nodes is represented by the respective matrix element (Figure 1.2). This equivalence between graph representations and matrix signifies that we can use both of them in the analysis of brain network connectivity.

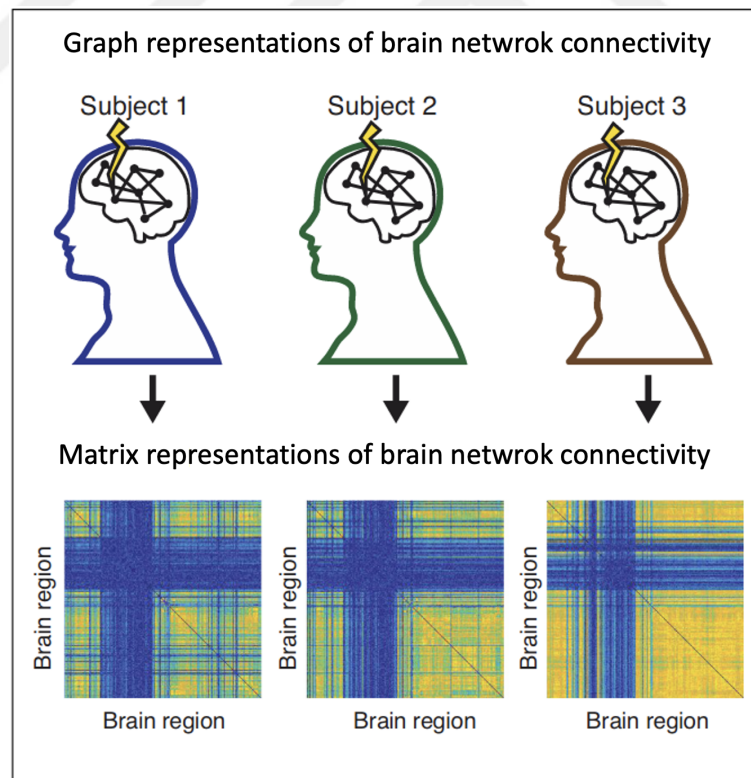


**Figure 1.2 :** Brain graph as a matrix (connectome).

Since brain data was collected from multiple neuroimaging modality (e.g., functional MRI or diffusion MRI), the generated multimodal brain connectivity networks(e.g.,

functional and morphological connectivities) [29,30,43] can be modeled by multigraph representation. Specifically, the interaction denoting the multimodal brain connectivity between two anatomical regions of interest (ROIs), namely the multigraph nodes, is encoded in a set of edges of multiple types. Each edge type defines that particular modality for modeling the relationship between brain ROIs. Hence, using the concept of connectomes, a brain multigraph can be mathematically encoded in a tensor, which can also be viewed as a set of stacked matrices, where each matrix represents a different type of edges (connectivities) of the graph.

### **1.3.1 Multigraph integration**

The concept of integration comes in to normalize a set of multigraphs, while considering all edge weights, thereby fusing complementary information into a representative template of a given population of multigraphs. A good fused representation should carry the different traits and relevant patterns characterizing the graph population to guarantee its representativeness. Among various integration techniques, some are based on graph comparison techniques such as graph edit distance (GED) [44]. However, these methods not only fail to simultaneously satisfy graph scalability, node and permutation-invariance criteria but also are originally designed to work on single-view graphs.

Another type of integration methods rely on multiple kernel-based comparison methods which can optimally take into account the multiscale structure of graphs. Each kernel can capture a particular graph scale which makes these algorithms more scale adaptive [45]. However, such graph fusion approaches raise a computational overhead cubic in deriving Laplacian Matrix Eigenvalues and when the size of the graph exponentially grows.

In the same context, more recent machine learning methods coped with the graph integration task. For instance, SNF-Clustering-Average (SCA) method based on similarity network fusion (SNF) [1] was introduced in [9]. It performs linear and non-linear fusion operations on different multigraphs. Another technique is netNorm which builds a representative template based on feature selection prior

to a non-linear fusion [2]. More recently, a supervised multi-topology network cross-diffusion (SM-netFusion) was proposed by [46] based on graph topological measures. SM-netFusion uses a weighted mixture of multi-topological measures to enhance the non-linear fusion process for supervised graph integration. Although it takes into account the heterogeneity of the data, this method is limited to single view graphs. Another drawback of these last methods is that they work in a dichotomized manner and not in an end-to-end fashion.

To overcome these limitations, emerging geometric deep learning techniques have been recently proposed. For instance, [11] introduced Deep Graph Normalizer (DGN), an end-to-end novel approach, which maps multiview networks into a centered and representative subject-biased template by introducing subject normalization loss. DGN applies consecutive graph convolutional neural layers to perform node embeddings by locally integrating edges from different heterogeneous views. Although this method works in an end-to-end fashion, the classification of multigraphs from different populations was not included in the learning process which mainly focused on population graph integration.

### **1.3.2 Multigraph classification**

Another category of studies has focused on single graph and multigraph classification tasks. For instance, spectrum-based methods [47] performed classification by generalizing the convolutional neural networks to graphs in the spectral domain where featured concepts of the architecture are transformed into the frequency domain via graph Fourier transform. One main important limitation of such spectral techniques is that they depend on the fixed spectrum of the graph Laplacian which does not make them suitable for multiple structure-view graphs.

Another type of graph classification has been developed based on spatial methods [48]. The core idea was to propagate local features between neighboring nodes. Some of them integrated a spatial graph convolutional layer to pool unarranged node features into a sorted graph representation. Such methods succeeded in achieving remarkable

performance at node classification tasks, however, they are not tailored to classify whole graphs.

Alternatively, [30] proposed an unsupervised clustering-based methods that learn a similarity matrix from graphs. [5] first vectorized brain multigraphs then applied an infinite feature selection trained with a supported vector machine classifier to identify the top discriminative edges between male and female brains. [29] performed a similar process but first computed correlation-based similarity matrices between different multigraph views prior to the feature selection step. However, such methods have a shared limitation which is the vectorization of multigraphs –causing the loss of the multigraph topological properties (Figure 1.3).

To address these issues, geometric deep learning (GDL), a recent graph-oriented learning approach extended from general-purpose deep learning, demonstrated its superiority over other approaches in classifying graphs and non-Euclidian structures in general [49]. A major GDL architecture, graph neural networks (GNNs) introduced by [50], have shown a remarkable performance in a variety of graph specific tasks such as graph classification [51], node classification and link prediction [52]. GNNs are not only simple to implement, but they can also capture different graph underlying patterns by message passing between nodes. Besides, they do not need to go through a preprocessing step as they can operate directly on graphs.

In this context, [52] performed multiple bootstrapped graph convolutional neural networks (GCNN) to improve the classification accuracy and make it more robust against noisy data. [50] proposed GNN-based models that propagate information and construct node representations that can be “aware” of the broader graph structure. GraphSAGE [53] first performs sum, mean or max-pooling neighborhood aggregation, then updates the nodes representation by applying a linear projection on top of the convolution layer. Graph Isomorphism Network (GIN) [54] extends GraphSAGE with arbitrary aggregation functions on multi-sets. Edge-Conditioned Convolution (ECC) [51] assigns different weights to neighboring nodes by learning parameters for each edge label. [55] proposes Deep Graph Convolutional Neural Network

(DGCNN) based on convolutional layer similar to the formulation of [56] while adding a specific sorting algorithm called SortPool. DiffPool [57] proposes an adaptive hierarchical pooling mechanism that collapses nodes on the basis of a supervised criterion using differentiable graph encoders. However, such methods only work on single-view graphs and require prior preprocessing to work on multigraphs. To address this limitation, we propose for the first time an end-to-end learning based graph classification architecture using multigraph fusion. In the first step, we learn a single-view graph representation from each multigraph to disentangle the heterogeneity problem while preserving multigraph topological features. Next, we introduce these graph templates into a geometric deep learning based classification step to optimally capture the discriminative patterns in graph structure.

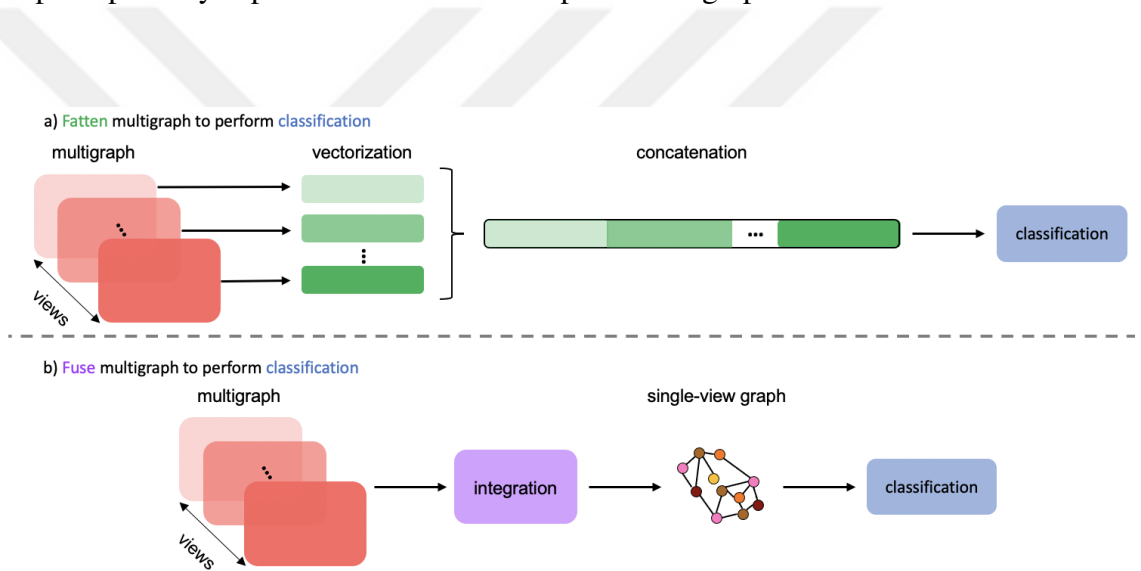


**Figure 1.3 :** *Diagram of conventional multigraph classification and integration tasks.*  
 a) Given a multigraph, typical classification methods including [5] aims to concatenate the multiple vectorized views. The stacked feature vectors are fed into an independent classification model. b) Proposed method integrates the views of the same sample into a single-view graph. Next, the fused multigraph is fed into the classification block. Both blocks work in an end-to-end manner which makes the integration block contributes to the discriminativeness and the global classification performance of the model.

## 1.4 Contributions and Road-map

The organization of this thesis is presented as follows: *Chapter 2* includes the literature and the related works of our three major contributions. *Chapter 3* details

the methodologies of our three contributions including the models architectures and their evaluations strategies. *Chapter 4* details the experimental results and the discussions of our thesis works including the data evaluation and preprocessing, parameters settings, and the comparison methods. Finally, in *chapter 5*, we discuss the implications for future research and clinical practice for our work. We also expand on the potential application of our approaches to other brain diseases and we conclude this thesis with the list of contributions.

The main contributions of this thesis and can be summarized as follows:

***Learning brain fingerprint of gender from cortical morphological datasets based on machine learning model:*** As a first contribution, we suggest to build machine learning model that learn how to integrate heterogeneous medical datasets derived from multimodal cortical measurements (e.g., maximum principal curvature, cortical thickness network, sulcal depth network) for generating a holistic representation for male and female brains that captures relevant connectional features that discriminate between them. Specifically, we propose, for the first time, a gender-specific connectional brain templates (CBTs) estimation method (MVCF-Net) using multi-view cortical morphological networks (CMNs) estimated from conventional T1-weighted magnetic resonance imaging (MRI) to disentangle male from female connectome. To this aim, given a population of brain connectomes, we propose to learn how to estimate a centered and representative morphological brain network template to reliably map the morphological connectome and its variability across training individuals, thereby capturing their shared traits (i.e., connectional fingerprint of a population). Essentially, we first learn how to cluster multi-view network based on manifold optimization which groups CMNs into shared and differential clusters while preserving their alignment across views. Next, for each view, we linearly fuse connectomes living in each cluster. Then, for each cluster, we non-linearly merge the local CBTs across views, producing a cluster-specific CBT. Last, by integrating the produced the cluster-specific centers we ultimately estimate the population network template (fingerprint). We compute the difference between male and female network CBTs to identify the most discriminative features (brain regions of interests). Our

multi-View clustering and fusion network (MVCF-Net) framework produced the most centered and representative and centered multimodal CBTs for male and female populations and identified the most discriminative ROIs marking gender differences.

***Building a geometric deep learning based integration model for multigraph***

***classification:*** As for second contribution, we suggest to build an end-to-end graph neural network based model for multigraph classification with application to genders brain connectomes. Thus, we propose the first method entitled multigraph integration and classifier network (MICNet) that couples both integration and classification in an end-to-end fashion. Specifically, having the integration block prior to classification boosts the discriminativeness of the edges that will pass through the classification block. First, we learn the integration of heterogeneous multigraph into a single-view graph representation using a GNN based integration model. Eventually, the integration process in our model will ensure a representative subject-level template of the geometrical and topological features from the original multigraphs in a discriminative approach. Thus, the integrated template will capture the most discriminative patterns of a multigraph for the purpose of the classification task. Second, we apply a subject-specific thresholding filter on the outputs of the integration block to generate binary matrices representing single-view graphs with binary edge attributes. The thresholding filter emphasizes the connections having most discriminative and representative edges used as subject fingerprints, thereby having more impact on the classification output. Last, we feed these graphs to a graph neural networks -based classification architecture which performs several graph convolutions through a sequence of embedding and pooling layers to obtain the final classification prediction. Specifically, our model learns the optimal weights of both integration and classification layers through a single objective loss function during a shared optimization process to provide the best classification performance. Our proposed geometric deep learning based classifier MICNet works in an end-to-end fashion to capture the most discriminative traits of the graph to predict gender class using brain multigraphs derived from different cortical measures.

***Comparing the performance of the existing models that estimate connectional brain template (CBT) using graph theory:*** In the third contribution, We suggest to review current graph fusion methods for CBTs generation promoted with a comparative study to evaluate their performance across extensive experiments in terms of producing the most centered templates, recapitulating unique traits of populations, and preserving the complex topology of biological networks. As a first step, we will review existent graph integration methods which can be emphasized in two categories: unimodal fusion methods and the multimodal integration methods. After summarizing them, we conduct a comparative study between fusion models of each category in separate manner by evaluating the performance of their generated CBTs. Ideally, a reliable estimated template should preserve the topological patterns and properties of a specific population during the fusion process. In more details, a CBT should satisfy the following criteria:(1) centeredness as it occupies the ‘center’ of a population by achieving the minimum distance to all population samples. (2) graph-derived biomarker reproducibility as as it allows to identify connectional biomarkers that disentangle the differences in brain connectivity between populations with different brain states (i.e., healthy and disordered or genders). (3) topological soundness to the population at different scales including node-wise similarity as it tests whether the local structure of the original data which includes the connectivity between the nodes are preserved by the CBT, distance-based similarity as it quantifies the distance between two networks by studying some characteristics, and global-based similarity as it tests whether the generated CBT preserves the global structure of the original graphs networks. In doing so, we discuss the results of the CBT evaluation measures and the strength of the best method. We highlight the limitations of the integration methods in estimating representative reference connectional templates derived from complex graph’s connectomes. We conclude with an outlook in the future of multigraphs fusion methods and discuss new avenues towards improving them to work on brain dynamic and non-isomorphic networks.

For easy and clear understanding to our work in this thesis, we provide an organized schema of three blocks where each indicates the general idea of the work done in each chapter (2,3 and 4). The roadmap schema is illustrated in Figure 1.4. To

summarize, neuroimaging studies have shown that gender is strongly related to brain disorders, and studying brain connectivity networks with respect to gender differences helps for precise diagnosis and early prediction of neurological diseases as well as deciding the treatment strategies. The existing researches have explored data from multi-modal sources including functional MRI, structural MRI and diffusion MRI to capture the difference in functional and structural connectivities. However, despite the importance of morphological connections in changing the structural and functional connectome as well as in being altered by neurological disorders, cortical morphological networks remain unexplored with respect to gender. On the other hand, unimodal and multi-modal integration models based on machine learning techniques have been developed to extract an integral connectional fingerprint of heterogeneous brain networks of a given population. That's why, the goal of this thesis is first to investigate cortical connectivity fingerprinting unveiling gender differences using integration concept. Next, by combining this latter approach with a classification model, we improve the learning process by extracting the most discriminative and representative patterns used as subject fingerprints to classifier heterogeneous brain multi graphs genders populations. For accurate evaluation of the integration model performance, we will investigate the main measures that can be extracted from the brain network with the help of graph theory. These measures define the most significant brain regions (central nodes) and the most discriminative connections unveiling gender differences. These topological measures reflect different aspects of topological centrality which means a node ability to influence (or be impacted by) other network components based on the topology of its connections [42].

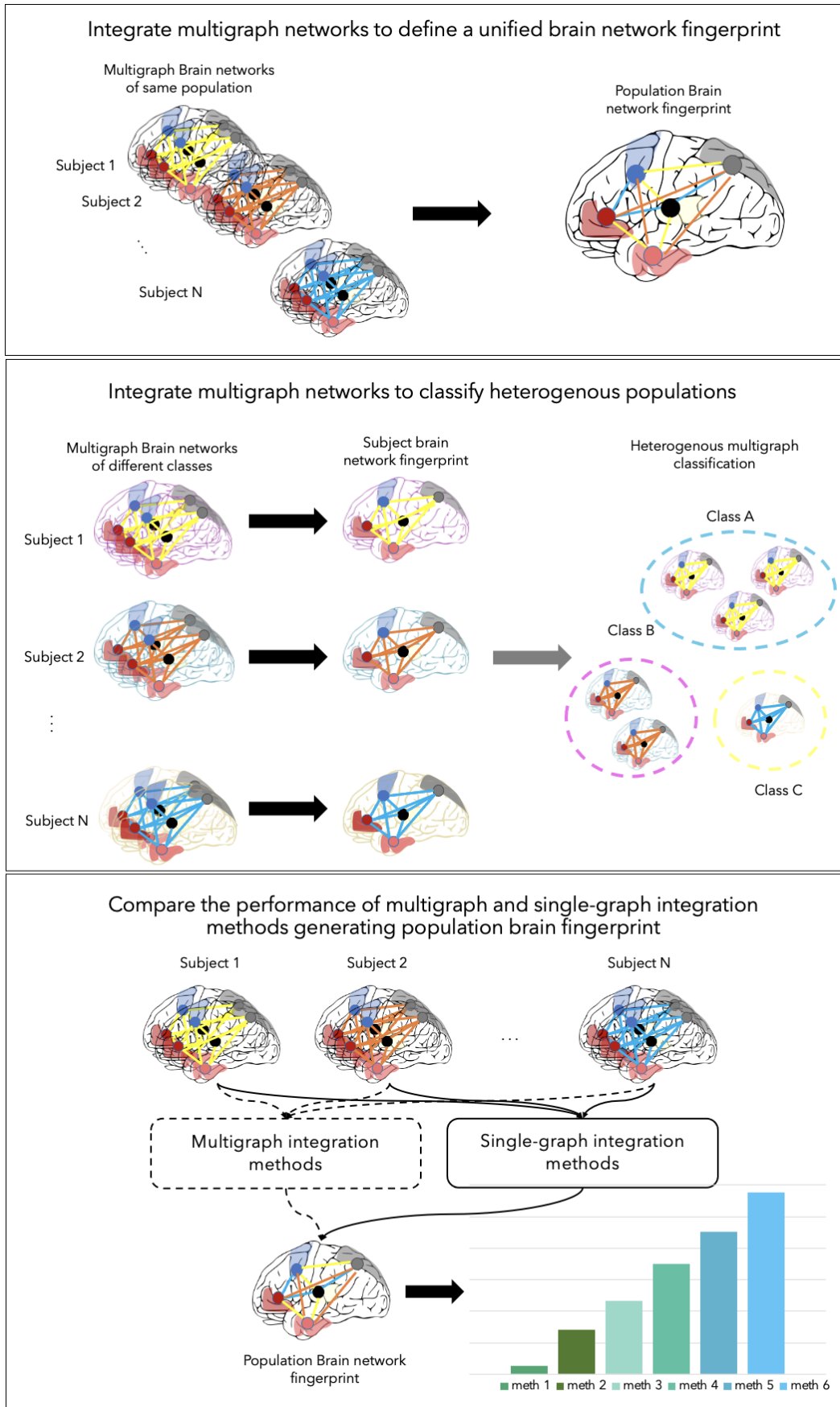


**Figure 1.4 : Roadmap of the thesis work**

## 2. LITERATURE REVIEW

The structure of the chapter is organized as follows. In *section 2.1*, the related works of our proposed Multi-View Clustering and Fusion Network (MVCF-Net) model. *Section 2.2* provided the related works of brain graph classification and integration methods. *Section 2.3* describes the evaluation strategies of our proposed integration model.

### 2.1 Related Works of Integration Models

Several human neuroimaging studies have been conducted to analyze brain connectivity between regions with respect to gender differences providing fundamental insights into the organization and integration of brain networks in male and female populations [33, 58]. In particular, brain Gender differences can be identified using functional connectivity and structural connectivity, derived from functional magnetic resonance imaging (fMRI) and diffusion weighted imaging (DWI) respectively [33, 33, 34]. By explicitly deriving structural and functional brain connectivity from functional and diffusion-weighted magnetic resonance imaging (fMRI and dMRI), network analysis presents a powerful tool for exploring structural–functional connectivity relationships [59–61] and revealing the causative linkage between connectivity changes and task performance across genders [62].

Several studies [63–66] on sex differences revealed contrasting activation patterns in cognitive abilities, behaviors and emotions between male and female brains. Such studies provide a better understanding of learning processes, language development, and progression of neurologically-based diseases such as autism spectrum disorder and depression [67, 68] across genders. What’s more, early prediction, risk, and protective factors of brain disorders can be captured, as well as personalized treatments for male and female populations can be designed. Although fMRI and dMRI neuroimaging modalities allowed the discovery of predictive brain connections fingerprinting gender differences, they may have a few limitations. On the one hand, functional MRI can

produce spurious and noisy connectomes due to the low signal-to-noise ratio induced by non-neural noise [30]. On the other hand, diffusion MRI can produce biased and largely variable structural connectomes depending on the employed fiber tractography method; a fact supported by a recent study [69] which evaluated 35 methods to generate structural connectomes and showed that how variations in diffusion MRI pre-processing steps affect network reliability and its ability to classify subjects remains opaque.

To circumvent the limitations of these neuroimaging modalities, recent studies have explored an alternative brain network representation, a cortical morphological network (CMN) constructed from structural T1-w MRI. The main idea is to build a network based on morphological connections of the cortical surface derived from a unique cortical attribute such as sulcal depth or cortical thickness. Specifically, CMNs model the relationship in morphology between different cortical regions quantified using specific cortical measurements. For instance, CMNs were investigated in neurodegenerative disorders [29, 40] as well as in neuropsychiatric disorders [30, 40]. [5] presented the first study on gender differences using CMNs of healthy subjects. This work leverages a feature selection method to find the most discriminative morphological connections between male and female cortices using different cortical attributes. Although compelling, this study might discard some of the important connective features (CFs) in revealing the gender-specific brain connective map. In fact, the utilized feature selection method selects only the important CFs and eliminates others which can lead to losing rich information when creating holistic maps of the male and female multi-view CMNs.

On the other hand, the concept of connective brain template (CBT) comes in to normalize a set of multi-view brain networks, while considering all connectivities to enable the integration of complementary information and the production of a representative ‘average’ of a given population. Hence, the estimation of a CBT provides an excellent tool for mapping human psychological behavior and cognitive functions, by providing a representative and holistic connective map of a set of multi-view brain networks. As integral and normalized representations of the

multi-view brain connectivity, CBTs estimated for each gender, can hence help spot out different connectional patterns between the male and female brains. [70] presents the first study on the estimation of a centered CBT using a population of brain networks based on a diffusive-shrinking graph technique. However, this work was limited to handling single-view networks, thereby overlooking the complementary and richness of multi-view brain networks populations, where each individual is represented by a set of brain networks (i.e., views). [9] generalized this concept to multi-view brain networks for a more holistic and integral mapping of brain connectivity by first non-linearly fusing multi-view brain networks for each individual in the population, and secondly by clustering the fused networks and integrating them within each cluster, and finally by averaging the obtained centers of all clusters. Despite its promising performance, this study has a major drawback which is clustering the samples without considering their heterogeneity across views which fails to simultaneously capture the distinct and the shared population-specific traits.

## **2.2 Related Works of Multigraph Classification Methods**

In the era of data eruption, rich and complex data can be modeled as a multigraph structure –a generic and rich graph representation where the graph nodes represent the data entities (actors) and the graph edges denote the interactions between these entities [71]. The multigraph structure enables us to model multiple relations using different types of edges between pairs of nodes [44]. Since multigraphs allow more than one relation between a pair of nodes, we can represent rich data more succinctly which in turn helps in capturing complementary information between multi-source data that cannot be discovered in the otherwise simple graphs. However, the heterogeneity aspect captured by the difference of measures across views within the same multigraph is overlooked by graph classification models intended for single-view graphs datasets [72]. Consequently, multigraph classification cannot benefit from the non-linearity provided by the richness of information carried by the different views.

Recently, there have been a great number of deep learning-based models dealing with multigraph classification [72]. However, these generalized learning architectures fail

to capture the rich topological properties of graphs. To fill this gap, geometric deep learning (GDL), a pioneering set of learning-based models, has demonstrated high performance in graph oriented tasks applied on a wide variety of applications such as molecular structures, social networks and knowledge graphs. A core element in GDL is graph neural networks (GNN) which are the extension of artificial neural networks (ANN) to the domain of graphs [50]. Another prime GDL architecture is graph convolutional networks (GCN) which are the extension of convolutional neural networks (CNN) to the graph domain [3]. GCN sequentially performs multiplication operations between original input data and a set of weights similarly to CNN. The main difference resides in the structure of the input data, since GCN deals with graphs where the number of edges change and the nodes do not have a given order.

To deeply get advantage from the hierarchical structure of the graphs, many geometric deep learning architectures have been designed such as DiffPool [57]. This method consists in hierarchically embedding nodes by assigning them to clusters. To perform embedding and assignment operations, DiffPool exploits separate GNN-based layers. Despite the promising performance of the aforementioned GDL-based techniques, they do not naturally generalize to multigraphs.

Due to its complexity, multigraph classification remains a difficult task. One of the most challenging obstacles is the heterogeneity problem resulting from different types of edges in each graph. Another major issue is the non-linear relationship across views. To alleviate data heterogeneity, some of the existing solutions proposed flattening out the multigraph structure by transforming a high-dimensional tensor to a vector. For example, [73] vectorized multimodal graph data to learn more generalized features for urban spatiotemporal forecasting. However, flattening out and concatenation techniques do not preserve the topology of the graph structure. To the best of our knowledge, no existing work investigated learning-based multigraph fusion for classification tasks. Fusion approaches can be a solution for the aforementioned problems since it blends together the different views while preserving the topological properties of the multigraph, which enables us to reduce the data high dimensionality.

Several multigraph integration methods have been conducted to generate a single-view graph. In particular, as a generic unsupervised technique, SNF [1] integrates different data types in a non-linear fashion. By constructing a sample-similarity network for each data type, SNF [1] integrates these networks into a single similarity network using a nonlinear combination method. However, SNF is limited to equal weighting of the different views within the same observation and it came with the assumption of emphasizing the nearest top-k local connections for each node. A recent selective technique, netNorm [2], normalizes and fuses a population of multi-view networks into a single-view network. To this aim, netNorm [2] constructs a high-order graph using cross-view connectional features as nodes and their Euclidean distance as dissimilarity measures to select the most significant network edges in a population. Then, the selected edges are integrated into a single network using SNF. However, one of the major limitations of netNorm resides in the total dichotomy between its different steps which blocks the feedback propagation along the process in order to globally optimize the template estimation. Therefore, errors might accumulate throughout the estimation pipeline. To overcome this limitation, a GDL-based architecture, CMGINet [20], was developed to integrate a multi-graph network preceded by clustering. First, it clusters similar samples together using multi-kernel manifold learning. Next, for each cluster, the method integrates the multigraph of each subject into a single graph, then fuses the generated graphs into a cluster-specific network. Finally, CMGINet generates a representative template by averaging the cluster-specific networks. The generated single-view graph is characterized by its representativeness and centeredness in relation to the original graphs. However, if we have two populations to classify, CMGINet [20] is agnostic to the class label of multigraphs. Hence, the investigation of how to generate discriminative templates which capture traits distinguishing between classes is important while dealing with multi-labeled datasets.

To address all these limitations, we propose the first graph neural network model that integrates and classifies multigraphs, named Multigraph Integration and Classifier Network (MICNet). Our framework consists of two main blocks. We design a multigraph integration block which is inspired from [74] to perform subject-level

multigraph integration. This block ensures the fusion of the heterogeneous views within the same multigraph. Then, we inject the subject-level integrated graphs into a graph classification block based on several node embedding and pooling layers [57]. This block performs sequential hierarchical node embeddings resulting in simpler graph representations as the network deepens to eventually output a class score. Weights of integration and classification blocks are learned through a single objective loss function during a shared optimization process. We also introduce the classification output in the global loss function which is back-propagated into the layers of both integration and classification blocks in an end-to-end manner.

The contributions of our work and the advantages of our joint multigraph integration and classification framework can be summarized as follows:

- i) We propose the first method that couples both integration and classification in an end-to-end fashion. Having an integration block prior to classification enhances the discriminativeness of the edges that will pass through the classification block.
- ii) We implement a geometric deep learning based integration in our model. This ensures a learnable representation of the geometrical and topological features from the original multigraphs.
- iii) The integration process in our model generates a representative subject-level template in a discriminative approach. The integrated template captures the most relevant patterns of a multigraph for the purpose of the classification task.
- iv) Our proposed method works in an end-to-end fashion. The model learns the optimal weights of both integration and classification layers during the same backward pass to provide the best classification performance.

### **2.3 Related Works of Single-view and Multi-view Integration Methods**

The availability of neuroimaging data using multiple data acquisition techniques is an important factor in increasing our understanding of the extraordinarily complex, yet highly organized, topology of the underlying human neural architecture; the so-called connectome [75, 76]. Using different sources of measurements, one can derive, for the same subject, multiple brain connectivity networks [77]. Having such multimodal

information, we can represent each subject by a multi-view graph where each view corresponds to an imaging modality defining a single type of brain connectivity network, each node of the graph denotes a brain region and the edge between two nodes represents the interaction between pairs of brain regions [44, 71]. A multigraph structure encapsulates the representation of multiple relations between two anatomical regions of interest (ROIs). For instance, connections in brain networks derived from resting state functional magnetic resonance brain imaging (fMRI) encode correlations in functional activity among brain regions, whereas diffusion tensor imaging (DTI) networks provide information concerning structural connections (i.e., white matter fiber paths) between these nodes [32–34]. Joining both networks results in two different views of brain connectivity, leading to a variability of the data.

Understanding how the brain's structural, morphological, and functional levels interlink offer more comprehensive picture of the brain facets construction [78]. However, analyzing these multi-modal connectomic data together, remains challenging due to the large inter-modality variations in different views of connectivity networks and the heterogeneity of connectional brain networks across the population samples [36, 37]. Nonetheless, mapping brain networks of a whole population into a single representation is useful to capture the most shared and representative brain signature across a population [38]. However, an individual signature of a particular subject differs from one to another, making the identification of biomarkers associated with a specific population harder. Mostly, these biomarkers are important in disentangling the typical from the atypical variations across the population samples and extracting their different patterns. For example, numerous studies have started to emphasize the importance of looking for commonalities and differences in neurobiological and psychiatric changes across brain disorders [28, 29, 40], which may improve our ability to understand the differences between comorbid disorders such as autism and dementia. Consequently, extracting an integral connectional fingerprint of heterogeneous brain networks of a given population while preserving their common and distinct patterns remains a critical pursuit towards assisting researchers to develop novel graph integration models.

Human neuroscience studies have made significant progress on the path towards estimating brain network templates for a population of connectomes [70]. Several integration methods were proposed to form the integrated complex representation for a population of both unimodal (single-view) [1, 7, 8] and multi-modal (multi-view) [2, 9–11, 20] brain networks. Nevertheless, single-view integration methods were limited to fuse single-view networks, thereby, overlooking the complementary and richness of multi-view brain network populations. More broadly, multi-view integration methods generalized this concept to multi-view brain networks for more holistic and integral mapping of the brain connectivity population. Both categories of fusion methods introduce the concept of connectional brain template (CBT) [70] as a normalized connectional representation of population of single-view or multi-view brain networks considering all population connectivities. Leveraging the brain template enables not only the integration of complementary information of a given population but also the generation of new connectomes for synthesizing brain graphs when minimal resources exist. Furthermore, the estimation of a population CBT provides an excellent tool for extracting integral connectional fingerprint of each population holding its most specific traits, which is an essential step for group comparison studies (e.g., the comparison of genders integral signatures).

In this forward-looking review, we introduce single-view and multi-view integration methods, focusing on how they produce for each population-type (single-view-based and multiview-based networks, respectively) a unified normalized connectional representation (CBT). After summarizing them, we conduct a comparative study between the unimodal fusion methods and the multimodal integration methods, separately, by evaluating the performance of their generated CBTs in terms of (1) well-centeredness (2) discriminativeness, and (3) topological soundness to the population at different scales including node-wise similarity, distance-based similarity, and global-based similarity. In doing so, we discuss the results of the CBT evaluation measures and the strength of the best method. We highlight the limitations of the integration methods in estimating representative reference connectional templates derived from complex graph's connectomes. We conclude with an outlook in the future of multigraphs fusion methods and discuss new avenues towards improving

them to work on brain dynamic and non-isomorphic networks.





### 3. METHODOLOGY

The structure of the chapter is organized as follows. In *section* 3.1, we present the methodology of our estimation of gender-specific connectional brain templates using joint multi-view cortical morphological network integration work. *Section* 3.2 provides the methodology of the multigraph classification using learnable integration network with application to gender fingerprinting work. *Section* 3.3 details the methodology of our comparative study of connectional brain templates in network neuroscience.

#### 3.1 Proposed Multi-View Clustering and Fusion Network (MVCF-Net)

We propose MVCF-Net, a novel multi-view network brain connectivity clustering-fusion method that estimates a representative and centered CBTs for a given population, with application to gender fingerprinting. Our method is rooted in the identification of consistent and differential clusters across brain views to generate a representative and well-centered CBT for a given population and to reduce subject inter-variability.

##### 3.1.1 MVCF-Net overview

Figure 3.1 provides an overview of the four key steps of the proposed joint multi-view network clustering and fusion framework MVCF-Net to estimate a population-based CBT from a set of multi-view CMNs: 1) feature extraction similarity networks construction, 2) multi-view clustering using optimization manifolds, 3) Individual-based non-linear fusion of connectional brain views, and 4) Linear fusion. Furthermore, we detail our evaluation strategies for assessing the representativeness and discriminability of the estimated CBTs as well as the identified of the top discriminative regions of interest differentiating both genders. To this aim, first, we leverage multi-view network clustering model based on manifold optimization

method [6], which performs clustering across data views. Thus, similar connectional traits and distinct connectional traits of samples within and across clusters in different views can be identified in an unsupervised way [6]. Second, for each view, we linearly average the CMNs of the subjects within each cluster, so that each cluster is represented by a local CBT. Third, for each aligned cluster, we non-linearly integrate its local CBTs across views into a cluster-specific CBT. Finally, we linearly fuse the cluster-specific CBTs to estimate the final CBT representing a given population. The estimated CBT captures both shared and distinct traits of a population. Ultimately, by simply comparing the CBTs derived from female and male populations, respectively, we spot out gender connectional differences. We demonstrate that the resulting multi-view population-driven CBTs by MVCF-Net fulfill the following criteria: (i) they are well-centered and they achieve the minimum Frobenius distance to all brain views and all subjects in a given population, and (ii) they can effectively differentiate gender fingerprints by capturing the most discriminative brain connections regions between male and female cortices.

### 3.1.2 Feature extraction and similarity networks construction

In this section, we detail the first step of MVCF-Net framework, which aims to extract feature and construct similarity networks. For each view  $m$  we extract the off-diagonal elements of the upper triangular part of each brain network encoded in a symmetric connectivity matrix to form the feature vector  $f_n^m$ . The dimension of each feature vector is thus equal to  $N_f = N_r \times (N_r - 1)/2$ . Next, for each view  $m$ , we define a pairwise distance matrix  $\mathbf{D}_m$  between subjects, where  $\mathbf{D}_m(i, j)$  is the Euclidean distance between subject  $i$  and subject  $j$  using their feature vectors  $f_i^m$  and  $f_j^m$ . We then generate the similarity matrix  $\mathbf{S}_m$  based on the distance (i.e., dissimilarity) matrix  $\mathbf{D}_m$  to capture the similarity strength between each pair of subjects. We denote by  $\mathbf{S}_{i,j}$  the similarity value between subjects  $i$  and  $j$ , where  $\mathbf{S}_{i,j}$  approaches zero when  $i$  and  $j$  are dissimilar. For easy reference, we summarize the major mathematical notations in 3.1.

### 3.1.3 Multi-view clustering using optimization manifolds

Unlike other methods [9] which generate CBTs by directly fusing heterogeneous connectional brain networks of a given population, first, we group subjects into more

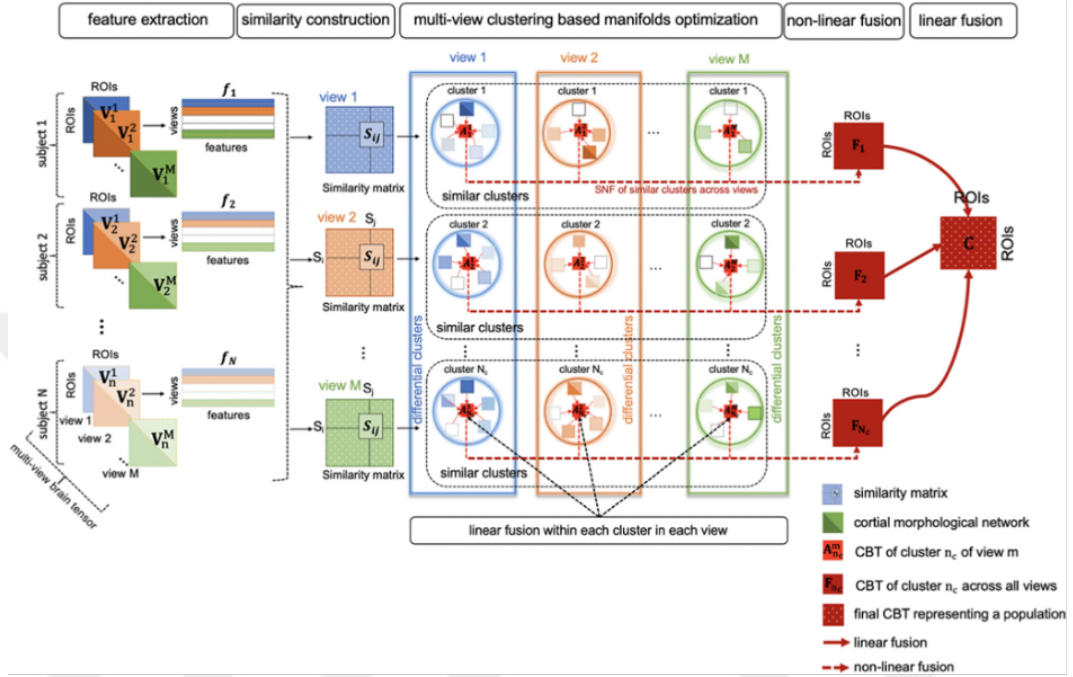


**Figure 3.1 :** Pipeline of the proposed MVCF-Net framework for connectional brain template (CBT) estimation using multi-view brain networks. First, for a given brain network view and for each subject, we extract features by vectorizing the upper off-diagonal part of each brain connectivity matrix. Second, we compute the Euclidian distance between each pair of subjects using their corresponding features vectors to eventually derive a multi-view similarity matrix. Third, we perform multi-view network clustering based on manifold optimization method [6] to partition subjects into shared and differential clusters across views. Fourth, we linearly average all brain networks in each cluster as they lie close to each other, producing local CBTs. Next, for each cluster, we non-linearly fuse its local CBTs across each view using similarity network fusion (SNF) since the local CBTs might lie far from each other. This produces a cluster-specific CBT. Last, we average all cluster-specific CBTs across all clusters, thereby generating the global population CBT.

**Table 3.1 :** Major mathematical notations used in this paper.

Math notation	Dimension	Definition
$M$	$\mathcal{N}$	number of views
$m$	$\mathcal{N}$	view $m$
$n$	$\mathcal{N}$	subject $n$
$\mathcal{M}_m$	-	manifold of $M^{th}$ view, $1 \leq m \leq M$
$N$	$\mathcal{N}$	number of a subject in a given population, $1 \leq n \leq M$
$N_r$	$\mathcal{N}$	number of regions of interest in a brain network (ROIs)
$R_i$	-	region of interest $i$ , $1 \leq i \leq N_r$
$N_c$	$\mathcal{N}$	number of clusters
$N_t$	$\mathcal{N}$	number of iteration in SNF algorithm
$N_f$	$\mathcal{N}$	dimension of feature vector $f_n^m$
$K$	$\mathcal{N}$	number of folds used for cross-validation partition
$K_n$	$\mathcal{N}$	number of the nearest neighbors used for KNN algorithm
$N_{n_c}^m$	-	cluster $n_c$ in $M^{th}$ view, $1 \leq n_c \leq N_c$
$\bar{m}c_i$	$\mathcal{R}$	mean cortical attribute of $R_i$
$\mathbf{V}_n^m$	$\mathcal{R}^{N_r \times N_r}$	brain network of $M^{th}$ view for subject $n$
$\mathbf{D}_m$	$\mathcal{R}^{N \times N}$	distance matrix of $M^{th}$ view
$\mathbf{f}_n^m$	$\mathcal{R}^{N_f \times 1}$	feature vector of $M^{th}$ view for subject $n$
$\mathbf{S}_m$	$\mathcal{R}^{N \times N}$	similarity matrix of $M^{th}$ view
$\mathbf{W}_m$	$\mathcal{R}^{N \times N}$	diagonal matrix of $M^{th}$ view of matrix $\mathbf{S}_m$
$\mathbf{L}_m$	$\mathcal{R}^{N \times N}$	Laplacian matrix of $M^{th}$ view of matrix $\mathbf{S}_m$
$\mathbf{V}_m$	$\mathcal{R}^{N \times N_c}$	assignment matrix of $M^{th}$ view of all subjects into $N_c$ clusters
$\eta_m$	$\mathcal{R}^{N \times N_c}$	eigenvector of $M^{th}$ view of the Laplacian $\mathbf{L}_m$
$\mathbf{V}$	$\mathcal{R}^{N_c \times N_c}$	right singular vectors decomposition of $\mathbf{U}$
$\mathbf{W}$	$\mathcal{R}^{N \times N_c}$	left singular vectors decomposition of $\mathbf{U}$
$\mathbf{U}$	$\mathcal{R}^{M \times N} \times N_c$	representation of $\mathbf{U}_m$ in all network views
$\mathbf{A}_{n_c}^m$	$\mathcal{R}^{N_r \times N_r}$	estimated CBT of cluster $n_c$ in $M^{th}$ view
$\mathbf{P}_{n_c}^m$	$\mathcal{R}^{N_r \times N_r}$	full kernel matrix for $M^{th}$ view and cluster $n_c$
$\mathbf{S}_{n_c}^m$	$\mathcal{R}^{N_r \times N_r}$	sparse kernel matrix for $M^{th}$ view and cluster
$\mathbf{F}_{n_c}$	$\mathcal{R}^{N_r \times N_r}$	fused CBT of cluster $n_c$ across all views
$\mathbf{C}$	$\mathcal{R}^{N_r \times N_r}$	estimated connectional brain template
$q$	$\mathcal{N}$	number of subject in cluster $n_c$
$\mathbf{T}$	$\mathcal{R}$	absolute difference matrix between two CBTs
$\alpha$	$\mathcal{R}$	discriminative score vector of ROIs distinguishing two groups
$\mathbf{y}^m$	$\mathcal{N}$	class label vector of all subjects in $M^{th}$ view
$\mathbf{x}$	$\mathcal{R}^{N_f \times 1}$	weight feature vector of ROIs
$\mathbf{B}$	$\mathcal{R}^{N_n \times N_n}$	discriminative weight matrix of ROIs
KNN	-	K-Nearest Neighbors
SNF	-	Similarity Network Fusion
SVD	-	singular vectors decomposition

homogeneous clusters by leveraging a multi-view clustering model developed by [6], which returns the aligned clusters in each view. Thus, both the consistent clusters and the differential clusters are identified in each view. Specifically, for each manifold  $\mathcal{M}_m$ , we transform the connectional brain networks to similarity matrices that measure the relation between different subjects. Next, for each view, we partition subjects into aligned clusters by solving an optimization problem using the line-search method and then by applying k-means clustering. While the line-search method returns the assignment of subjects into all clusters for each view, k-means clustering method groups subjects into clusters. Thus, the aligned clusters are identified in each view. We detail these steps in the following part. We illustrate in Figure 3.2 multi-view clustering using optimization manifolds of MVCF-Net.

First, we construct the diagonal matrix  $\mathbf{W}_m$  by summing each row of  $\mathbf{S}_m$  as indicated in Eqs. (2) and (3), then perform spectral clustering to solve the optimization model [79] as follows:

$$\mathbf{W}_m = \text{diag}_{1 \leq i \leq N}(\mathbf{S}_i) \quad (3.1)$$

where

$$\mathbf{S}_i = \sum_{j=1}^N \mathbf{S}_{i,j} \quad (3.2)$$

$$\min_{\mathbf{U}_m \in \mathbb{R}^{N \times N_c}} \text{trace}(\mathbf{U}^T \mathbf{L} \mathbf{U}) \quad s.t. \quad \mathbf{U}^T \mathbf{U} = \mathbf{I}_{N_c} \quad (3.3)$$

where

$$\mathbf{L} = \begin{pmatrix} \mathbf{L}_1 & 0 & \cdots & 0 \\ 0 & \mathbf{L}_2 & \cdots & 0 \\ \vdots & \vdots & \ddots & 0 \\ 0 & 0 & \cdots & \mathbf{L}_M \end{pmatrix} - \begin{pmatrix} 0 & \mathbf{I}_n & \cdots & \mathbf{I}_n \\ \mathbf{I}_n & 0 & \cdots & \mathbf{I}_n \\ \vdots & \vdots & \ddots & \mathbf{I}_n \\ \mathbf{I}_n & \mathbf{I}_n & \cdots & 0 \end{pmatrix} \quad (3.4)$$

and

$$\mathbf{U} = \begin{pmatrix} \mathbf{U}_1 \\ \mathbf{U}_2 \\ \vdots \\ \mathbf{U}_M \end{pmatrix} \quad (3.5)$$

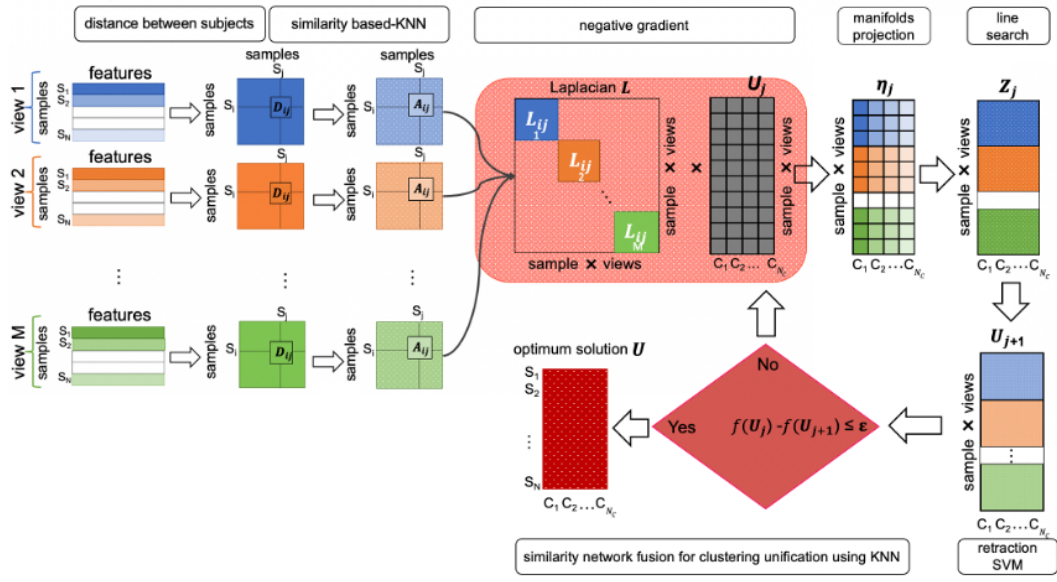


**Figure 3.2 : Multi-view clustering using manifold optimization.** For each view  $m$  lying on a manifold  $\mathcal{M}_m$ , first, we calculate pairwise distance matrix between subjects. Second, for each view  $m$ , we derive the similarity matrices using K-nearest neighbor (KNN) method and compute the Laplacian matrix. Then, for each view  $m$ , we partition all subjects into clusters while preserving their alignment using multi-view spectral clustering. Thus, both consistent and differential clusters can be identified simultaneously. To do that, we solve the optimization problem for each view:  $\min \text{trace}(\mathbf{U}_m^T \mathbf{L} \mathbf{U}_m)$  where  $\mathbf{U}_m$  is a vector representing the initial partition of  $N$  subjects into  $N_c$  cluster. The optimization process includes three steps: first we project the negative gradient on the tangent vector to the manifold  $m$  and we obtain the direction  $\eta_m$ . Second, we update  $\mathbf{U}_m$  by adding a multiple of this direction to its previous measurement. Third, we retract the new  $\mathbf{U}_{m+1}$  to the manifold using single value decomposition. Finally, as  $\mathbf{U}$  converges, we compute k-means clustering to obtain the final label vector partitioning the  $N$  subjects into  $N_c$  clusters for each network view.

where  $N_c$  denotes the putative number of the clusters in each view,  $\mathbf{L}_m = \mathbf{S}_m - \mathbf{W}_m$  is the Laplacian matrix of  $\mathbf{S}_m$  and  $\mathbf{U}_m$  is the assignment matrix of  $N$  subjects into  $N_c$  clusters for view  $m$ . The Laplacian matrix reveals the information about the structure of a graph by showing how many edges are linked to each node (subject), and is used to partition the nodes into clusters by leveraging the Laplacian eigenvectors and eigenvalues in spectral clustering method. Spectral clustering is an effective technique for identifying communities of nodes in a graph based on the edges connecting them. This is achieved by dividing the graph nodes into several groups such that nodes in the same group are similar and nodes in different groups are dissimilar to each other [6]. The first term in the objective function (4) clusters the subjects in each view, while the second term is a constraint to align the clusters in each view. The  $\beta$  is to balance the importance between the network views. Since we treat all views equally, we consider that networks are on the same level and we set  $\beta = 1$ .

To solve the optimization problem (4), we implement the line search algorithm on Stiefel manifold [6] to find the optimal solution of the objective function  $trace(\mathbf{U}^T \mathbf{L} \mathbf{U})$  [80]. This approach includes three steps. First, we project the negative gradient descent direction of the objective function to the tangent vector space of the Stiefel manifold  $\{\mathbf{M}_m = \mathbf{U}_m \in \mathbb{R}^{N \times N_c} : \mathbf{U}_m^T \mathbf{U}_m = \mathbf{I}_{N_c}\}, m = 1, \dots, M$ . The gradient descent of the objective function can be defined in a closed form as:

$$-\nabla_{\mathbf{U}} trace(\mathbf{U}^T \mathbf{L} \mathbf{U}) = -\mathbf{L} \mathbf{U} = (\mathbf{Z}_1^T, \mathbf{Z}_2^T, \dots, \mathbf{Z}_M^T)^T \quad (3.6)$$

For each manifold  $\mathcal{M}_m$ , we compute the orthogonal projection to the tangent vector space to get the direction  $\eta_m$  which represents also the eigenvector of the Laplacian, then we search for the next point by adding a multiple of this direction to the old iteration point.

$$\eta_m = \mathbf{Z}_m - \frac{1}{2} \mathbf{U}_m ((\mathbf{U}_m^T) \mathbf{U}_m + (\mathbf{Z}_m^T) \mathbf{U}_m) \quad (3.7)$$

Second, we associate to the new iteration point a retraction to the manifold using single value decomposition and we get the new assignment vector  $\mathbf{U}_m$  of the  $N$  subjects into  $N_c$  clusters. We keep updating the line search method until the value of vector  $\mathbf{U}_m$  converges to  $\mathbf{U}$ . Finally, we use unsupervised k-means clustering to cluster the

elements in  $\mathbf{U}$ . By taking only the  $k$  eigenvectors corresponding to the  $k$  smallest eigenvalues of  $\mathbf{L}_m$ , we extract the cluster assignment vector which represents the partition of all subjects in the aligned clusters  $C_1^m; \dots; C_{N_c}^m$  for each view  $m$ .

### 3.1.4 Individual-based non-linear fusion of connectional brain network views

To estimate the CBT  $\mathbf{A}_{n_c}^m$  of each cluster  $n_c$  for the  $m_{th}$  view, we linearly average all brain networks of subjects belonging to cluster  $n_c$  in view  $m$ :

$$\mathbf{A}_{n_c}^m = \frac{\sum_{i \in q} \mathbf{V}_i^m}{\dim(n_c)} \quad 1 \leq i \leq N, \quad 1 \leq m \leq M \quad (3.8)$$

where  $q$  is the number of subjects in cluster  $n_c$  for a given view  $m$ .  $q$  can take different values across views and clusters. Next, we merge all  $\mathbf{A}_{n_c}^m$  across  $M$  views using non-linear fusion function  $\Phi$  in order to derive an 'average' connectional brain representation of cluster  $n_c$  across all views:

$$\Phi(\{\mathbf{A}_{n_c}^m\}_{m=1}^M) \mapsto \mathbf{F}_{n_c} \quad (3.9)$$

Ultimately,  $\Phi$  non-linearly maps the view-specific CBTs  $\{\mathbf{A}_{n_c}^m\}_{m=1}^M$  located in different views to a fused brain network  $\mathbf{F}_{n_c}$  of multi-view networks in cluster  $n_c$ . Thus, we integrate networks sharing the same connectional traits from different manifolds (i.e., views), but within a single cluster. To do so, we leverage the similarity network fusion technique (SNF) proposed by [1]. SNF enables the fusion of subjects having common neighbors across views so that complementary information can be propagated through the fusion process. Given a cluster  $n_c$ , for each CBT  $\mathbf{A}_{n_c}^m$  of view  $m$ ,

$$\mathbf{P}_{n_c}^m(i, j) = \begin{cases} \frac{\mathbf{A}_{n_c}^m(i, j)}{2 \sum_{l \neq i} \mathbf{A}_{n_c}^m(i, l)}, & j \neq i \\ \frac{1}{2}, & j = i \end{cases} \quad (3.10)$$

$$\mathbf{P}_{n_c}^m(i, j) = \begin{cases} \frac{\mathbf{A}_{n_c}^m(i, j)}{2 \sum_{l \in N_i} \mathbf{A}_{n_c}^m(i, l)}, & j \neq i \\ 0, & \text{otherwise.} \end{cases} \quad (3.11)$$

Note that  $\mathbf{P}$  carries all information about ROIs similarities of each subject to all other ROIs, whereas  $S$  only encodes the similarity to the  $K_n$  most similar ROIs.  $N_i$  denotes the set of most  $q$  closed ROIs (neighbors) to the target ROI  $R_i$ . To find the set  $N_i$ , we

use the K-nearest neighbors (KNN) algorithm. Next, we compute iteratively the status matrices  $\mathbf{P}_{n_c}^m$  by using the following equation [1]:

$$\mathbf{P}_{n_c}^m = \mathbf{S}_{n_c}^m \times \left( \frac{\sum_{t \neq m} \mathbf{P}_{n_c}^t}{M-1} \right) \times (\mathbf{S}_{n_c}^m)^T, \quad m \in 1, \dots, M \quad (3.12)$$

For each cluster  $n_c$  and view  $m$ , we update the similarity matrix  $\mathbf{P}_{n_c}^m$  by diffusing the global structure of other networks  $\sum_{t \neq m} \frac{\mathbf{P}_{n_c}^t}{M-1}$  along the sparse structure  $\mathbf{S}_{n_c}^m$  of the current view  $m$ . After  $N_t$  iterations, we compute the average of the diffused matrices  $\mathbf{P}_{n_c}^m$  across the different  $M$  views and we get the fused CBT representing the cluster  $n_c$  across views using the following equation:

$$\mathbf{F}_{n_c} = \frac{\sum_{m=1}^M \mathbf{P}_{n_c}^m}{M} \quad (3.13)$$

### 3.1.5 Linear fusion

After obtaining the cluster-based CBTs  $\{\mathbf{F}_{n_c}\}_{n_c=1}^{N_c}$ , we linearly average them into a single final CBT denoted as  $C$ :

$$\mathbf{F}_c = \frac{\sum_{n_c=1}^{N_c} \mathbf{F}_{n_c}}{N_c} \quad (3.14)$$

For easy reference, we detail the steps of the proposed MVCF-Net framework in Algorithm 1 3.2. MVCF-Net Algorithm 1: Joint multi-View Network Clustering and Fusion.

### 3.1.6 Evaluation strategies

We evaluate the performance of our MVCF-Net framework by testing the generated connectional brain template (CBT) in term of (1) representativeness and centeredness, (2) and discriminability. To ensure the reproducibility and the generalizability of our evaluation results, we split each dataset (male (M) and female (F) populations) into training and testing subsets using 5-fold cross-validation. We use the training subset to train our model and to generate CBTs for both hemispheres (LH and RH) of 2 populations namely; M, and F. Next, we showcase MVCF-Net with the aforementioned evaluation tests on the left out testing subset.

#### 3.1.6.1 Evaluation strategy of connectional brain template representativeness

**Table 3.2 :** MVCF-Net Algorithm: Joint Multi-View Network Clustering and Fusion.

Line	Algorithm
1	<b>INPUTS:</b> Set of population brain connectivity network views:
2	$\{\{\mathbf{V}_1^1, \dots, \mathbf{V}_1^m, \dots, \mathbf{V}_1^M\}, \dots, \{\mathbf{V}_n^1, \dots, \mathbf{V}_n^m, \dots, \mathbf{V}_n^M\}, \dots, \{\mathbf{V}_N^1, \dots, \mathbf{V}_N^m, \dots, \mathbf{V}_N^M\}\};$
3	$M$ : number of views;
4	$N$ : number of subjects in the population;
5	$N_c$ : number of clusters;
6	$K$ : number of folds in cross-validation strategy;
7	<b>Feature extraction and similarity networks construction</b>
8	For each subject $n$ , extract the feature vector $\mathbf{f}_n = \{\mathbf{f}_n^1, \dots, \mathbf{f}_n^m, \dots, \mathbf{f}_n^M\}$ ;
9	Calculate the multi-view pairwise distance matrix between subjects using Euclidian distance $\mathbf{D} = \{\mathbf{D}_1, \dots, \mathbf{D}_m, \dots, \mathbf{D}_M\}$ ;
10	Compute the similarity matrices $\mathbf{S} = \{\mathbf{S}_1, \dots, \mathbf{S}_m, \dots, \mathbf{S}_M\}$ based on $\mathbf{D}$ ;
11	Compute the similarity matrices $\mathbf{W} = \{\mathbf{W}_1, \dots, \mathbf{W}_m, \dots, \mathbf{W}_M\}$ ;
12	<b>Multi-view clustering using optimization manifolds [6]</b>
13	<b>Initialization:</b> Compute the Laplacian matrices $\mathbf{L} = \{\mathbf{L}_1, \dots, \mathbf{L}_m, \dots, \mathbf{L}_M\}$ using $\mathbf{S}$ and $\mathbf{W}$ given a starting point $\mathbf{U}^0$ ; $U$ as $N \times M$ points in $\mathcal{R}^{Nc}$
14	Solve the optimization problem using spectral clustering algorithm:
15	Repeat
16	Compute the negative gradient: $-\nabla_{\mathbf{U}} \text{trace}(\mathbf{U}^T \mathbf{L} \mathbf{U}) = -\mathbf{L} \mathbf{U} = (\mathbf{Z}_1^T, \mathbf{Z}_2^T, \dots, \mathbf{Z}_M^T)^T$
17	<b>for</b> $m = 1, 2, \dots, M$ <b>do</b>
18	project the negative gradient to the tangent vector of the manifold $\mathcal{M}_m$ ;
19	$\eta_m = \mathbf{Z}_m - \frac{1}{2} \mathbf{U}_m ((\mathbf{U}_m^T) \mathbf{U}_m + (\mathbf{Z}_m^T) \mathbf{U}_m)$ ;
20	$\eta = (\eta_1^T, \eta_2^T, \dots, \eta_M^T)^T$ ;
21	<b>end for</b>
22	Update the next point: $\mathbf{U} = \mathbf{U} + \alpha \eta$ ;
23	<b>Until</b> $ \mathbf{U}^1 - \mathbf{U}^0  < \epsilon$ ;
24	Retract using singular value decomposition: $\mathbf{U} = \mathbf{W} \mathbf{W}^T$ ;
25	Compute k-means clustering algorithm to get the clusters label of the nodes in each network $m$ : $C_1^m, C_2^m, \dots, C_{N_c}^m$ ;
26	<b>Fusion process of network views</b>
27	<b>for</b> $m = 1, 2, \dots, M$ <b>do</b>
28	<b>for</b> $n_c = 1, 2, \dots, N_c$ <b>do</b>
29	Compute the CBT $\mathbf{A}_{n_c}^m$ by linear fusion of $\{\mathbf{V}_n^m, n \in n_c\}$ ;
30	<b>end for</b>
31	Compute $\mathbf{F}_{n_c}$ the network representing cluster $n_c$ by merging $\mathbf{A}_{n_c}^m$ across views using SNF algorithm [1];
32	<b>end for</b>

```

33 Linear fusion
34 Compute the estimated CBT representing the population by averaging
    $\mathbf{F}_{n_c}$  across clusters;
35 Extraction of ROIs scores using the estimated CBTs of two
   populations  $p$  and  $p'$  and cross-validation strategy
36 for  $i = 1, 2, \dots, K$  do
37   for  $j = 1, 2, \dots, K$  do
38     Compute  $D$  the absolute distance between two estimated
       populations CBT  $\mathbf{A}_i^p$  and  $\mathbf{A}_i^{p'}$ ;
39   end for
40   Compute the weight vector  $\alpha$  representing the discriminative score of
     ROIs by aggregating the elements of each row in the matrix  $D$ ;
41 end for
42 OUTPUTS: Return the estimated CBT of a population and the ROIs
     scores vector between two populations.

```

---

We evaluate both the centeredness and representativeness of the estimated CBT for a given population using two evaluation metrics: (i) the mean Frobenius distance as well as (ii) the Pearson correlation between the estimated CBT and the brain networks of all subjects across views in the given population. For each view  $m$ , we compute the mean Frobenius distance  $d_m^F$  between the estimated CBT and all brain networks, then we calculate the average of  $d_m^F$  across the views. Likewise, we compute the mean Pearson correlation  $r_m$  for each view between the predicted CBT and all brain networks belonging to a given population, then we linearly average  $r_m$  across views. The Frobenius distance and the Pearson correlation between two matrices  $\mathbf{G} = (g_{ij})$  and  $\mathbf{H} = (h_{ij})$  where  $1 \leq i, j \leq N$  are calculated as follow:

$$d_F(\mathbf{G}, \mathbf{H}) = \sqrt{\sum_i \sum_j |g_{i,j} - h_{i,j}|^2} \quad (3.15)$$

$$r(\mathbf{G}, \mathbf{H}) = \frac{\sum_i \sum_j (g_{i,j} - g)(h_{i,j} - h)}{\sqrt{(\sum_i \sum_j |g_{i,j} - g|^2)(\sum_i \sum_j |h_{i,j} - h|^2)}} \quad (3.16)$$

where  $g = \text{mean}(\mathbf{G})$  and  $h = \text{mean}(\mathbf{H})$ . For evaluating the reproducibility of the estimated CBTs, we use K-fold cross-validation for validating and testing. We randomly split each group in the given population of multi-view brain networks into  $K$  sub-populations. For each sub-population, we generate a CBT and we measure its Frobenius distance to views. For better visualization of the results and for easy

comparison between methods, we further normalize the Frobenius distances for each fold using the following formula:

$$d'_F = (d_F - \text{mean}_i) / (\text{max}_i - \text{mean}_i) + 1.5 \quad (3.17)$$

where  $\text{mean}_i$  and  $\text{max}_i$  denote respectively the average and the maximum Frobenius distances in fold  $i$ .

### 3.1.6.2 Evaluation strategy of connectional brain template discriminability

In this part, we aim to test the discriminability of the estimated CBTs by identifying the top brain ROIs that distinguish between two groups. This experiment evaluates the performance of a given method in relation with the discriminability of the ROIs. To do so, we estimate a CBT for each group, then by computing the difference between both templates, we identify the top ROIs distinguishing between both groups. Next, we compute the overlap (in %) between the top discriminative ROIs found by MVCF-Net and a supervised machine learning method based on multiple kernel learning (MKL) Figure 3.3. Both methods are detailed below.

#### Identification of top discriminative ROIs using the estimated CBTs

To assess the reproducibility of our proposed method, we use K-fold cross validation strategy to partition samples in each population (male/female) into  $K$  groups (folds). We denote by  $p_i$  the fold  $i$  of group 1 (e.g., male) and  $p'_j$  the fold  $j$  of group 2, where  $1 \leq i, j \leq K$ . After computing the estimated CBTs of all folds for both populations, we compute the average absolute difference between all  $n$  possible pair combinations of estimated CBTs. Each combination includes CBTs from both fold groups  $p$  and  $p'$ , then we define an  $N_r N_r$  matrix  $\mathbf{T}$  representing the cumulative absolute differences between all pairs of CBTs:

$$T = \sum_{i,j=1}^K |\mathbf{A}_i^p - \mathbf{A}_{i_j}^{p'}|, \quad 1 \leq i, j \leq K \quad (3.18)$$

where  $\mathbf{A}_i^p$  denotes the CBT of group 1 from fold  $i$  and  $\mathbf{A}_{i_j}^{p'}$  is CBT of group 2 from fold  $j$ . By aggregating the elements of each row in  $\mathbf{T}$ , we get the weight score  $\alpha_i$  assigned to the ROI  $R_i$ . The obtained  $\alpha_i$  denotes the cumulative Euclidian distance from  $R_i$  to all other ROIs  $R_j$  ( $j \neq i$ ). Next, we rank the elements in score vector  $\alpha$  decreasingly

to identify the top discriminative ROIs having the highest scores. The pipeline steps of top discriminative ROIs are illustrated in Figure 3.3.

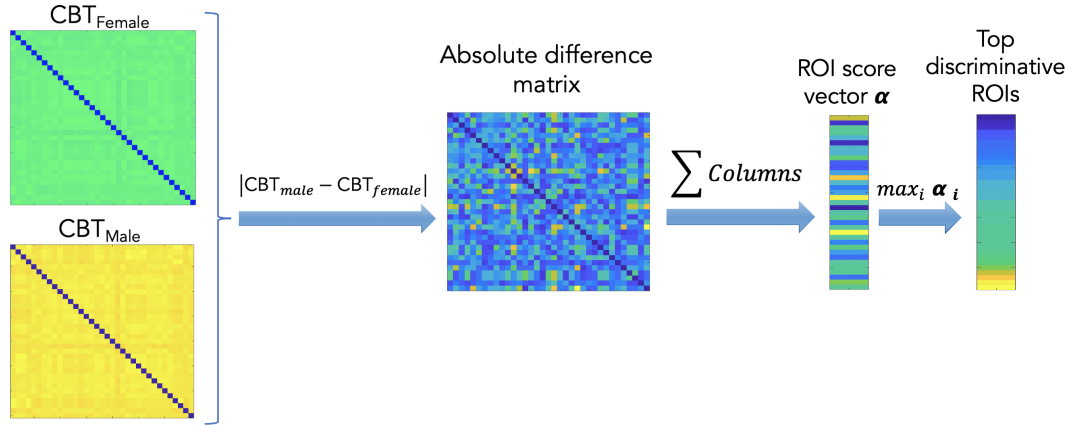


**Figure 3.3 :** *Identification of regions of interest (ROIs) scores using MVCF-Net method.* First, we calculate the absolute difference between two estimated connectional brain templates (CBTs) to generate the absolute difference matrix. Secondly, we aggregate the column elements of each row in the absolute difference matrix to produce a score vector assigning the weight for each ROI. Finally, we decreasingly rank the elements of score vector to get the top discriminative ROIs.

### Reproducibility of top discriminative ROIs

Next, we aim to evaluate the reproducibility of the top discriminative ROIs revealed by two CBTs, each derived from a particular population. To this aim, we propose to use an independent machine-learning methodology for supervised feature selection, namely multiple kernel learning (MKL), and compare the ROIs identified by MVCF-Net and MKL. MKL is a technique that learns an optimal combined kernel from predefined basic kernels (e.g. information coming from multiple sources by maximizing separability between them). Specifically, MKL was shown to be powerful in classification task that distinguishes between classes while identifying the most discriminative features between them [4]. Given a labeled sample with its corresponding feature vector, we train an SVM classifier that learns a weight score for each feature measuring its discriminative power in the target classification task. For each network view  $m$ , we use a  $K$ -fold randomized partition to divide the data into  $K$  subpopulations. Let  $p$  denote population 1 and  $p'$  population 2. For each combination of subpopulations  $p_i$  and  $p'_j$ , where  $1 \leq i, j \leq K$ , we construct a feature vector  $\mathbf{F}_n^m$  for each subject  $n$  in both subpopulations  $p$  and  $p'$  using the vectorized upper triangular part of the connectivity matrix  $\mathbf{V}_n^m$ , and we assign its label  $\mathbf{y}_n^m \in \{1, 2\}$  indicating

the population class. Using  $\mathbf{f}_n^m$ ;  $\mathbf{y}_n^m$  and the subpopulations  $p_i$  and  $p'_j$  as inputs to train the SVM classifier, we use a wrapper method to estimate a weight vector  $\mathbf{x}_{i,j}^m$  which assigns a learned weight quantifying the importance of each feature (i.e., brain connectivity) in distinguishing between two classes. We compute the total weight vector  $\mathbf{x}$  by cumulating  $\mathbf{x}_{i,j}^m$  across all views and all combinations of sub-populations:

$$\mathbf{x} = \sum_{i,j=1}^K \sum_{m=1}^{\bar{M}} \mathbf{x}_{i,j}^m \quad (3.19)$$

We apply anti-linearization to transform the weight vector  $x$  into a square matrix  $B$  where each element  $B(i, j)$  represents the learned weight assigned to brain connections between ROIs  $R_i$  and  $R_j$ . Next, by summing up the weights of all connections involving  $R_i$  to other ROIs, we obtain the weight score  $\alpha_i$  that quantifies the discriminative power of  $R_i$ .  $\alpha_i$  is then calculated as follows:

$$\alpha_i = \sum_{j \neq i} \mathbf{B}(i, j), \quad 1 \leq j \leq N_r \quad (3.20)$$

Finally, we select the top discriminative ROIs using the highest scores  $\alpha_i$ , where  $1 \leq i \leq N_r$ . The identification pipeline of top discriminative ROIs using MKL technique is illustrated in Figure 3.4.

## 3.2 Multigraph Integration and Classifier Networks (MICNet)

### 3.2.1 MICNet overview

Figure 3.5 provides an overview of the key steps of our proposed multigraph integration and classifier networks MICNet which is the first end-to-end learning based graph classification architecture using multigraph fusion. In the first step, we learn a single-view graph representation from each multigraph to disentangle the heterogeneity problem while preserving multigraph topological features. To this aim, we first compute multiple convolutions on the multigraph views at a subject-level. Next, at each layer, we perform a multiplication of a multigraph tensor convolution output and the resulting tensor of the previous layer. After computations of all layers, we then calculate the average of the resulting tensor over the channels to obtain a

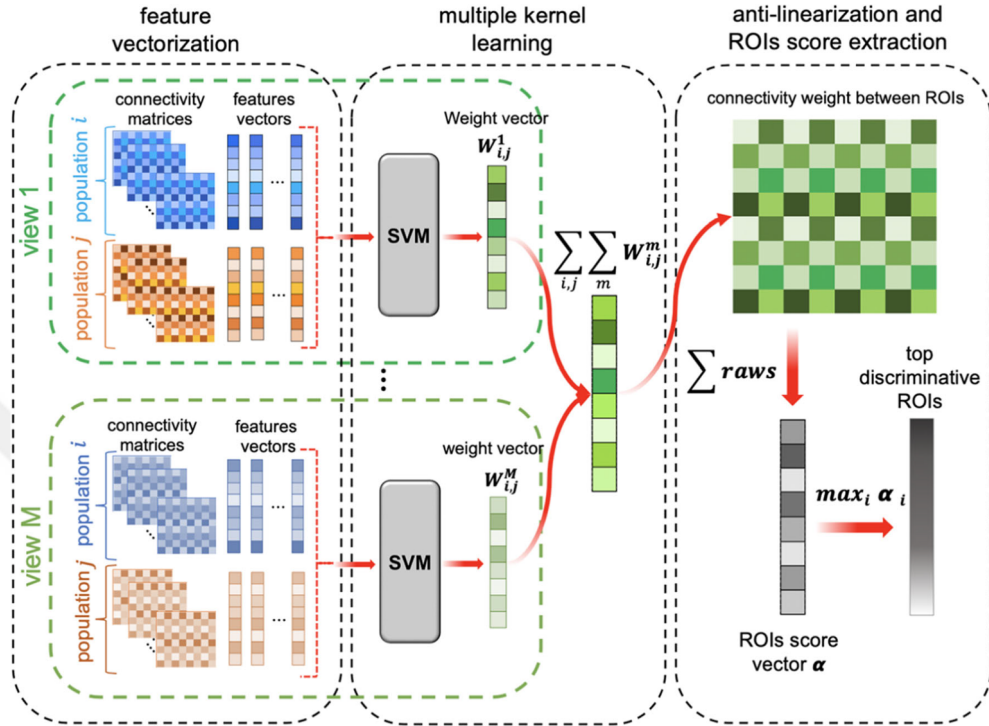


**Figure 3.4 :** Identification of the top discriminative ROIs using multiple kernel learning (MKL). First, we linearize the multi-view brain connection networks for training and testing brain networks through the vectorization of the upper triangular part of each population matrices to generate a feature vector for each brain network. Second, for each view  $m$ , we apply MKL based on support vector machine (SVM) to obtain a weight vector  $\mathbf{x}_m$  quantifying the discriminability of each brain feature (i.e., brain connectivity between two anatomical regions of interest (ROIs)). Next, by summing the weight vectors  $x_m$  across views, we obtain the total weight vector  $\mathbf{x}$  for a particular ROI. We then use anti-linearization to transform the weight vector into a matrix where each element represents the connectivity weight between two ROIs. Specifically, anti-linearization is the inverse of features vectorization where the weight vector represents the upper triangular part of the resulting symmetrical connectivity matrix. By aggregating the columns of the resulting matrix, we obtain the score vector denoting the discriminative power of each ROI. Finally, we rank brain ROIs according to their highest scores.

**Table 3.3 :** Major mathematical notations used in this paper.

Mathematical notation	Definition
$N$	number of multigraphs (subjects)
$n$	number of graph nodes
$n_v$	number of views
$\mathbf{A}_i^{(k)}$	the $i^{th}$ view of the $k^{th}$ subject's adjacency tensor
$y^{(i)}$	real label of the $i^{th}$ subject
$\hat{y}^{(i)}$	predicted label of the $i^{th}$ subject
$n_g$	number of graph integration layers
$n_p$	number of classification pooling layers
$\mathbf{S}^{[i]}$	assignment tensor at the $i^{th}$ layer
$\mathbf{H}^{[i]}$	input embedding tensor at the $i^{th}$ layer
$\mathbf{Z}^{[i]}$	output embedding tensor at the $i^{th}$ layer
$\mathbf{p}$	prediction logits vector

single view-graph after integration of the original views. In the second stage, we introduce these graph templates into a geometric deep learning based classification step to optimally capture the discriminative patterns in graph structure. To do so, we compute a sequence of pooling layers where we run two separate GNN-based architectures to learn new embedding representations for the nodes and their new assignment to the new clusters. After the final pooling layer, we use all the embedding tensors to classify the graph using a dedicated GNN-based architecture.

### 3.2.2 Problem definition

Graphs are data structures with a node set  $V$  and an edge set  $E$ ,  $G = (V, E)$ , where  $E \subset V \times V$ . We denote  $n = |V|$  and  $n_v$  the number of nodes and the number of views, respectively. In this study, we work with undirected graphs having multiple edge attributes. Since our problem is supervised classification of a multigraph set, we denote the label of a graph as  $y$  and its predicted label as  $\hat{y}$ . We represent subjects in the population as a set of tensors  $\{\mathbf{A}^{(i)}\}_{i=1}^N$ . Each tensor  $\mathbf{A}^{(i)} \in \mathbb{R}^{n \times n \times n_v}$  stacks the adjacency matrices of the  $i^{th}$  subject in the dataset. Specifically,  $\mathbf{A}_j^{(i)} \in \mathbb{R}^{n \times n}$  is the  $j^{th}$  view of the  $i^{th}$  subject in the population. In this work, our goal is to conduct an accurate classification for a dataset of labeled multigraphs.

In this section, we detail the components of our MICNet architecture for multigraph integration and classification (Fig 3.5). First, we introduce the integration block that learns the shared connectivity patterns across the multi-view graph tensor to generate

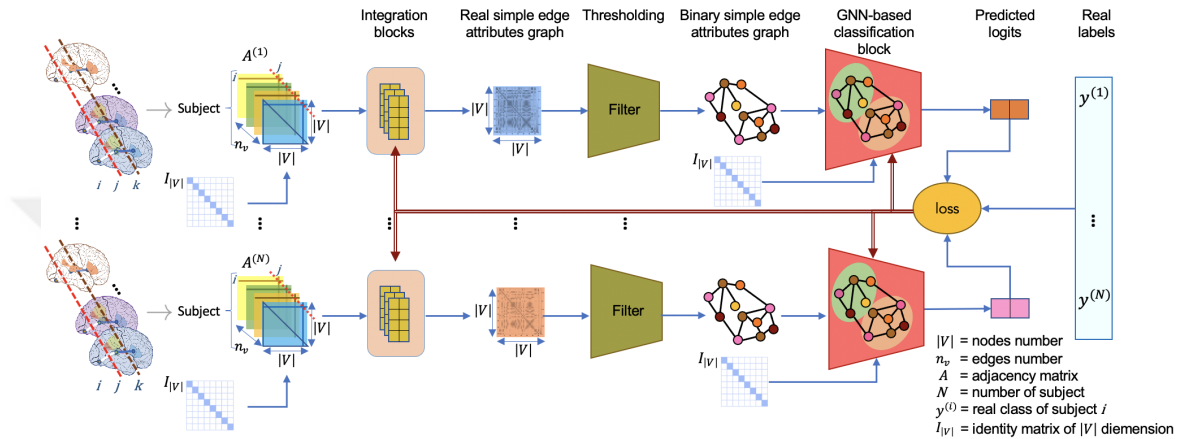


**Figure 3.5 :** *Overview of our multigraph integration and classification (MICNet) architecture.* MICNet performs classification of multigraphs with heterogeneous views. We first integrate a multigraph at a subject-level. The integration block extracts single-view graphs from the original multigraphs. These single-view graphs contain the most relevant edge attributes. Next, we introduce the outputs of the integration block to a subject-specific thresholding filter. This step generates binary matrices representing single-view graphs with binary edge attributes. This step selects the connections having most relevant connectivity weights, thereby emphasizing the most discriminative and representative edges used as subject fingerprints. We feed these graphs to a GNN-based classification architecture which performs several graph convolutions to get final prediction. We transform the single-view graph through a sequence of embedding and pooling layers into predicted labels.

subject-level integrated graphs (i.e., template graphs). Second, we apply thresholding filters at a subject level to generate binary adjacency matrices. Third, we perform a classification step that stacks multiple graph convolutions and graph neural layers to obtain the final classification prediction.

### 3.2.3 Multigraph integration and thresholding step

The input of the integration block is a multigraph with heterogeneous views and different edge types. Let  $\mathbf{A} \in \mathbb{R}^{n \times n \times n_v}$  be the set of input tensors representing the multigraphs. The output of this block is an  $n \times n$  matrix which represents the single view integrated graph. The integration block was inspired by graph transformer networks proposed in [74] for node classification. Here we adapt it to perform a graph integration task. The goal of our integration block is to transform an input tensor which represents a multigraph  $\mathbf{A} \in \mathbb{R}^{n \times n \times n_v}$  to a single view graph which is an  $n \times n$  matrix representing the integrated subject-specific template.

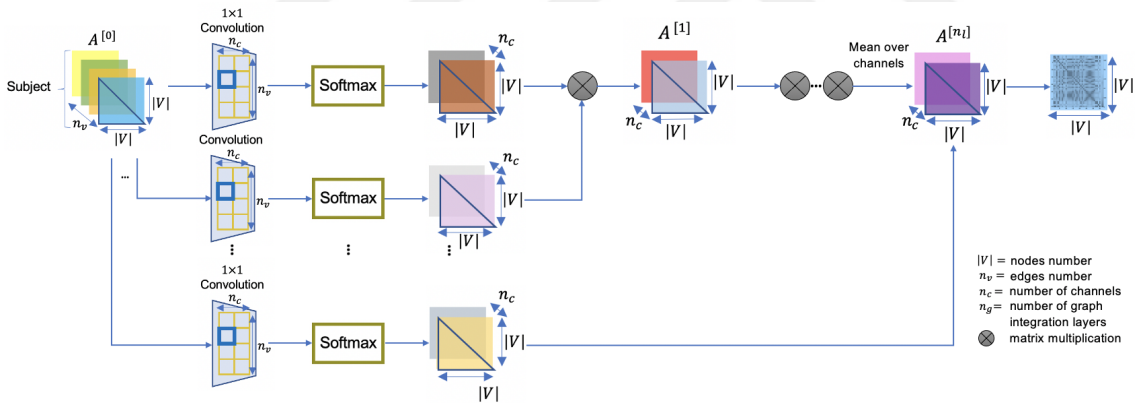


**Figure 3.6 :** *Multigraph integration pipeline.* For a given multigraph, this block consists in the fusion of the multigraph views at a subject-level. We compute the subject-level integrated template by stacking different convolution operations. At each layer, we perform a multiplication of a multigraph tensor convolution output and the resulting tensor of the previous layer. After computations of all layers, we calculate the mean of the resulting tensor over the channels. The resulting tensor represents a single view-graph obtained after integration of the original views.

The multigraph fusion is done by the exploration of the graph meta-paths [74]. Meta-paths can be used to highlight relationships between multiple nodes related through different edge types. They can be useful to identify hidden or complex

patterns lying in more than one view specially when dealing with multigraphs with heterogeneous edge types. Given a node of a multigraph, meta-paths can be decisive to explore the relevant edges that connects it with its neighborhood through the heterogeneous views. The meta-path extraction can be a hard task when dealing with relatively high-dimension multigraphs. We can define the meta-path graph by its adjacency matrix  $\mathbf{A}_\delta$ , describing the connections between the nodes with a relation that represents the meta-path  $\delta$  as follows:

$$\mathbf{A}_\delta = \mathbf{A}_{\delta_p} \dots \mathbf{A}_{\delta_2} \mathbf{A}_{\delta_1} \quad (3.21)$$

where  $p$  denotes the number of edge types included in the meta-path  $\delta$ . The adjacency matrix using the meta-path  $d$  can be seen as a multiplication of the adjacency matrices  $\{\mathbf{A}_{\delta_j}\}_{j=1}^p$  where  $\delta_j$  is the  $j^{th}$  edge type included in the meta-path  $\delta$ . To obtain adjacency matrices with meta-paths, our model computes several multiplications of convolutions of the original adjacency matrices. For the initial layer, our integration block performs the multiplication of two convolutions of the original input tensor as follows:

$$\mathbf{A}^{[1]} = \phi_0(\mathbf{A}^{[0]}, \text{softmax}(\mathbf{W}_{\phi_0})) \phi_1(\mathbf{A}^{[0]}, \text{softmax}(\mathbf{W}_{\phi_1})) \quad (3.22)$$

where  $\mathbf{W}_{\phi_0}, \mathbf{W}_{\phi_1} \in \mathbb{R}^{n_c \times n_v \times 1 \times 1}$  are the learned weight matrices corresponding to the two separate  $1 \times 1$  convolutions used at the 1<sup>st</sup> layer  $\phi_0$  and  $\phi_1$ , respectively.  $n_c$  is a parameter indicating the number of channels used in the convolution.

For the following layers, our model computes the multiplication of the output of the last layer and the convolution's output of the original tensor as:

$$\mathbf{A}^{[i]} = \mathbf{A}^{[i-1]} \phi_i(\mathbf{A}^{[0]}, \text{softmax}(\mathbf{W}_{\phi_i})), i > 1 \quad (3.23)$$

where  $\mathbf{A}^{[i]} \in \mathbb{R}^{n \times n \times n_c}$  is the resulting tensor from the  $i^{th}$  layer.  $\mathbf{W}_{\phi_i} \in \mathbb{R}^{n_c \times p \times 1 \times 1}$  is the learned weight matrix of the  $1 \times 1$  convolution  $\phi_i$  used at the layer  $i$ .  $\mathbf{A}^{[i]}$  represents the meta-paths learned for the multigraph tensor  $\mathbf{A}$  until the  $i^{th}$  layer. Next, we compute the mean over channels of the tensor resulting from the last layer. The resulting tensor is an  $n \times n$  matrix which represents the subject-level integrated graph. The obtained

graph contains the meta-paths learned following multiple convolutions during the integration process. The meta-paths are the most relevant relationships containing different edge types. The resulting tensor is a single-view graph  $\mathbf{A} = (a_{ij}) \in \mathbb{R}^{n \times n}$ .

Next, we conduct a thresholding to emphasize the edge attributes that have more impact on the classification output. We threshold the integrated subject-level templates using a specific filter that keeps the edges having the highest connectivity weights. This filter extracts a binary matrix from the integrated template. We aim to remove weak connections that can be irrelevant. Hence, we only preserve the most pertinent edges. We perform two methods of filters: mean-based and median-based thresholdings. For each method, we compare the weights with the threshold and make the following transformation:

$$a_{i,j} = \begin{cases} 1, & \text{if } a_{i,j} \geq t \\ 0, & \text{if } a_{i,j} < t \end{cases} \quad (3.24)$$

where  $t$  is the threshold chosen for the adjacency weights specific to the graph represented by the tensor  $\mathbf{A} = (a_{i,j})$ . Consequently, we obtain a binary matrix for each subject representing the new integrated template which will be injected in the classification model. Furthermore, we will show in the following sections that the thresholding step has an important contribution to the global performance of our MICNet architecture.

### 3.2.4 Multigraph classification

Following the thresholding of the fused subject-specific template, we obtain a single-view graph. This graph has only one edge type and the edge weights are binary with an adjacency matrix  $\mathbf{A}^{(k)} \in \{0, 1\}^{n \times n}$  where  $k \in \{1, \dots, N\}$  is the index of the graph in the dataset. In this section we describe the different classification blocks used by our model. We will compare the contributions of each classifier to our whole end-to-end model performance in the results section.

#### 3.2.4.1 Classification with hierarchical embedding

We build a GNN-based graph classification model. Our model defines an end-to-end strategy that stacks multiple layers of GNN modules to learn a differentiable soft

cluster assignment for nodes. Each GNN architecture contains multiple stacked graph convolutions parametrized based on these hyperparameters: hidden dimension, assign ratio and output dimension denoted as  $h, a$  and  $o$ , respectively. In each layer  $i$ , we generate the new adjacency matrix and node embedding matrix of the newly coarsened graph by the following equations:

$$\mathbf{H}^{[i+1]} = \mathbf{S}^{[i]\mathbf{T}} \mathbf{Z}^{[i]} \quad (3.25)$$

$$\mathbf{A}^{[i+1]} = \mathbf{S}^{[i]\mathbf{T}} \mathbf{A}^{[i]} \mathbf{S}^{[i]} \quad (3.26)$$

where  $\mathbf{H}^{[i]} \in \mathbb{R}^{|V|a^i \times (2h+o)}$  and  $\mathbf{A}^{[i]} \in \mathbb{R}^{|V|a^i \times |V|a^i}$  for  $i > 0$ . In each layer  $i$ , we compute the new adjacency matrix and node embedding matrix using two tensors learned through the classification model which are the embedding tensor  $\mathbf{Z}^{[i]} \in \mathbb{R}^{|V|a^i \times (2h+o)}$  and the assignment tensor  $\mathbf{S}^{[i]} \in \mathbb{R}^{|V|a^i \times |V|a^{i+1}}$  in Table 3.3.

These two tensors  $\mathbf{Z}$  and  $\mathbf{S}$  are generated through two separate GNN-based architectures. The embedding tensor  $\mathbf{Z}$  is responsible for the new node embeddings and obtained through this equation:

$$\mathbf{Z}^{[i]} = GNN_{i,embed}(\mathbf{A}^{[i]}, \mathbf{H}^{[i]}) \quad (3.27)$$

On the other hand, the assignment tensor  $\mathbf{S}^{[i]}$  at the  $i^{th}$  layer generates assignments of the nodes of the previous layer to the new clusters.

$$\mathbf{S}^{[i]} = softmax(GNN_{i,pool}(\mathbf{A}^{[i]}, \mathbf{H}^{[i]})) \quad (3.28)$$

Noting that in our case, we initialize  $\mathbf{H}^{[0]} = \mathbf{I}_n, \mathbf{A}^{[0]} = \mathbf{A}$ , this whole process can be repeated  $n_p$  times where  $n_p$  corresponds to the number of the pooling layers. After the final pooling layer, another GNN is performed to vectorize the embedding tensors and generate the final prediction of our model.

$$\mathbf{p} = GNN_{pred}(\mathbf{Z}^{[n_p]}, \mathbf{Z}^{[n_p-1]}, \dots, \mathbf{Z}^{[0]}) \quad (3.29)$$

where  $\mathbf{p} = (p_j) \in \mathbb{R}^{l \times 1}$  is the prediction vector containing the prediction logits where  $l$  is the number of classes in the dataset.  $\mathbf{p}$  is computed by  $GNN_{pred}$  a GNN-based

architecture that takes as input the embedding tensors of all the pooling layers of the classification block. The predicted label of the classification is the index of the maximum value in the final prediction vector.

$$\hat{y} = \underset{j}{\operatorname{arg\,max}} p_j = \{j \mid p_j = \max_{j'} p_{j'}\} \quad (3.30)$$

### 3.2.4.2 Graph convolution networks (GCN) classifier

GCN performs a sequence of graph convolution layers. In the literature, there are variant implementations of GCN [3]. These implementations differ by the propagation rule used in every neural network layer  $\mathbf{H}^{[i+1]} = f(\mathbf{H}^{[i]}, \mathbf{A})$  where  $\mathbf{H}^{[i+1]}$  is the graph-level output of the  $(i+1)^{th}$  layer. Here we choose the propagation rule proposed in [3]:

$$f(\mathbf{H}^{[i]}, \mathbf{A}) = \sigma(\hat{\mathbf{D}}^{-\frac{1}{2}} \hat{\mathbf{A}} \hat{\mathbf{D}}^{-\frac{1}{2}} \mathbf{H}^{[i]} \mathbf{W}^{[i]}) \quad (3.31)$$

with  $\hat{\mathbf{A}} = \mathbf{A} + \mathbf{I}$  where  $\mathbf{I}$  is the identity matrix and  $\hat{\mathbf{D}}$  is the diagonal node degree matrix of  $\hat{\mathbf{A}}$ .

### 3.2.4.3 Loss

The loss function of our MICNet model aims to minimize the error between the real labels of our multi-view graphs subjects and the model's predicted labels. We only introduce the prediction logits and the real labels to the loss function. In our model, we use the cross-entropy loss to improve the global performance of our model.

$$\mathcal{L} = -\frac{1}{N} \sum_{i=1}^N (y^{(i)} \log(\hat{y}^{(i)})) \quad (3.32)$$

where  $y^{(i)}$  and  $\hat{y}^{(i)}$  are the real class and the predicted class of  $i^{th}$  subject, respectively.  $N$  is the total number of subjects in a given population. This loss takes into consideration the weights of both classification and integration layers. The design of our model loss ensures that our proposed method works in an end-to-end fashion by learning the weights of all layers through backpropagation. During a single backward pass,

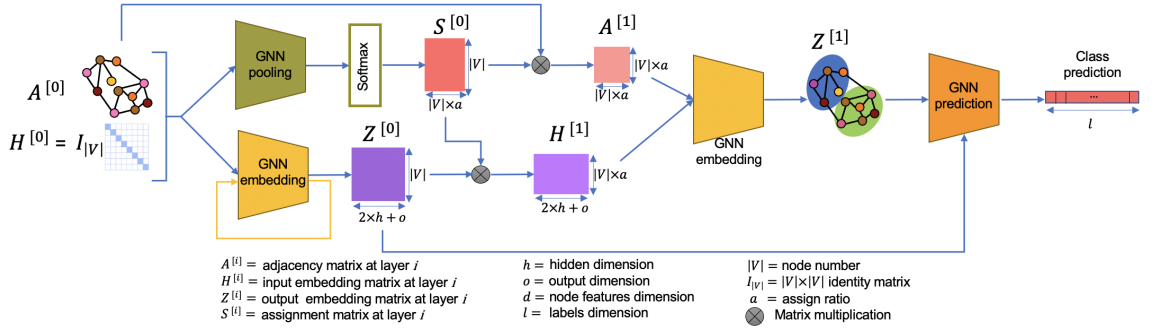


**Figure 3.7 :** Illustration of our proposed MICNet graph classification model with one pooling layer. We initialize  $\mathbf{A}^{[0]}$  as the adjacency matrix of the graph obtained after thresholding step and  $\mathbf{H}^{[0]}$  as an identity matrix  $\mathbf{I}_n$ . On one hand, we run a GNN-based architecture to obtain the embedding tensor  $\mathbf{Z}^{[0]}$ . Then, we multiply  $\mathbf{Z}^{[0]}$  by  $\mathbf{A}^{[0]}$  to obtain the new adjacency matrix  $\mathbf{A}^{[1]}$ . On the other hand, we run another GNN-based architecture to get the assignment matrix  $\mathbf{S}^{[0]}$  containing the new nodes representation in the new clusters. Next, we multiply  $\mathbf{Z}^{[0]}$  by the softmax output of  $\mathbf{S}^{[0]}$  to get the new nodes embedding matrix  $\mathbf{H}^{[1]}$ . We run a separated GNN-based architecture using  $\mathbf{Z}^{[1]}$  and  $\mathbf{H}^{[1]}$  to obtain the updated output embeddings tensor of nodes  $\mathbf{Z}^{[1]}$ . This whole process represents the  $1^{st}$  pooling layer and it is repeated  $n_p$  times. After the final layer computations, we use all the embedding tensors  $\{\mathbf{Z}^{[i]}\}_{i=0}^{n_p}$  to classify the graph using a dedicated GNN-based architecture.

our model updates all its weights to optimize the classification performance in an end-to-end manner.

### 3.3 CBT Estimation Methods

We present the first review paper which provides an insightful survey of the existing integration models promoted with a comparative study to evaluate their performance across extensive experiments in terms of producing the most centered templates, recapitulating unique traits of populations, and preserving the complex topology of biological networks. In our search for articles that introduce graph integration methods, we emphasize two categories which estimate a unified connectional representation of a population of networks. The first category corresponds to the single-view fusion methods where they take populations of single-view networks and output single CBTs. For this category, we identify three single-view graph fusion methods: SNF [1], NAG-FS [7], and SM-netFusion [8]. These fusion methods are

based on different machine learning (ML) architectures.

The second group represents multi-view graphs integration methods which fuse populations of multi-view networks into a single connectional template. For this category, we review five multigraph fusion methods: netNorm [2], SCA [9], MVCF-Net [10], cMGI-Net [20], and DGN [11]. Multigraph fusion methods can be sub-categorized into two big classes: machine learning-based and deep learning-based models. The source articles are published between 2018 and 2020, except the one proposed by [1] in 2014. In the following section, we detail the architecture of each graphs integration method for both categories. We refer the reader to our GitHub link where all papers cited in our work are available at <https://github.com/basiralab/Multigraph-and-Single-View-Integration-in-Network-Neuroscience>.

The aforementioned integration frameworks are graph-based models which are designed to learn from a brain graph where nodes represent anatomical brain regions and edges denote the morphological connectivities. Integration models aim to generate a representative template which encodes a holistic mapping of shared traits within a population of brain multigraphs (single-view graphs). This problem can be defined as follows. Let sample  $s$  (brain connectome) in a population be represented by a set of  $n_v$  weighted undirected graphs with  $n_r$  nodes. We model this sample as a single tensor  $\mathcal{T}_s \in \mathbb{R}^{n_r \times n_r \times n_v}$  that is composed of stacked  $n_v$  adjacency matrices  $\{\mathbf{X}_s^v\}_{v=1}^{n_v}$  of  $\mathbb{R}^{n_r \times n_r}$  capturing the pairwise relationships between  $n$  ROIs. The objective of these fusion frameworks is to integrate a set of multi-view (single-view) graphs  $T = \{\mathcal{T}_1, \mathcal{T}_2, \dots, \mathcal{T}_N\}$  in order to obtain a population-representative connectional template  $\mathcal{T} \in \mathbb{R}^{n_r \times n_r}$  that is well-centered (2) discriminative, and (3) topological sound (topological pattern are preserved when transforming a population of multi-view (single-view) networks to a unique and generic connectional template).

### 3.3.1 Single-graph fusion methods

**SNF.** Similarity network fusion (SNF), proposed by [1], is a generic unsupervised technique for non-linear network integration, which is based on message passing

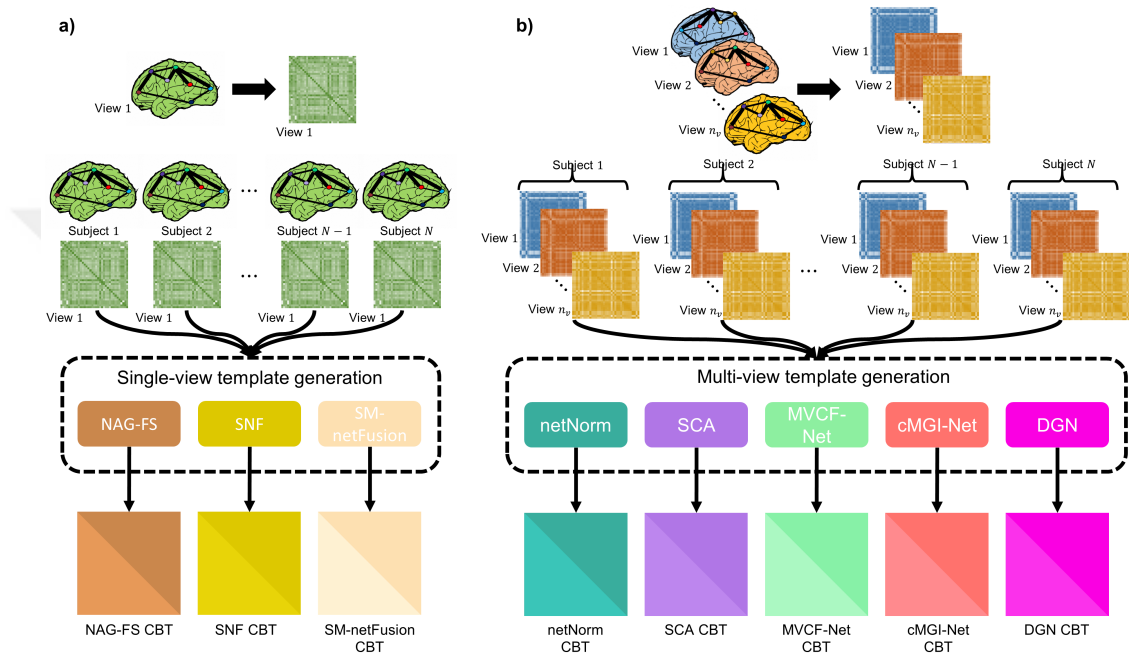


**Figure 3.8 :** The schema illustrates connectional brain templates (CBTs) estimated by **a)** single-graph fusion methods for a given population of single-view brain networks: network atlas-guided feature selection (NAG-FS) [7], similarity network fusion (SNF) [1] and supervised multi-topology network cross-diffusion (SM-netFusion) [8]; and **b)** multi-graph integration methods for a population of multi-view connectomic brain data: multi-view networks normalizer (netNorm) [2], SNF-Clustering-Average (SCA) [9], multi-view clustering and fusion (MVCF-Net) [10], cluster-based multi-graph integrator networks (cMGI-Net) [11].

theory [81]. SNF aims to estimate a status matrix for each network that carries the whole networks information and a sparse local matrix that only takes up to top-k neighbors into consideration. Next, an iterative integration step is conducted to update each status network by diffusing the mean global structure of the remaining networks and along with the sparse local network. The obtained single similarity network captures both shared and complementary information from different data sources.

**NAG-FS.** Network atlas-guided feature selection (NAG-FS) method, proposed by [7], is a feature selection-based method to produce a unified normalized connectional representation of a population of brain networks. First, NAG-FS clusters similar brain networks into non-overlapping subspaces using multiple kernels. Then, NAG-FS leverages the network diffusion and fusion techniques introduced in [1] to nonlinearly fuse the networks lying in the same subspace, hence creating a cluster-specific network atlas. (i.e., a population center). Last, the population connectional network atlas is obtained by non-linearly diffusing and fusing network atlases. NAG-FS captures potential data distribution heterogeneity with different bandwidths.

**SM-netFusion.** Supervised multi-topology network cross-diffusion (SM-netFusion), proposed recently by [8], is a supervised fusion method for CBT estimation from single-view networks of a population based on graph topological measures. SM-netFusion uses a weighted mixture of multi-topological measures to enhance the non-linear fusion process for supervised graph integration. First, SM-netFusion learns a weighted combination of the topological diffusion kernels derived from degree, closeness and eigenvector centrality measures in a supervised manner. Then, SM-netFusion non-linearly cross-diffuses the normalized brain networks so that all diffused networks lie close to each other for the final fusion step to generate the target of a specific population. This normalization well captures the shared networks between individuals at different topological scales, improving the representativeness and centeredness of the estimated multi-topology CBT.

### 3.3.2 Multigraph fusion methods

**SCA.** Starting with the SNF-Clustering-Average (SCA) introduced by [9], is a multi-view brain connectivity fusion framework for estimating a brain network atlas of multi-view brain networks population. Specifically, SCA non-linearly fuses multi-view networks into a single network for each subject. In this step, all individuals are diffused from the original space into the mapped space where their brain views are unified individually by leveraging the generic similarity network fusion (SNF). Then, it clusters the fused networks in the mapped space to identify individuals sharing similar connectional traits in an unsupervised way, which are next averaged within each cluster to generate a representative network atlas for each cluster. After obtaining the cluster-based brain templates, SCA constructs the final multi-view network atlas by linearly averaging the obtained templates of all clusters into a single template denoting the multi-view network atlas.

**netNorm.** A recent selective technique, netNorm introduced by [2], builds a representative template based on graph feature selection prior to a non-linear fusion to integrate multi-view networks. First, netNorm defines a cross-view feature vector between each pair of ROIs for each individual in the population. Then, in order to investigate the inter-relationship between different subjects in a population at local scale, this framework constructs a high-order graph for each pairwise connection by measuring the Euclidean distance between the cross-view feature vectors across all subjects. Next, netNorm selects the most centered cross-view connectional features across the population, which will compose the new significant edges for each network view. Finally, the network views are integrated into a single network using non-linear fusion technique to generate brain connectional template.

**MVCF-Net.** More recently, [10] proposed multi-view clustering and fusion (MVCF-Net), a graph-based clustering method, to fuse a population of multi-view networks. This method is rooted in the identification of consistent and differential clusters across brain views to generate a connectional brain template for a given population. To this aim, first, MVCF-Net leverages multi-view network clustering model based on manifold optimization method [6], which groups similar subjects

in the same cluster and separates dissimilar subjects in different clusters while preserving their alignment across data view. Thus, similar connectional traits and distinct connectional traits of samples within and across clusters nested in different views can be identified in an unsupervised way [6]. Then, for each view, MVCF-Net linearly fuses the networks within each cluster to generate local CBT and non-linearly integrates the resulting local CBTs across views into a cluster-specific CBT. Next, by linearly fusing the cluster-specific centers, the final CBT is estimated to represent a given population of multi-graph networks. MVCF-Net jointly captures simultaneously similar and distinct connectional traits of samples.

*cMGI-Net.* More recently, [20] proposed a clustering-based multi-graph integrator network (cMGI-Net) for CBT estimation of multigraph population. Based on geometric deep learning, cMGI-Net non-linearly maps a population of brain multigraphs to a target CBT in an end-to-end manner using single objective loss function to optimize. First, cMGI-Net clusters similar samples together using multi-kernel manifold learning (MKML) introduced in [82] to disentangle the heterogeneity of the population and facilitating the following integration task. Then, for each cluster, cMGI-Net integrates multigraph network of each subject into a single graph to identify useful edge types between connected nodes. This step results in generating metapaths for each subject which can be very useful to encapsulate representative connections across multigraph networks. Next, cMGI-Net fuses the generated subject-specific graphs into a cluster-specific CBT while learning their weights under the constraint of minimizing the distance between the resulting template and all multigraph networks of the population. The final CBT is estimated by simply averaging the cluster-specific CBTs.

*DGN.* Another very recent approach, deep graph normalizer (DGN) introduced by [11], is a GNN-based architecture that learns how to normalize and integrate a population of multigraph brain networks into a single CBT. First, each training sample passes through a sequence of graph convolutional neural network layers which are separated by non-linear activation of the previous layer. Precisely, each GNN layer learns deeper embeddings for each node by locally integrating connectivities offered

by different heterogeneous views and blending the previous layer's embeddings using integrated connectivities. Next, DGN computes the pairwise absolute difference of each pair of the final layer's node embeddings to derive connectivity weights of the generated CBT. To evaluate the representativeness of the estimated subject-biased CBT, DGN integrates a randomized weighted loss function (SNL) which updates the model weights in a way that generated CBT represents a random subset of the training views set. Specifically, the trained model is fed with an arbitrary subject of the training population and learns how to achieve subject-to-population mapping thanks to SNL optimization. The obtained CBT is refined by selecting the element-wise median of all training CBTs to retain the most centered connections for the final CBT generation.

### **3.3.3 CBT evaluation measures**

Ideally, a reliable estimated template should preserve the topological patterns and properties of a specific population during the fusion process [75]. In more details, a CBT should satisfy the following criteria: (1) centeredness as it occupies the 'center' of a population by achieving the minimum distance to all population samples. (2) graph-derived biomarker reproducibility as it allows to identify connectional biomarkers that disentangle the differences in brain connectivity between populations with different brain states (i.e., healthy and disordered or genders). (3) graph global-level similarity as it tests whether the generated CBT preserves the global structure of the original graphs networks. (4) graph node-wise similarity as it tests whether the local structure of the original data which includes the relationship (connectivity) between the nodes are preserved by the CBT. (5) graph distance-base similarity as it quantifies the distance (similarity score) between two networks by studying some characteristics.

To evaluate the centeredness of the CBTs, we measure the Frobenius distance from the estimated template to each tensor view of each subject in the population. Based on graph theory approach, to compare the aforementioned criteria of graph networks and further on the performance between the graph fusion methods, it is mandatory to quantify the similarity between them [83, 84] using graph theoretical measures.

However, applying this task on complex networks such brain networks is difficult and may fail to encapsulate in a single score because of their heterogeneous composition. To overcome this limitation, we integrate in our CBTs comparison a combination of methods and metrics that evaluate multiple levels in a graph: the nodal level (brain regions), the local level and the global level of a graph network [85–89]. In the rest of this section, we detail the five criteria for CBTs comparison, their evaluation methods and metrics.

### 3.3.3.1 CBT centeredness test

We evaluate the centeredness and representativeness of the estimated CBT by measuring the mean Frobenius distance from the estimated template to each tensor view of each subject for a given population. Frobenius distance between two matrices  $\mathbf{A}$  and  $\mathbf{B}$  is a scalar value and is calculated as:  $d_F(\mathbf{A}, \mathbf{B}) = \sqrt{\sum_i \sum_j |\mathbf{A}_{ij} - \mathbf{B}_{ij}|^2}$ . For reproducibility and generalizability, we split the datasets into training and testing sets using 5-fold cross-validation. We use the training set to generate a connectional template and to calculate its mean Frobenius distance to all views of each sample within the testing left-out fold. Hence, for each population (i.e., AD), we generate 5 CBTs, with an additional one using the whole data. To assess the statistical significance of each single-view fusion method and multigraph fusion method, we validate the comparative study of the CBT centeredness using two-tailed paired t-test across all data folds in addition to the whole data between the comparative methods.

### 3.3.3.2 CBT discriminativeness reproducibility test

Our second criterion is that the generated templates are discriminative which means that CBTs will encapsulate the most distinctive traits of a population of graph networks. To test the discriminability of the estimated CBTs, we first spot the most  $k$  discriminative brain ROIs where a population  $p^A$  CBT largely differs from a population  $p^B$  CBT (i.e., (1) AD vs. LMCI, and (2) M vs. F). To do so, we compute the absolute difference between both estimated templates  $p^A$  and  $p^B$ , respectively. To assess the reproducibility of the CBT produced by each graph fusion method, we use randomized  $k$ -fold partition to divide each population into  $k$  folds.  $\mathbf{A}_i$  and  $\mathbf{B}_i$  denote the estimated CBTs for the  $i^{th}$  fold for population  $p^A$  and the  $j^{th}$  fold for population  $p^B$ , respectively, where  $1 \leq i, j \leq k$ . We compute the mean absolute difference

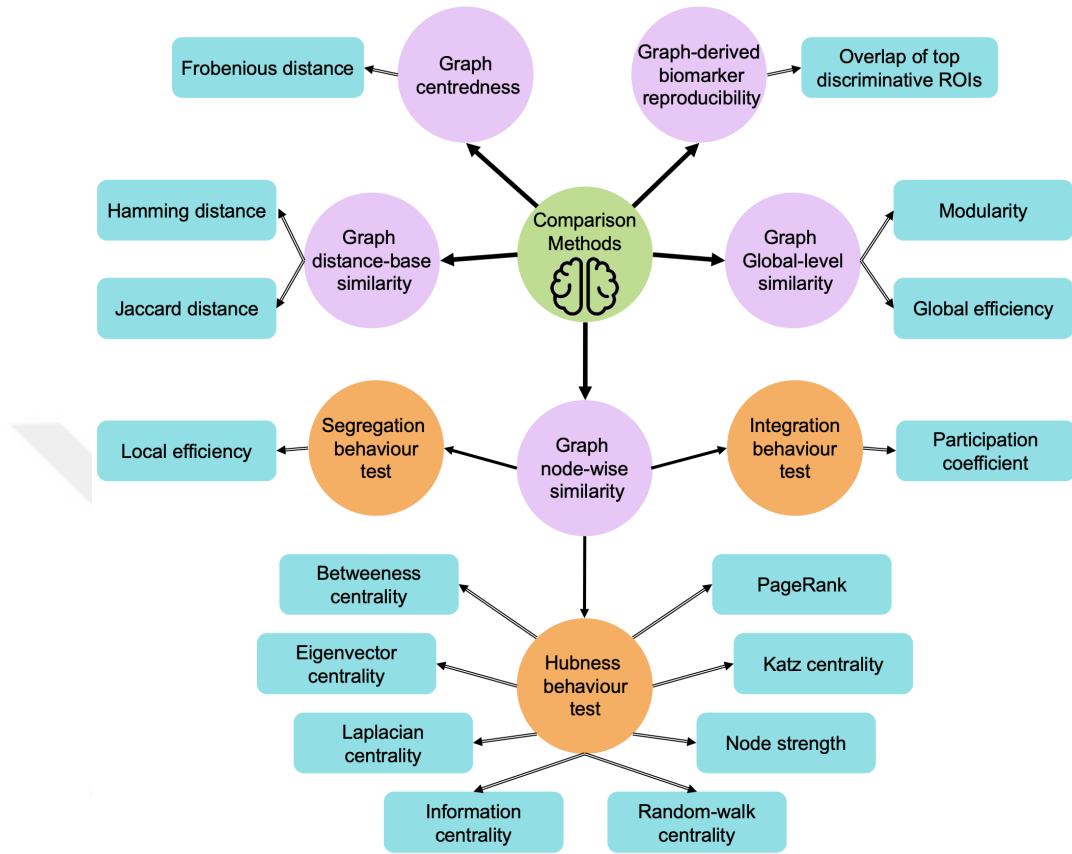


**Figure 3.9 :** Diagram illustrating the criteria used to evaluate the performance of the connectional brain templates generated for single-view graph integration methods and multi-view graphs fusion methods. This includes first graph centeredness using Frobenius distance, second the graph-derived biomarker reproducibility where we identify the overlap of top  $k$  discriminative nodes (ROIs) computed by the graph fusion methods and by an independent biomarker selection method, third the global-level similarity using both modularity and global efficiency measures, fourth the graph distance-based similarity where we compute Hamming and Jaccard distances. Finally, we include the graph node-wise similarity where we evaluate three behavior for the graph: integration behavior using participation coefficient, segregation behavior using local efficiency, and hubness behavior using the following centrality metrics: PageRank [12], Katz centrality [13], node strength [14], random-walk centrality [15], information centrality [16], Laplacian centrality [17], eigenvector centrality [18], and betweenness centrality [19].

between the estimated templates across folds using simple inter-template subtraction as follows:  $\mathbf{D} = \sum_{i,j} |\mathbf{A}_{ij} - \mathbf{B}_{ij}|$ ,  $1 \leq i, j \leq k$ , where  $\mathbf{D}$  is an  $n_r \times n_r$  matrix containing the absolute features' differences between all pairs of fold  $i$  and fold  $j$  in terms of connectional strength. Next, we sum the columns of the resulting difference matrix to obtain a discriminability score vector  $\alpha$  where the  $i^{th}$  coefficient denotes the score  $\alpha_i$  assigned to the  $i^{th}$  ROI representing the cumulative distance from ROI  $i$  to all other ROIs  $k \neq i$ .  $\alpha_i$  is calculated as follows:  $\alpha_i = \sum_k \mathbf{D}(i, k)$ ,  $1 \leq k \leq n_r, k \neq i$ . We then pick the top  $k$  discriminative ROIs with the highest scores.

To evaluate the reproducibility of CBT-based discriminative ROIs, we propose to use an independent learner, namely multiple kernel learning (MKL) [4], which aims to identify the most discriminative features for a target classification task disentangling both  $p^A$  and  $p^B$  groups. Next, we compute the overlap (in %) between the top discriminative ROIs found by the application of (i) the mean absolute difference between the estimated CBTs and (ii) a supervised machine learning method based on MKL. To do so, we independently train a support vector machine (SVM) based on a supervised feature selection method. For each network view  $v$ , we first extract connectional features from each brain network view belonging to the given population by vectorizing the upper triangle of the connectivity matrix. Then, we use a  $k$ -fold randomized partition to divide each population  $p^A$  and  $p^B$  into  $k$  sub-populations. Given the  $v^{th}$  brain view, for each combination of  $p_i^A$  and  $p_i^B$  sub-populations, where  $1 \leq i, j \leq k$ , we train an SVM classifier using the wrapper method MKL to learn a weight score vector quantifying the importance of the features (i.e., brain connectivities) according to their distinctiveness in distinguishing between two sub-populations. Next, we compute the total feature weight vector by summing up the weight vectors for all views and all possible  $\mathbf{A} - \mathbf{B}$  combinations of their  $k$  sub-populations as follows:  $\mathbf{w} = \sum_{v=1}^{n_v} \sum_{i,j=1}^k w_{i,j}^v$ . We linearly anti-vectorize the resulted feature weight vector  $w$  to obtain matrix  $\mathbf{M} \in \mathbb{R}^{n_r \times n_r}$  where each element  $\mathbf{M}(i, j)$  represents the learned weight assigned to brain connections between ROIs  $R_i$  and  $R_j$ . Finally, we sum up the columns of the resulted matrix  $M$  to obtain ROIs discriminability scores where each weight score  $\alpha_i$  quantifies the discriminative power of  $R_i$ , and we pick the top ROIs with the  $k$  highest score. Getting the top  $k$

discriminative ROIs using CBT-based graph fusion methods and MKL-based SVM method, we report the overlap between them where the highest overlap denotes the best method performance in relation with the discriminability of the ROIs.

### **3.3.3.3 CBT node-wise similarity comparison**

Many studies, which investigate the topological features of complex networks [41, 75, 90], consider that graph theoretical metrics are sufficient to preserve the population topology. Among them, we specify graph node-wise metrics which can be estimated at node level of the compared networks. Graph node-wise metrics are calculated for each node, and then the node's metric values are compared across the graphs (CBTs). Such comparison metrics allow not only to explore more features in the graph, but also to indicate where the difference is located between the CBTs (on which brain regions). Globally speaking, these metrics reflect mainly three behaviors in the network: hubness, segregation, and integration.

#### **Hubness behaviour test**

To evaluate the hubness behavior of a graph network, we first include the following measures as they capture different graph topological properties: (i) node strength [14] describes the connection strength (weight) of node to all other nodes, (ii) betweenness centrality [19] is defined as the fraction of all shortest paths in the network that pass through a given node, (iii) random-walk betweenness centrality [15] counts how often a node is traversed by a random walk between two other node, (iv) eigenvector centrality [18] measures a node's importance while giving consideration to the importance of its neighbors, (v) weighted PageRank [12] can be seen as a variant of eigenvector as it investigates the in-degree of nodes and their neighbours by assigning a score to each node based on the number and the weight of edges connected to each node, (vi) Katz centrality [13] can be seen as the generalization of the eigenvector centrality where it computes the relative influence of a node within a network by measuring the number of immediate neighbors (first degree nodes) and also all other nodes in a network that connect to a node under consideration through these immediate neighbors, (vii) information centrality [16] is defined as a variant of closeness centrality based on effective resistance between nodes in a networks. It

## Box 1 Hubness centrality metrics

### Node strength

Node strength ( $S_{v_i}$ ) reflects the importance of the node  $v_i$  in a graph. In the case of weighted networks, we measure  $S_{v_i}$  by summing the weights of edges that connect directly the node with its adjacent neighbors:

$$S_{v_i} = \sum_j^N w_{ij}$$

where  $w$  is the weighted adjacency matrix, in which  $w_{ij}$  is greater than 0 if the node  $v_i$  is connected to node  $v_j$ , and the value represents the weight of the edge.

### Betweenness centrality

Betweenness centrality ( $C_b$ ) considers how important nodes are in connecting other nodes. In other words, it helps identify nodes who play a "bridge spanning" role in a network. In the case of their removal, some nodes becomes unreachable from others.  $C_b$  metric measures the number of the shortest (weighted) paths that passes through a node. The highest the betweenness, the more the node is on all shortest paths from  $s$  to  $t$  nodes in the graph. More formally, the betweenness of node  $v_i$  is defined as the fraction of the shortest paths between all pairs of nodes in the graph (but  $v_i$ ) that go through  $v_i$ :

$$C_b(v_i) = \sum_{s \neq i \neq t} \frac{\sigma_{st}(v_i)}{\sigma_{st}}$$

where  $\sigma_{st}$  is the number of shortest paths from vertex  $t$  to  $s$  and  $\sigma_{st}(v_i)$  is the number of shortest paths from vertex  $t$  to  $s$  that pass through  $v_i$ .

### Random walk centrality

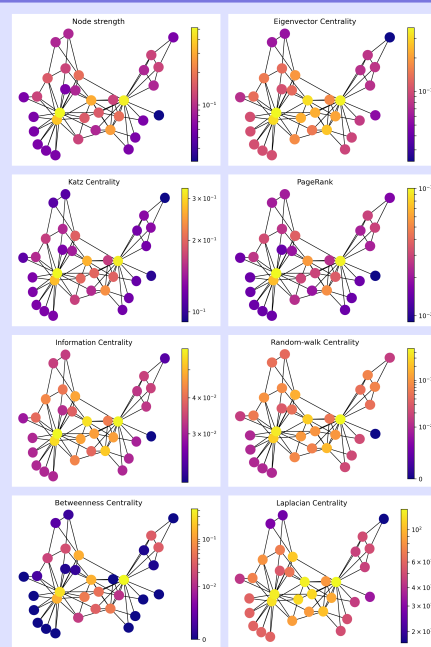
Random Walk is an alternative measure for betweenness counting how often a node is traversed by a random walk between two other nodes. Consider a walk that starts at node  $s$  and make a random moves until it reaches node  $t$ . If at some point in this walk we find ourselves at node  $j$ , then the probability that we will find ourselves at  $i$  on the next step is given by:  $M_{i,j} = \frac{A_{i,j}}{\sum_{i \neq j} A_{i,j}}$ ,  $j \neq t$

### PageRank

PageRank is an adjustment of eigenvector centrality that takes into account the fact that nodes linked to high central node are forced to get high centrality. To overcome that issue, PageRank dilute the link weight received from an important node. Given  $k_{v_i}^{out}$  as the number of outbound links on the node and  $\alpha \in [0,1]$ ,

PageRank is defined as:  $C_{v_i}^t = \alpha \sum_{v_j \in M_i} \frac{C_{v_j}^t}{k_{v_j}^{out}} + \beta$

### Centrality - Example



### Katz centrality

Katz centrality ( $C_{Katz}$ ) measures the relative influence of each node in a given network by taking into account it's immediate neighboring nodes as well as non-immediate neighboring nodes that are connected through immediate neighboring nodes.  $C_{Katz}$  of a node  $v_i$  is computed as:  $C_{Katz}(v_i) = \alpha \sum_j A_{j,i} C_{Katz}(v_j) + \beta$  where  $\alpha$  is a controlling term ( $\alpha < 1/\lambda$ ) and  $\beta$  is a bias term used to avoid the zero centrality value.

### Information centrality

Information centrality relates to both path-length indices and to walk-based eigenmeasures. For that, it counts all possible paths between two nodes weighted by an information-based value for each path that is derived from the inverse of its length. Information centrality is defined by:

$$I_{v_i} = \frac{n}{\sum_{v_j \in V^1} 1/d_{v_i v_j}}, \text{ where } n = \dim[V] \text{ is the number of nodes in the graph.}$$

### Eigenvectors centrality

Eigenvector centrality generalizes node strength by incorporating the importance of the neighbors. When we sum up all connections of a node, not all neighbors are equally important. The node with the highest eigenvector centrality is the one who is connected to more central nodes and if it is connected to only a few unimportant nodes then it won't be important. In practice, it is defined in the following way: the eigenvector centrality  $C_u$  for node  $u$  is when its centrality score equal to a proportional sum of the scores of all nodes which are connected to it.

More formally,  $C_{v_i}^{t+1} = \frac{1}{\lambda} \sum_{v_j \in M_i} C_{v_j}^t$

with a normalization constant  $\lambda$ , where  $M_j$  means that the sum is over all  $j$  such that the nodes  $i, j$  are connected. This recursive definition can be interpreted in term of eigenvectors and eigenvalues, which is defined as  $Ax = x$ , with  $x$  an eigenvector, the corresponding eigenvalue.

### Laplacian centrality

Laplacian centrality ( $C_L$ ) relates the importance of a node to the ability of the network to respond to the deactivation of the vertex from the network. It is an intermediate measuring between global and local characterization of the importance of a node. More formally,  $C_L(G) = \sum_i \lambda_i^2$ , where  $\lambda_i$ 's are eigenvalues of the Laplacian matrix of weighted network  $G$ .

quantifies how easy a node is reached by paths from other nodes, (viii) Laplacian centrality [17] quantifies each node using node strength to assess the impact of their removal from a graph.

Next, we conduct ROI-based comparison using the distribution over the ROIs of the aforementioned centrality measures (CMs) for the connectonal templates (CBTs-based CMs) generated by all graph fusion methods (single-view and multi-graph integration methods). Specifically, each CM distribution is a discrete distribution which is composed of topological measures calculated for each node. For a fair comparison between the CBTs-based CMs, we include CM distribution of the ground truth template (GT-based CM), as a reference for the estimated templates. For each centrality metric, we acquire the ground truth distribution by averaging the distribution of topological measures (i.e., PageRank) of each network view of each testing subject. Additionally, we compute method-based comparison using the Kullback-Liebler divergence measure (KL-divergence). For each centrality measure and for each graph fusion method, we compute KL-divergence between CBT-based CM distribution and GT-based CM distribution over the ROIs. Note that we normalize each distribution using the total sum of measures across all nodes before computing KL-divergence to get a valid discrete probability CM distribution. For the reproducibility of hubness results, for each pair of graph fusion method and CM, we apply 5-fold cross-validation to split the data into training set for CBT generation and testing set to compute CBT-based CM distribution, GT-based CM distribution, and the KL-divergence between them. We report the average centrality metric distributions across folds for the estimated brain template, the average ground truth distributions, and the Kullback-Liebler divergence distribution over folds between the normalized CBT-based CM distribution and the normalized GT-based CM distribution. More formally, KL-divergence measures the difference between two probability distributions  $p(x)$  and  $q(x)$  of a discrete variable  $x$ :

$$D_{KL}(p(x) \parallel q(x)) = \sum_{x=1}^{n_v} p(x) \ln \frac{p(x)}{q(x)}, \quad (3.33)$$

where  $p$  denotes the normalized CBT-based CM distribution,  $q$  is the normalized GT-based CM distribution and  $x$  represents the node of the graph. Finally, we conduct method-to-method comparison between all possible pairs of graph fusion

methods. Specifically, given two fusion methods, we average, for each method, the KL-divergence distribution over folds between the normalized CBT-based CM distribution and the normalized GT-based CM distribution. Then, we compute the KL-divergence between the resulting averages of two methods.

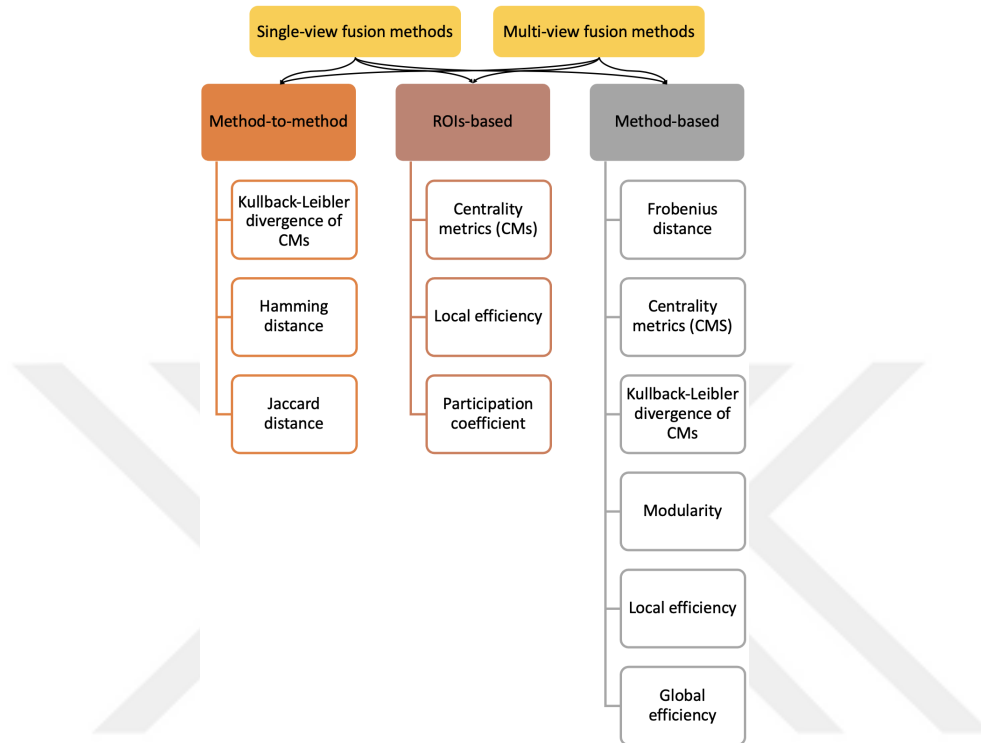


**Figure 3.10 :** Analysis diagram illustrating the types of comparative study to evaluate single-view and multigraph fusion methods. We conduct method-based analysis where we evaluate the CBTs generated by the fusion methods against the ground truth using Frobenius distance, centrality metrics, Kullback-Leibler divergence, modularity, local efficiency, and global efficiency measures. We also conduct ROIs-based analysis to evaluate the CBTs at the node-scale, where we recompute both centrality metrics and local efficiency, and we add the participation coefficient. Lastly, we include method-to-method analysis using a pairwise comparison between graph fusion methods, where we compute three measures: KL-divergence, Hamming distance and Jaccard distance.

### Segregation behaviour test

Another broader criterion for node-wise similarity comparison is the segregation behaviour of graph network, which quantifies the relative difference in strength of within-network versus between-network connections. Among the metrics belonging to this class, we include the local efficiency [91], which measures the efficiency of information transfer limited to neighboring nodes. It is calculated as the average nodal efficiency among the neighboring nodes of node  $i$ , excluding node  $i$  itself. More

formally, the local efficiency is defined as:

$$E_{loc}(i) = \frac{1}{N_{G_i}(N_{G_i} - 1)} \sum_{j \neq h \in G_i} \mathbf{A}_{j,h} \quad (3.34)$$

where  $\mathbf{A}_{j,h}$  is the connectivity weight of the adjacency matrix  $\mathbf{A}$  of graph  $G$  relating node  $j$  with node  $h$ , and  $N_{G_i}$  is the number of neighbour of node  $i$ .

### **Integration behaviour test**

Another direction to measure the similarity between graphs is to evaluate their integration behavior, which reflects the ability of network to combine information from distant nodes. In this context, we include participation coefficient [90], which quantifies the balance between the intramodule versus intermodule connectivity for a given node. In other word, participation coefficient measures the distribution of a node's edges among the communities of a graph. This metric approaches 0 when a node's edges are restricted to its community, and it takes a maximal value that approaches 1 when the node's edges are equally distributed among all communities (high correlations with multiple communities). More formally, the participation coefficient can be defined as:

$$PC_i = 1 - \sum_{s=1}^{N_c} \frac{k_{i,s}}{k_i} \quad (3.35)$$

where  $k_{i,s}$  is the node strength (sum of weights connections) of node  $i$  to other nodes in its own community network ( $s$ ), and  $k_i$  is the degree of node  $i$  regardless of community membership. By subtracting that ratio from 1, participation coefficient is a normalized measure of the connections that are not within a node's own community, or that are across communities.

### **3.3.3.4 CBT graph-edit distances-based comparison**

The main idea of distance-based graph comparison methods consists of comparing two graphs networks by quantifying their similarity. This includes methods based on edit distances that focus to find the common/uncommon nodes (brain regions) and edges (connections) between two brain networks. A special instance of the broader class of graph-edit distances is the Hamming distance. Introduced by [92], the Hamming distance measures the amount of change between two graphs by counting the number of edge deletions and insertions necessary to transform one graph into another. More

formally, the (normalized) Hamming distance is defined as the sum of difference between the adjacency matrices of two graph networks  $G$  and  $\tilde{G}$  on  $N$  nodes:

$$d_H(G, \tilde{G}) = \sum_{i,j=1}^N \frac{|\mathbf{A}_{i,j} - \tilde{\mathbf{A}}_{i,j}|}{N(N-1)} = \frac{1}{N(N-1)} \|\mathbf{A} - \tilde{\mathbf{A}}\|_{1,1} \quad (3.36)$$

where  $i$  and  $j$  are two nodes, and  $A$  and  $\tilde{A}$  are the adjacency matrices of  $G$  and  $\tilde{G}$ , respectively. The Hamming distance value (if normalized) is bounded between 0 (no similarity at all) and 1 (fully similar/same network) over all graphs of size  $N$ . However, the Hamming distance is sensitive to the density of the graphs. This yields a limited capacity to recognize similar level of relative variability across graphs with varying sparsity.

A potential solution to the aforementioned density-effect problem consists in using the Jaccard distance [93], which includes a normalization with respect to the volume of the union graph. This distance metric can be understood as the proportion of edges that have been removed or added with respect to the total number of edges appearing in either graph network. More formally, given two weighted graphs,  $G$  and  $\tilde{G}$ , and two nodes  $i$  and  $j$ , the Jaccard similarity is defined as the difference between the size of the intersection of graph  $G$  and graph  $\tilde{G}$  (i.e. the number of common edges) and the size of the union of graph  $G$  and graph  $\tilde{G}$  (i.e. the number of unique edges) over the size of the union of graph  $G$  and graph  $\tilde{G}$ :

$$d_{Jaccard}(G, \tilde{G}) = \frac{|G \cap \tilde{G}| |G \cup \tilde{G}|}{|G \cup \tilde{G}|} \quad (3.37)$$

In the case of weighted graphs,  $G$  and  $\tilde{G}$  can be represented by their corresponding adjacency matrices  $\mathbf{A}$  and  $\tilde{\mathbf{A}}$ , where  $\mathbf{A}_{i,j}$  and  $\tilde{\mathbf{A}}_{i,j}$  denote the edges weights of graphs  $G$  and  $\tilde{G}$ , respectively, relating node  $i$  with node  $j$ . The Jaccard distance can be written as:

$$d_{Jaccard}(G, \tilde{G}) = 1 - \frac{\sum_{i,j} \min(\mathbf{A}_{i,j}, \tilde{\mathbf{A}}_{i,j})}{\sum_{i,j} \max(\mathbf{A}_{i,j}, \tilde{\mathbf{A}}_{i,j})} \quad (3.38)$$

A Jaccard distance close to 1 indicates an entire remodeling of the graph structure between graph  $G$  and  $\tilde{G}$ .

### 3.3.3.5 CBT global-level similarity comparison

In this part, we aim to evaluate the global structure of the estimated CBTs. One way is to investigate the modular structure of the graph network. A well accepted criterion is modularity  $Q$ , introduced by [94], which evaluates the goodness of partitioning of graph nodes into clusters. In other word, the modularity detects the communities (clusters) in a graph where a node belongs to a community if it has stronger connections with members of this community than with members of another community. Thus, a high modularity means a good clustering where dense connections between nodes are within the same cluster and sparse connections are in different clusters, whereas a low modularity means a poor clustering. More formally, given an adjacency matrix  $\mathbf{A} \in \mathbb{R}^{n_r \times n_r}$  which represents the estimated connectional template (CBT) in our case, the modularity  $Q$  applies to a graph  $G$  and a clustering  $C$  can be written as:

$$Q(C) = \sum_{i,j \in V} \left( \mathbf{A}_{i,j} - \frac{w_i w_j}{w} \right) \delta_C(i, j), \quad (3.39)$$

$$\begin{cases} w_i = \sum_{i \in V} \mathbf{A}_{i,j} \\ w = \sum_{i \in V} w_i = \sum_{i,j \in V} \mathbf{A}_{i,j} \\ \delta_C(i, j) = 1, \text{ if } (i, j) \text{ are in the same cluster under clustering } C \\ \delta_C(i, j) = 0, \text{ otherwise.} \end{cases} \quad (3.40)$$

where  $\mathbf{A}_{i,j}$  denotes the connection weight that relates node  $i$  with node  $j$ . A minimum value of  $Q$  near to 0 indicates that the considered network is close to a random one, whereas a maximum value of  $Q$  near to 1 indicates a strong community structure. The modularity  $Q$  can be written in term of probability distribution:

$$Q(C) = \sum_{i,j \in V} (p(i, j) - p(i)p(j)) \delta_C(i, j). \quad (3.41)$$

Our objective is to cluster nodes while maximizing the modularity which means to decrease the second term of  $Q$ . However this quantity is negligible for too small clusters. To go beyond the resolution limit, the multiplicative factor  $\gamma$ , called the resolution is introduced as follow:

$$Q(C) = \sum_{i,j \in V} (p(i, j) - \gamma p(i)p(j)) \delta_C(i, j). \quad (3.42)$$

For  $\gamma = 0$ , the resolution is minimum and there is a single cluster, that is  $C = \{\{1, \dots, n\}\}$ ;  $\gamma = \infty$ , the resolution is maximum and each node has its own cluster, that is  $C = \{\{1\}, \dots, \{n\}\}$ . To maximize the modularity of our CBTs graphs, we leverage

the hierarchical clustering algorithm, named Pairwise Agglomerative using Resolution Incremental sliding (Paris), which is agglomerative and is based on simple distance between clusters induced by the probability of sampling node pairs. The main idea of this method is to split the nodes of a network into  $K$  non-overlapping communities. Specifically, Paris tries to approximate the optimal partitions with respect to the modularity score and with a sliding resolution. Starting from the maximum resolution where each node has its own cluster, Paris looks for the first value of the resolution parameter  $\gamma$ , say  $\gamma_1$ , that triggers a single merge between two nodes, resulting in clustering  $C_1$ .  $\gamma_1$  can be written as:

$$\gamma_1 = \max_{i,j \in V} \frac{p(i,j)}{p(i)p(j)}. \quad (3.43)$$

Then, the hierarchical clustering algorithm looks for the next value of the resolution parameter, say  $\gamma_2$ , that triggers a single merge between two nodes, resulting in clustering  $C_2$ , and so on. We get in total the sequence of resolutions  $\gamma_1, \dots, \gamma_{n-1}$ . Specifically, the resolution  $\gamma_t$  provides exactly  $n - t$  clusters. Since the best modularity values of the CBTs nodes clustering are reached when the resolution  $\gamma_{n-1}$  provides exactly one cluster, we compute the optimal modularity score  $Q_{n-1}$  of each estimated CBT with corresponding to its resolution  $\gamma_{n-1}$ .

A second method to evaluate the entire structure of the estimated CBTs is to quantify the exchange of information across the whole graph network. A good criterion for this measurement is the global efficiency [91, 95], which is defined as the inverse of the average distance (efficiencies) over all pairs of nodes  $(i, j), i \neq j$  in the whole graph. More formally, the global efficiency is denoted:

$$E_{glob} = \frac{1}{n(n-1)} \sum_{i \neq j} \frac{1}{d(i,j)} \quad (3.44)$$

## 4. RESULTS AND DISCUSSIONS

The structure of the chapter is organized as follows. *Section 4.1* details the results of our experiments generated by our multi-view clustering and fusion network MVCF-Net framework to estimate a well-representative and centered connectional brain template (CBT) for a population of multi-view brain networks. By estimating gender-specific CBTs for male and female cortical morphological networks, respectively, we will identify the top cortical ROIs marking gender differences. We will demonstrate the outperformance of MVCF-Net in comparison with a state-of-the-art method SNF-Clustering-Average (SCA) in terms of (i) centeredness and representativeness compared to all subjects and all views in the population and (ii) discriminability in identifying the most reproducible and discriminative gender connectional markers. By generating a robust and holistic connectional brain map (i.e., CBT) representing a given population, MVCF-Net will reveal gender-specific fingerprints using multi-view cortical morphological in relation to behavior, learning, and cognition. In our future work, we will examine how the identified gender cortical morphological markers relate to brain function and structure using multimodal brain networks.

*Section 4.2* details the results and the discussions chapter, we will detail the results of our experiments generated by our novel graph neural network based multigraph classification framework rooted in (i) multigraph fusion including multiple graph convolutions aiming at learning how to optimally construct the meta-path adjacency matrix across heterogeneous data views and (ii) a classification block comprising consecutive GNN-based node embedding layers to predict the target class label. Our MICNet framework works in an end-to-end manner which helps emphasize the weights of the most relevant edges during the integration step. Based on the experimental results, our MICNet will outperform baseline methods on the two brain genomics superstruct project datasets. In our future work, we aim to generate

augmented multigraphs based on population-level integrated templates to enlarge the dataset and eventually enhance the classification performance. Since our model works on heterogeneous multigraphs, we will evaluate it on an extended dataset covering a diverse range of edge types such as structural and functional connectivities. We also aim to further enhance our framework by designing attention techniques for multigraphs.

*Section 4.3* details the results and the discussions chapter, we will detail the results of the conducted comparison study on the learned brain connectional templates (CBTs) generated by single-view fusion methods and by multigraph fusion methods, separately, by evaluating their performance against the ground truth in term of centerdness, biomarker reproducibility, node-wise similarity, global-level similarity, and distance-based similarity. First, we will estimate single population-based CBTs and multigraph population-based CBTs by integrating a set of single-view biological networks and a set of multigraph biological networks, respectively into a single connectional template. Next, we will compute a set of measurements on the generated CBTs to evaluate their topological properties on the two brain datasets: the Alzheimer’s Disease Neuroimaging Initiative (ADNI) database GO public dataset and the Brain Genomics Superstruct Project (GSP) dataset. Based on the experimental results, we will demonstrat that DGN consistently and significantly outperforms other multigraph integration methods by generating well-centered, discriminative, and topologically sound connectional templates. Together, these criteria will allow DGN to lead the discriminative power in discovering connectional biomarkers that disentangle the connectivity variability of two different populations.

## **4.1 Results and Discussion of Our Proposed MVCF-Net Method**

### **4.1.1 Experimental results**

#### **4.1.1.1 Evaluation dataset and preprocessing pipeline**

We evaluate our proposed MVCF-Net method using the brain genomics superstruct project (GSP) dataset [96, 97] detailed in Table 4.1. The dataset consists of 698

healthy candidates split in two populations: 308 subjects are males and 390 subjects are females, and none of them carry any sign of brain disorders or had any history of mental disease. Each subject is represented with structural T1-w MR image which undergoes preprocessing steps such motion and topology correction, T1-w intensity normalization and segmentation of the subcortical white and deep grey matters volumetric structures [5]. Then, we leverage the reconstruction of the right and the left cortical hemispheres (RH and LH) for each subject [5]. Next, we partition each hemisphere into  $N_r = 35$  cortical regions of interest (ROIs) using Desikan-Killiany Atlas [98] and FreeSurfer [99]. Finally, for each subject  $n$  and for each hemisphere, we define  $M = 4$  networks  $\{\mathbf{V}_n^m\}_{m=1}^M$ , where each is represented by a cortical morphological network (CMN):  $\mathbf{V}_n^1$  indicates the maximum principal curvature brain view,  $\mathbf{V}_n^2$  marks the mean cortical thickness brain view,  $\mathbf{V}_n^3$  is generated using the mean sulcal depth, and  $\mathbf{V}_n^4$  is derived from the mean cortical curvature. Brain morphological networks are constructed separately for the left and the right hemispheres, and they are investigated independently as we aimed in this study to overlook morphological connections that can be “biased” by the brain hemispheric asymmetry [68, 100]. Combining them also prevents the loss of insightful information on how gender affects each hemisphere independently.

**Table 4.1 :** Data distribution of female/male dataset.

datasets	M/F	
	M	F
Number of subjects	615	781
mean $\pm$ std. age	21.6 $\pm$ 0.9	21.6 $\pm$ 0.8

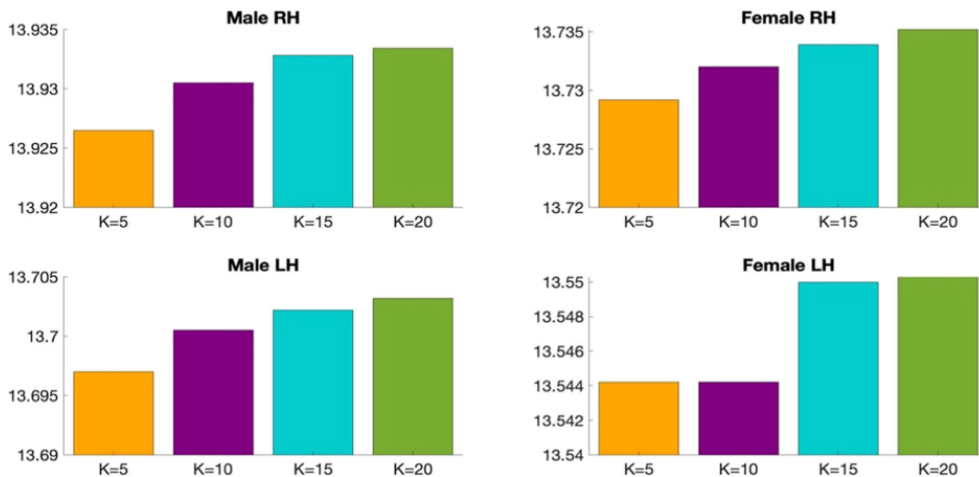
#### 4.1.1.2 Method parameters

We list below the parameters used in our methodology and comparison methods: (1)  $K_n$ : the number of selected neighbors for KNN (2)  $N_c$ : the number of clusters for k-means clustering and (3)  $M$ : the number of views:

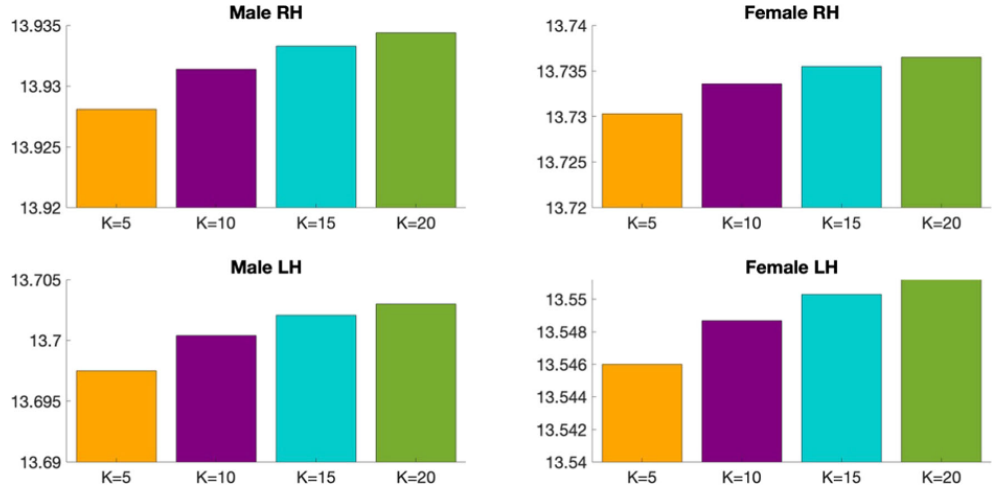
- Number of clusters  $N_c$ . In fact, we use a grid search strategy that considers all parameter combinations by varying the number of clusters  $N_c$  in the range [2,15] in order to determine the best  $N_c$  that achieves the minimum Frobenius distance and the maximum Pearson correlation for the multi-view brain networks across

all methods (ours and SNF-Clustering-Average (SCA)). We found that the optimal number of clusters  $N_c$  is equal to 3 across all methods.

- $K_n$  in KNN algorithm. We also investigate the best number of  $K_n$  nearest neighbors used in KNN method. We vary  $K_n$  in the set (5, 10, 15, 20) and we find that  $K_n = 5$  achieves the minimum Frobenius distance between the estimated templates and all population networks for each method, independently. Figure 4.1 and Figure 4.2 display the average Frobenius distance between the estimated CBT and all CMNs using our method and SCA [9] while varying the number of  $K_n$  nearest neighbors. Noticeably, setting  $K_n = 5$  achieves the best results across all methods. We also use the grid search strategy to identify the best combination of the parameters  $N_c$  and  $K_n$  dependently.
- Number of views  $M$ . We vary the number of selected views to build the subject-specific CMNs from 2 to 4 views. For each selected number of views, we assess all possible combinations of views out of the existing 4 views (e.g., we have  $C_4^2$  possible combinations of  $M = 2$  out of 4 views). We report the average Frobenius distance and the average Pearson correlation between the estimated morphological CBT and all CMN views in the left (LH) and right (RH) hemispheres using our method MVCF-Net in comparison with SCA [9] respectively represented in Figure 4.3 and Figure 4.4.



**Figure 4.1 :** Average Frobenius distance between the estimated CBT by MVCF-Net and all CMNs in the left (LH) and right (RH) hemispheres as we vary the number of selected neighbors for KNN.



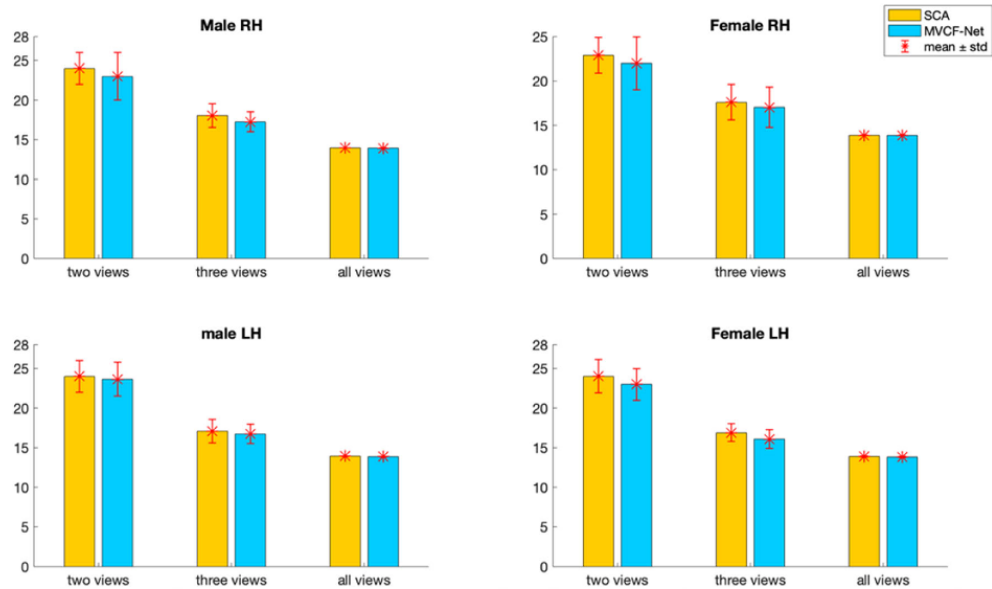
**Figure 4.2 :** Average Frobenius distance between the estimated CBT by SNF-Clustering-Average (SCA) [9] and all CMNs in the left (LH) and right (RH) hemispheres as we vary the number of selected neighbors for KNN.

Figure 4.3 and Figure 4.4 display the average Frobenius distance and the average Pearson correlation between the estimated morphological CBT and all CMNs using our method MVCF-Net in comparison with SNF-Clustering-Average (SCA) [9] as we vary the number of selected views constructing the subject-specific CMNs. For each selected number of views (e.g. 2 views, 3 views, all views), we compute the average of metric (e.g. Frobenius distance, Pearson correlation) using all combination of brain networks. Noticeably, including all views together (e.g. four cortical attributes) achieves the best results for the average Frobenius distance and the average Pearson correlation in the left (LH) and right (RH) hemispheres across all methods (Ours and SCA).

#### 4.1.1.3 Methods comparison

In this work, we propose a robust multiview clustering and fusion network MVCF-Net method for CBT estimation which can simultaneously capture shared and distinct traits of a population lying on different views and identify the top discriminative ROIs marking gender differences. For comparative evaluation, we benchmark MVCF-Net against a state-of-the-art method SNF-Clustering-Average (SCA) introduced in [9].

#### 4.1.1.4 CBT representativeness and centeredness



**Figure 4.3 :** Average Frobenius distance between the estimated morphological CBT and all CMNs in the left (LH) and right (RH) hemispheres using our method MVCF-Net in comparison with SNF-Clustering-Average (SCA) [9] as we vary the number of selected views constructing the CMNs from 2 to 4 views. Each bar represents the average Frobenius distance and its standard deviation of all possible combinations for a given number of views.

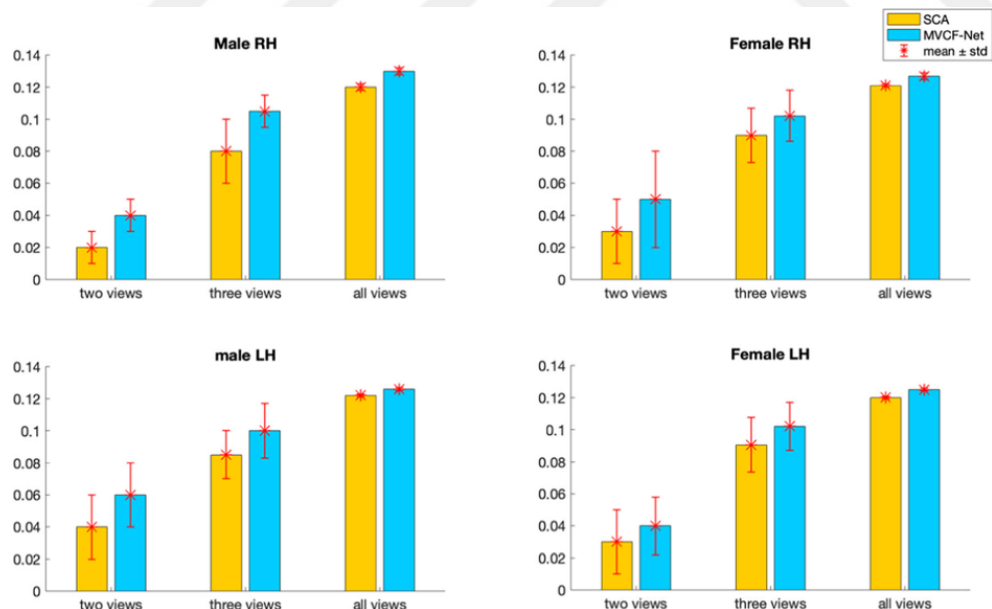


**Figure 4.4 :** Average Pearson correlation between the estimated morphological CBT and all CMNs in the left (LH) and right (RH) hemispheres using our method MVCF-Net in comparison with SNF-Clustering-Average (SCA) [9] as we vary the number of selected views constructing the CMNs from 2 to 4 views. Each bar represents the average Pearson correlation and its standard deviation of all possible combinations for a given number of views.

We evaluate the representativeness of the proposed CBT by computing the mean Frobenius distance and the Pearson correlation between the estimated brain network and all different views (4 views) in each population for SCA as well as for MVCF-Net in left and right hemispheres. To better visualize the difference in performance between MVCF-Net and SCA, we plot the normalized Frobenius distance in Figure 4.5. Also, we randomly partition our data into 5 folds to evaluate the reproducibility of our results across folds as well as when using the whole dataset.

As illustrated in Figure 4.5 and Figure 4.6, our MVCF-Net provides the best centered CBTs for male and female populations in both hemispheres. Based on both evaluation metrics, MVCF-Net method outperforms SCA by achieving the minimum Frobenius distance and the maximum correlation between the estimated CBT and all views for whole and subpopulations (5 folds) in each hemisphere. Excluding one male LH sub-population, MVCF-Net achieves the maximum correlation comparing to SCA. A smaller Frobenius distance indicates a more centered CBT with respect to all individuals in the population and all views. Clearly, MVCF-Net estimates the most centered brain template for each population.

Further, our method stands out in performance in comparison with SNF-Clustering-Average (SCA) as we vary the number of selected views constructing the morphological CMNs from 2 to 4 views. As illustrated in Figure 4.3 and Figure 4.4, our MVCF-Net provides the best centered CBTs for male and female populations by achieving the optimal averages in both Frobenius distance and Pearson correlation between the estimated morphological CBT and all CMNs in the left (LH) and right (RH) hemispheres when the number of views is equal to 2, 3 and 4, respectively. We note that MVCF-Net significantly ( $p - value < 0.001$ ) outperforms SCA comparison method in terms of centeredness across all populations in both hemispheres based on two tailed paired t-test.

#### **4.1.1.5 CBT discriminability**

In addition to being well-centered, we demonstrate that MVCF-Net generates a well-discriminative CBT able to easily spot gender-distinctive brain regions. In

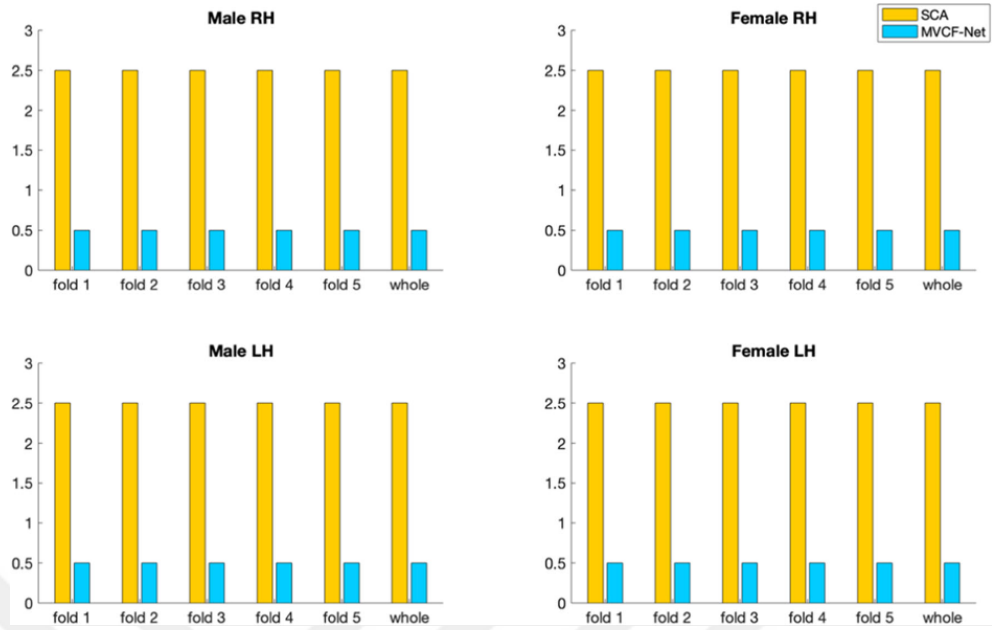
particular, we identify the top 15 discriminative ROIs distinguishing between male and female populations for both hemispheres using the estimated CBTs representing each group. To compare the performance between MVCF-Net and SCA methods, we evaluate the reproducibility of the top 15 discriminative ROIs distinguishing between gender populations in comparison with a feature selection method, namely MKL. Next, we compute the overlap between the most discriminative ROIs identified using our method and those using MKL.

Table 4.2 displays the overlap in % between the top 15 discriminative ROIs identified using (i) MKL and (ii) the absolute difference between the two estimated CBTs by MVCF-Net and SCA, respectively. We demonstrate that our method achieves an overlap percentage of 60% in identifying the most discriminative brain regions in the left hemisphere between genders and 46.67% in the right hemisphere. While SCA method reaches only an overlap percentage of 53.33% and 33.33% in the left hemisphere and the right hemisphere, respectively. Table 4.3 displays the overlap in % between the top 20 discriminative ROIs identified using MKL and the absolute difference between the two estimated CBTs.

**Table 4.2 :** Matching rate in % between the top 15 discriminative ROIs distinguishing between male and female populations identified by (i) MKL and (ii) the difference between the estimated CBTs by SNF-Clustering-Average (SCA) and our method for the right and left hemispheres (RH and LH).

Dataset	Male / Female	
	LH	RH
SCA	53.33%	33.33%
Ours	60%	46.67%

Specifically, our method achieves an overlap percentage of 65% in identifying the most discriminative brain regions in the left hemisphere between genders and 60% in the right hemisphere, while SCA reaches only an overlap rate of 45% for left hemisphere and 55% for the right hemisphere. We notice that the overlap rates between the most discriminative ROIs identified using (i) MKL and MVCF-Net methods as well as using (ii) MKL and SCA methods are higher in the left hemisphere



**Figure 4.5 :** Evaluation of the normalized Frobenius distance between the estimated morphological CBT and all multi-view brain networks for male and female populations in left and right hemispheres (LH and RH) using our method MVCF-Net in comparison with SNF-Clustering-Average (SCA) [9].

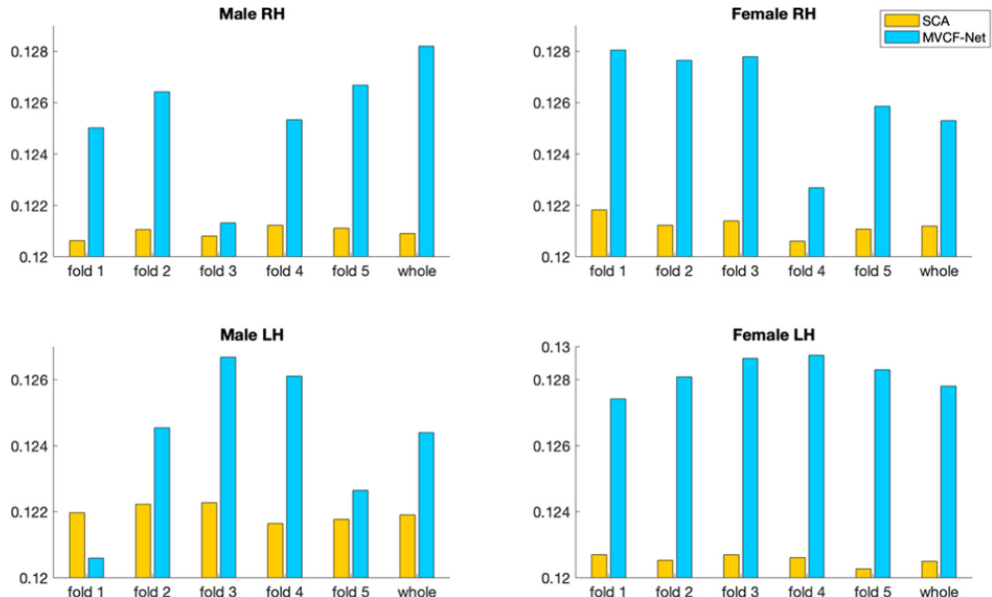


**Figure 4.6 :** Evaluation of Pearson correlation between the estimated morphological CBT and all multi-view brain networks for male and female population in left and right hemispheres (LH and RH) using our method MVCF-Net in comparison with SNF-Clustering-Average (SCA) [9].

compared to the right hemisphere. Our finding supports the evidence that strong gender-related differences are more prevalent in the left hemisphere [101].

In Figure 4.8, we visualize the top 15 discriminative ROIs that distinguish between gender populations for left and right hemispheres using MKL and MVCF-Net, respectively. We plot the discriminability weight of ROIs using the normalized score vector. We note the most two discriminative ROIs selected by MVCF-Net differentiating between male and female populations include the lateral occipital cortex (region 12) followed by the pars opercularis (region 19) for the left hemisphere. These regions are correlated with processing of visuospatial and motion information [102]. For the right hemisphere, the two highly ranked discriminative ROIs identified by our method included the middle temporal gyrus (region 16) and lingual gyrus (region 14) which are correlated with brain size, gray-matter volume and concentration [103, 104].

Figure 4.7 displays the top 5 discriminative ROIs distinguishing between gender populations using MVCF-Net for both RH and LH. These regions are consistent with the literature findings investigating the gender fingerprint, where they were shown to be involved in visuospatial processing, cognitive performance, emotion and facial expression. Precisely, the most discriminative regions selected by our method explain the difference in integration, communication, reaction and memories abilities between human genders [105].

Our discriminative analysis of the estimated CBTs shows the consistency of our proposed method in relation with MKL technique. By detecting gender-specific biomarkers using both comparative methods, we conclude that our proposed MVCF-Net achieves the highest biomarker reproducibility overlap of the top ROIs distinguishing between male and female CMNs (Tables 4.2, 4.3 and Figure 3.1). This demonstrates the effectiveness of our method, first in merging complementary information from one population while computing multi-view clustering using manifolds optimization, in which the aligned clusters preserves simultaneously similar and dissimilar traits of the subjects, second in enhancing the distinctive traits between male and female cortical morphological networks while capturing their fingerprinting

ROIs.

**Table 4.3 :** Matching rate in % between the top 20 discriminative ROIs distinguishing between male and female populations identified by (i) MKL and (ii) the difference between the estimated CBTs by SCA and our method for the right and left hemispheres (RH and LH).

datasets	Male / Female	
	LH	RH
SCA	60%	45%
Ours	65%	55%

### 4.1.2 Discussion

We introduce MVCF-Net, a novel framework for connectional brain template estimation that leverages complementary information offered by multi-view CMNs for a population of multi-view brain networks. Using the estimated CBTs, we identify the top discriminative ROIs distinguishing between genders. First, for each view, MVCF-Net groups similar subjects in the same cluster while separate dissimilar subjects in different clusters. Based on manifold optimization, the clustering process computes the aligned clusters across views to map the subjects to a common space. Then a multi-fusion operation is applied to obtain a representative CBT that captures both shared and differential traits of a population using different views.

#### 4.1.2.1 Parameters impacts

The impact of changing the number of clusters  $N_c$  on the estimated CBT can be explained by the fact that the k-means clustering algorithm is sensitive to the initial positions of the cluster centroids. As we vary the number of clusters, the total within-cluster variation changes result in different CBTs. We note that the generated CBT depends also on the selected number of nearest neighbors  $K_n$ . In KNN algorithm, the computation of both pairwise similarity matrix and the Laplacian matrix depends on the value of  $K_n$ , where a smaller value of  $K_n$  can fail to depict a highly heterogeneous multi-peaked distribution of the population whereas a larger value might over-cluster the data and fail to mimic the real distribution. For the selection of the appropriate number of views (cortical attributes), we demonstrate that

including four cortical morphological networks will provide the best results in terms of CBT centeredness and representiveness. Constructing the CMNs using all views together achieves the optimal average Frobenius distance and the optimal average Pearson correlation in the left (LH) and right (RH) hemispheres across all methods (Ours and SCA). A combination of morphological attributes has been proven to have better diagnostic performance compared with a single attribute [106]. This can be explained by the fact that each type of morphological view is derived from a specific cortical measurement will reveal different changes in the morphology of the brain regions. Thus, the constructed CMNs efficiently handle the complexity of the cortical networks and its multivariate interacting effects between the regions which can greatly help in learning a holistic map of the brain connectivity.

#### **4.1.2.2 CBT representativeness and centeredness**

Our proposed method achieves the best performance in terms of centeredness where the estimated CBTs, derived from male and female populations in both left and right hemispheres, achieve the minimum mean Frobenius distance to all network views (Figure 4.5) as well as the highest Pearson correlation when randomly partitioning the data as well as when using the whole data (Figure 4.6). These results can be explained by the fact that while SCA integrates heterogeneously the network views lying on different manifolds by merging them directly on a global scale, MVCF-Net learns how to align clusters across views to capture both consistent and differential clusters simultaneously. The correlation between the estimated CBT and all network views in each population is globally consistent across both hemispheres, yet the results between the right and the left hemispheres for gender populations show higher correlations for the left hemisphere. This difference can be explained by the fact that both hemispheres present morphological asymmetry [100, 107], which generates different CBTs with different centeredness rates.

	<b>Top 5 discriminative ROIs</b>	<b>Behavioral effect in human gender</b>	<b>ROI representation</b>
<b>Left Hemisphere</b>	Lateral occipital cortex	Face and emotional processing. (Proverbio et al., 2006; Proverbio et al., 2012)	
	Pars opercularis	Speech recovery and re-integration. (Cheng et al., 2009).	
	Postcentral gyrus	Sensory reception, mental rotation and visuospatial processing. (Clower et al. 2001)	
	Unmeasured Corpus Callosum	Interhemispheric connection and communication. (Allen et al., 1991)	
	Caudal anterior-cingulate cortex	Sensory motor reaction and motor reaction. (Naito et al., 2000)	
<b>Right Hemisphere</b>	Middle temporal gyrus	Language and speech processing. (Keller and Menon 2009)	
	Lingual gyrus	Vision processing, logical conditions orders and visual memories encoding. (Clements-Stephens et al., 2009)	
	Superior parietal cortex	Visuospatial processing and cognitive function such manipulation of Information in working memories.	
	Pars triangularis	Semantic processing of language and speech production. (Rubin et al. 2017)	
	Entorhinal cortex	Network for memory in particular spatial memory, navigation and the perception of time. (Nebli et al., 2019).	

**Figure 4.7 :** Top 5 discriminative regions of interest (ROIs) in left (LH) and right (RH) hemispheres distinguishing between gender populations revealed by computing the absolute difference between male and female CBTs by MVCF-Net.

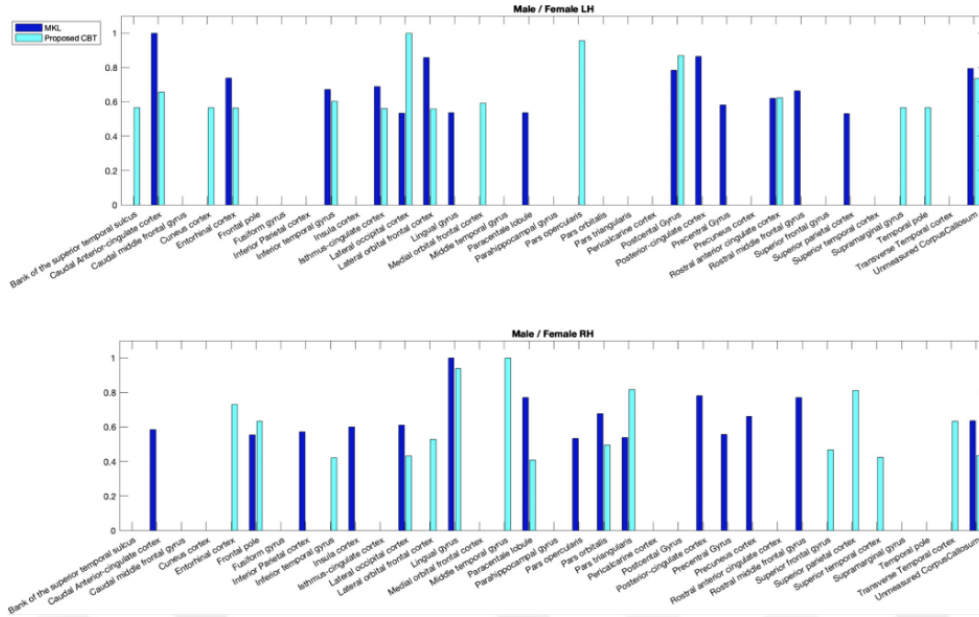


**Figure 4.8 :** *Evaluating the discriminability of the estimated population specific connectional brain template by MVCF-Net.* We identify the top 15 discriminative ROIs using multiple-kernel learning (MKL) and the absolute difference between male and female CBTs in the right and left hemispheres (RH and LH). For each of top identified 15 ROIs, we display their discriminative weight.

#### 4.1.2.3 CBT discriminability

We demonstrate the discriminative potential of MVCF-Net against SCA in distinguishing between gender populations, where MVCF-Net remarkably achieves the highest matching rate with MKL method of the most 15 discriminative ROIs and the most 20 discriminative ROIs as shown in Tables 4.2, 4.3 and Figure 4.7 respectively. These results indicate the effectiveness of our framework in identifying brain regions marking gender differences. This can be explained, first, by the fact that the estimated CBT occupies the minimum distance compared to all subjects in the population, which results in minimizing the inter-subject variability. Second, MVCF-Net is based on multi-view clustering strategy which learns cluster alignment across views to eventually identify both consistent and differential clusters at the same time. Furthermore, MVCF-Net integrates SNF to fuse complementary data lying on different manifolds and avoid dealing with different scales, collection bias and noise in different data types [1]. Therefore, we believe that MVCF-Net produces more holistic CBT representations for male and female populations, stimulating a deeper

understanding of gender difference using multi-view cortical morphological networks.

We display in Figure 4.7 the top 5 discriminative ROIs characterizing the differences between male and female CMNs in the right and left hemispheres. MVCF-Net shows that the top three ROIs distinguishing between genders in the left hemisphere are the lateral occipital cortex, pars opercularis and postcentral gyrus. The lateral occipital cortex is correlated with the control of vision processing specifically facial expression. Our findings are consistent with previous studies, where men showed an asymmetric functioning of visual cortex while decoding faces and expressions, whereas women showed a more bilateral functioning. These results indicate the importance of gender effects in the lateralization of the occipitotemporal response in facial expressions. Other studies supporting our findings, showed a higher activation through a rapid and symmetric of visual time inputs for women rather than men [108, 109]. The reason behind an earlier visual ability is that women have a higher concentration of fibers in the right optic radiation than men [110]. Besides, the pars opercularis region shows an increased volume in young adult females in comparison to males which reflects the high emotional empathic level in women [111]. The third most discriminative region, postcentral gyrus, is involved in multiple aspects of sensory processing and sensorimotor integration [112] especially in the perception of emotions in facial stimuli [113]. The study of [114] supports our discovery of the postcentral gyrus region as a gender biomarker and showed higher regional homogeneity in females than males. This explains why female generally excel in language [115, 116], facial emotion recognition [117] and emotional memory tasks [118].

The fourth most discriminative ROI in LH is the caudal anterior cingulate cortex, which is widely known to be involved in the sensory motor (e.g. motor of reactions) [119]. While the fifth region corpus callosum has been already demonstrated by a large number of studies to show asexual dimorphism. This finding can be explained by the difference in the shape of this region between genders, where it was more bulbous shaped in females and more tubular-shaped in males [120]. Generally, anatomical sex differences such as shape and volume could underlie gender-related differences in

behavior and neuropsychological functions.

For the right hemisphere, our method shows that the most three discriminative regions are the middle temporal gyrus, lingual gyrus and superior parietal gyrus. The middle temporal gyrus reveals the difference in the functional organization of the brain activation between male and female brains, where males show a greater ventral stream activation than females. This explains the high mathematical and spatial cognition performances in males [65]. The lingual gyrus is responsible for visuospatial processing in mental rotation tasks, where the female brain was shown to use spatial attention and working memory, whereas the male brain uses the visuo-motor network [121]. Other morphological differences in the right occipital lingual gyrus and the right middle temporal gyrus were identified by [122], noting that females have significantly increased gray matter concentration rather than male, while males have increased gray matter volume. The third most discriminative ROI, superior parietal gyrus, is correlated with the conscious visual perception of individuals. This focal region showed a difference in brain structure variability between genders which can be explained by gray matter density disparity in the parietal cortex between them.

The fourth most discriminative region in RH is pars triangularis which is important for verbal and language processes. The selection of this region is consistent with [123] study showing the difference of hormone levels in male and female brains responsible for brain system regulation. Compared to women, men showed higher nodal degree and nodal efficiency in pars triangularis. While the entorhinal cortex represents the fifth most discriminative ROI which is consistent with [5] finding that this region is considered as a morphological 'hub' in CMNs derived from four measurements: maximum principal curvature, mean sulcal depth, mean average curvature and mean cortical thickness. Particularly, the entorhinal cortex might explain the difference in gender behavior and why males and females learn differently.

The difference between the top discriminative regions in the right and left hemispheres are mainly due to the asymmetric nature of the human brain [107, 124]. This lack of equivalence comes from the difference in cognitive function for each hemisphere

called hemisphere lateralization. While the right hemisphere is responsible for the visuospatial processing tasks, which is consistent with our finding about the top discriminative regions for the right part of the brain (e.g. middle temporal gyrus region and lingual gyrus), the left hemisphere is used for linguistic processing and communication which is consistent with our top discriminative regions in the left hemisphere related to facial emotional expressions [125]. Our results confirm the fact that the top discriminative regions in the right and left hemispheres are different. In fact, [126, 127] demonstrated in their studies the asymmetric influence of gender on the morphological aspects between both hemispheres where male brains were found to be more asymmetric than female. This gender-related effect is noticeable in all brain areas but is most significant in the superior temporal gyrus.

#### **4.1.2.4 Limitations and future directions**

In our future work, we will examine CBTs generated from multimodal brain networks for a more holistic investigation of gender difference at a morphological, functional and structural levels. This will give new insights into how gender-specific brain morphology relates to brain function and structure. Also, we will use different weights for different views (attributes) according to their importance instead of equal weights. As alternative, we propose simultaneous learning of view specific weights while optimizing the loss function of the multi-view clustering task. This will enable us to identify the most important views in the fusion process and estimation of the gender-specific population-driven CBT.

In summary, we evaluated MVCF-Net, which has the best results in terms of CBT centeredness and representiveness, on morphological connectomic data. Although promising, our method overlooks the topological properties of brain networks when integrating them into a unified CBT. One can integrate topological measures such as degree centrality or betweenness centrality, quantifying the hubness of brain regions in a network, to perverse the population topological properties when estimating the target CBT. We will also tap into the nascent field of graph neural networks (GNNs), which will enable us in an end-to-end manner to learn a CBT without resorting to

craftsmanship of an independent data processing steps. We note that our proposed framework is generalizable to different network neuroscience modalities such as functional and structural connectivities, independently.

## 4.2 Results and Discussion of Our Proposed MICNet Method

### 4.2.1 Experimental results

#### 4.2.1.1 Evaluation dataset and preprocessing pipeline

We evaluate our proposed MICNet method on two brain genomics superstruct project (GSP) multigraph datasets extracted from structural T1-w MR images [97]: one representing multigraphs of the right hemisphere (RH) and the left hemisphere (LH), respectively. Both RH and LH multigraph datasets contain 699 subjects. All subjects are represented by multi-view fully connected graphs of healthy brain connectomes. RH and LH datasets contain 391 female subjects and 308 male subjects. Each brain is represented by a set of  $n_v = 4$  networks, called cortical morphological networks (CMNs) constructed from structural T1-w MRI.

Specifically, we first divide each hemisphere into  $n = 35$  cortical regions of interest (ROIs) representing the nodes of the graphs using Desikan-Killiany Atlas [128]. Next, we produce for each subject a multigraph composed of 4 CMNs, each encoding the dissimilarity in morphology between different cortical regions of interest quantified using a specific cortical measurement. Consequently, each subject is represented by a multigraph where each edge attribute is derived from a particular cortical measurement (e.g., cortical thickness).

Hence, we represent the subject's  $i^{th}$  CMN as an adjacency matrix  $\mathbf{A}_i$  where  $i \in \{1, \dots, n_v\}$ . Particularly,  $\mathbf{A}_1$  indicates the maximum principal curvature brain view,  $\mathbf{A}_2$  denotes the mean cortical thickness brain view,  $\mathbf{A}_3$  is generated using the mean sulcal depth, and  $\mathbf{A}_4$  is derived from the mean cortical curvature. Thus, each edge in

**Table 4.4 : Data description of female/male distributions**

Dataset	Male	Female
Number of subjects	308	391
mean $\pm$ std. age	21.6 $\pm$ 0.9	21.6 $\pm$ 0.8

the graph has  $n_v$  attributes that correspond to connectivity weights for different cortical measures. For each subject, we initialize the feature matrix as an identity matrix.

#### 4.2.1.2 Method parameters

To evaluate the reproducibility of our model as well as benchmark methods, we ran 5-fold cross validation (4 folds for training and 1 fold for testing). For each dataset, we choose the thresholding method based on the results in Fig 4.9. For RH data, We set  $n_g = 1, h = 150, o = 550, a = 0.1$  and  $n_p = 1$  where  $n_g, h, o, a$  and  $n_p = 1$  are the number of graph integration layers, the hidden dimension, the output dimension, the assignment ratio and the pooling layers number, respectively. For LH data, We set  $n_g = 1, h = 128, o = 512, a = 0.3$  and  $n_p = 2$ . All models were trained for 50 epochs.

#### 4.2.1.3 Methods comparison

In this work, we proposed a robust multigraph integration and classification model. To generate the subject-level integrated templates, we benchmarked MICNet against five multigraph integration methods:

**Linear fusion** We add a linear neural layer that has  $n_v$  learned weights. We train this layer over the views of the multigraphs. It assigns an optimized weight for each view to perform a weighted average of the original multigraph. Thus, this step learns to generate a single-view representation (i.e., single graph) of the input multigraph tensor.

**Integration by average** We compute the simple average of the connectivities over all the views.  $a'_{ij} = \frac{1}{n_v} \sum_{k=1}^{n_v} (a_{ij})_k$  where  $\mathbf{A}' = (a'_{ij})$  is the resulting single-view graph.

**SNF** [1] performs a non-linear fusion of the multigraphs across views based on the similarities between nodes. Next, it fuses the multigraph through successive fusion

iterations. The final output is a single view graph with the same nodes of the original graph.

**netNorm** [2] performs a fusion process based on population-based feature selection. This method constructs a fused matrix based on a commonality criterion of feature vectors. The final output of this method is a single-view graph with the same number of nodes as the original multigraph.

#### **4.2.1.4 Classification performance**

Table 4.5 displays the classification results in terms of accuracy, specificity and sensitivity of the different combinations of the five integration methods and the two classifiers detailed in the previous sections. For each dataset, we evaluate 10 models constructed from the 10 possible combinations of the integration methods and classifiers. Based on the accuracy, our MICNet outperforms all benchmark methods by achieving the highest accuracy rate for subpopulations (5 folds) for both hemisphere datasets (RH and LH). On the other hand, if we replace the classifier with GCN and combine it with our integration, the resulting model outperforms all the other GCN-based models. Besides, the models based on our classification block outperform all the GCN-based models except one case when combined with netNorm [2] integration method. We can see that if we change the classifier and consider the multigraph integrator combined with baseline GCN outperforms all GCN-based solutions. This demonstrates the superiority of our GDL-based integration step over other integration techniques. We can explain this by the fact that our learning based integration was able to generate a better subject-specific graph template that contributes in boosting the classification accuracy.

#### **4.2.2 Discussion**

In this section, we introduced MICNet, a novel deep learning based architecture for multigraph classification that integrates a multigraph into a single-view graph prior to classification to leverage the complementary information offered by its different edge types and weights. Our multigraph integration ensures the generation of a representative subject-level single-view graph which enables us to preserve the multigraph topological properties. The geometric deep learning based classifier

**Table 4.5 :** Comparing the classification performance metrics by our proposed method (MICNet) and benchmark methods for gender classification. Our model MICNet is represented by our integration and our classifier (DIFF). The benchmark methods used for comparison include different integration techniques and classifiers. The integration methods are: similarity network fusion technique (SNF) [1], normalization method (netNorm) [2], simple average (average), weighted linear average (linear) and our integration. The classifiers are graph convolutional networks (GCN) [3] and the classification block (DIFF) that we integrated in our model. All models include thresholding as mentioned in the above sections.

RH		Accuracy	Sensitivity	Specificity
SNF [1]	GCN	0.62 ±0.03	0.74	0.48
	DIFF	0.63 ±0.02	0.75	0.5
netNorm [2]	GCN	0.65 ±0.05	0.77	0.51
	DIFF	0.6 ±0.03	0.72	0.46
Average	GCN	0.67 ±0.02	<b>0.78</b>	0.54
	DIFF	0.67 ±0.03	0.78	<b>0.53</b>
Linear	GCN	0.49 ±0.03	0.5	0.47
	DIFF	0.68 ±0.04	<b>0.85</b>	0.49
Our integration	GCN	<b>0.68 ±0.02</b>	<b>0.78</b>	<b>0.55</b>
	DIFF	<b>0.7 ±0.03</b>	0.83	0.52
LH		Accuracy	Sensitivity	Specificity
SNF [1]	GCN	0.48 ±0.06	0.4	0.6
	DIFF	0.56 ±0.02	1	0
netNorm [2]	GCN	0.64 ±0.04	<b>0.78</b>	0.47
	DIFF	0.6 ±0.02	<b>0.69</b>	0.49
Average	GCN	0.66 ±0.03	0.72	0.59
	DIFF	0.69 ±0.06	0.68	0.71
Linear	GCN	0.51 ±0.06	0.57	0.45
	DIFF	0.69 ±0.04	<b>0.69</b>	0.7
Our integration	GCN	<b>0.68 ±0.04</b>	0.68	<b>0.67</b>
	DIFF	<b>0.71 ±0.02</b>	<b>0.69</b>	<b>0.73</b>

captures the most discriminative traits of the graph to predict the subject class. Our MICNet implementation allows end-to-end gradient-based training with original graphs, without the need to first transform graphs into vectors. This section covers interpretations of quantitative and qualitative results.

#### 4.2.2.1 Quantitative analysis

Our model achieved higher classification accuracy without the need for any data normalization. This demonstrates that our model is good at capturing relevant features

with dataset showing lower integrity relation within it. In Fig 4.9, we compared the performance of our model with and without normalization. The normalization that we used is min-max normalization.

In addition, we tested different types of filters between integration and classification blocks. Figure 4.9 displays the impact of the choice of the filter on the classification results. We applied three types of filters: mean, median and without thresholding. Figure 4.9 shows that thresholding had an important effect in boosting the model performance. This can be explained by the fact that thresholding motivates the model to focus on the connectivities emphasized by the integration block.

#### 4.2.2.2 Qualitative analysis

Here, we analyze some clinical insights extracted from the model at different levels during the learning process. The clinical insights include the important features of both connectivities and regions of interest.

**Insights into the most representative cortical morphological connections** By integrating the complementary information of multigraphs over the views for each subject in the population, our MICNet generated a representative and homogeneous subject-level single-view representation. To visualize the most representative morphological connectivities, we conducted a linear average of the integrated graphs across all subjects. Next, we identified the top 5 weighted brain connectivities of the population encoding gender specificity. These selected connectivities represent the most representative edges learned after the integration process. Both gender populations in the left (LH) and the right hemispheres (RH) share the same top 5 representative morphological connections between the brain regions except one different connection for the male population in the RH dataset.

Figure 4.10 display the average single-view learned representations across all subjects and the top 5 most representative morphological connectivities of both gender populations for RH and LH, respectively. As shown in the figure, female circular graph in LH, male circular graph in LH and female circular graph in RH showed the

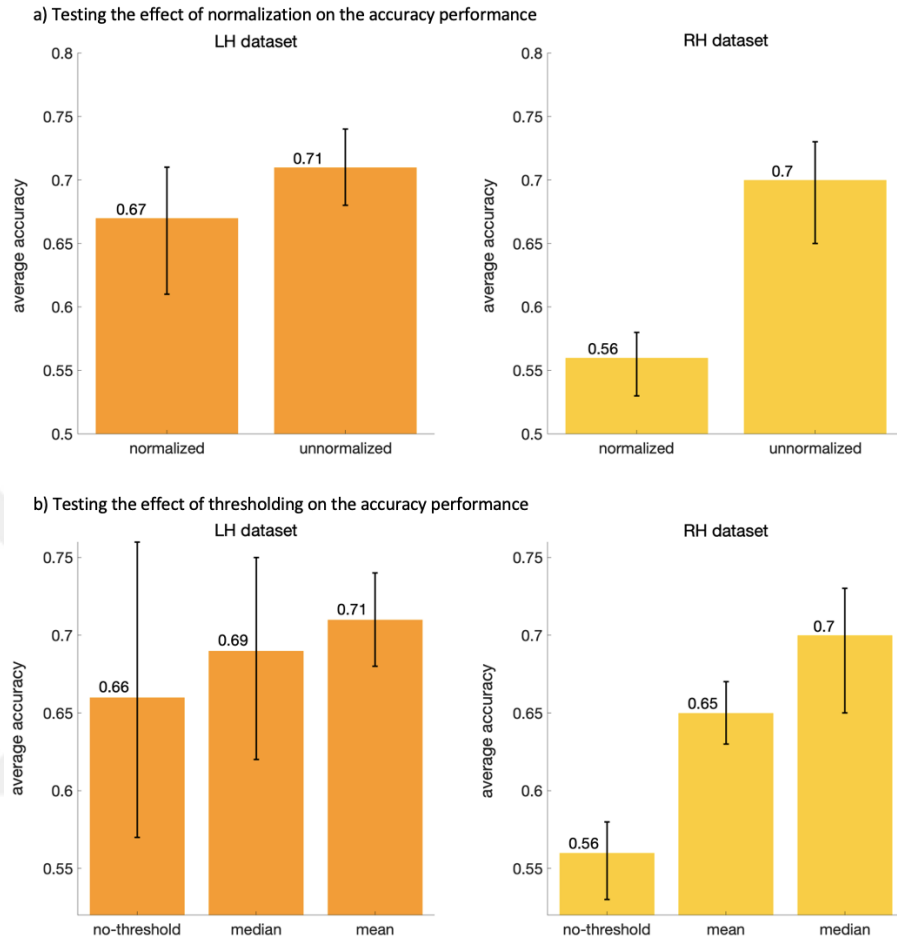


**Figure 4.9 :** a) *Testing the effect of normalization on the accuracy performance using 5 folds cross-validation.* b) *Testing the effect of thresholding on the accuracy performance using 5 fold cross-validation.* For a) and b), the left and right barplots display the accuracy obtained using left and right hemisphere datasets, respectively. In each plot of a), the left bar shows the result obtained by our model after normalization of the data using min-max technique. The right bar shows the results obtained by our model without data normalization. In each plot of b), the bars correspond to three types of filters: mean thresholding, median thresholding and without thresholding. The thresholding step was applied between integration and classification blocks of our model. These barplots point out the contribution of the different thresholding strategies to the global model accuracy for both datasets (left and right hemispheres).

same top 5 connections between ROIs. The first most representative connection was identified between the bank of the superior temporal sulcus and the supramarginal gyrus. Moreover, the connection linking the bank of the superior temporal sulcus and the temporal pole was scored as the second most representative edge. The third most representative morphological connection was identified between the cuneus cortex and the supramarginal gyrus. The connection between the cuneus cortex and temporal pole had the fourth rank. The fifth most representative cortical morphological connection was established between the supramarginal gyrus and the temporal pole.

Supporting our findings, [129] reported that the cuneus cortex region had been shown to be involved in a neural network functionally specialized in the processing of spatially guided behavior. [130] studied the abnormalities in neonates associated with genetic risk for schizophrenia. It was reported that male with high-risk neonates had significantly thicker cortex in the left cuneus cortex while female with high-risk neonates had significantly thinner cortex in the right cuneus.

[131] found that females have higher regional homogeneity in supramarginal gyrus than males during the resting-state and spontaneous brain activity within cerebral cortex. [130] demonstrated that the supramarginal gyrus volume is significantly larger in male subjects when compared to females. Moreover, male showed a leftward (left > right) asymmetry for the supramarginal gyrus, with a less marked opposite asymmetry in females. Such sexual dimorphisms may possibly underlie the subtle cognitive differences observed between both genders.

[130] studied the influence of gender on the morphology of temporal pole structures in patients with schizophrenia. They found that temporal lobe volume on the left is significantly smaller in male patients than in female comparison subjects. [132] reported evidence that the temporal pole may have a lower synaptic density in women than in men, which could differentially influence the efficiency with which certain cognitive operations are performed.

[133] reported that the bank superior temporal sulcus was associated with action control in the context of reward processing. Other studies [132] found that the superior temporal sulcus region was implicated in the representation of perceived pleasantness and positive affection. [134] provided evidence that men exhibited a stronger reduction of activation in this region during the ‘desire-reason dilemma’. This finding supports the view of a sexual dimorphism that manifested in the recruitment of gender-specific neural resources during the successful deployment of self-control [134].

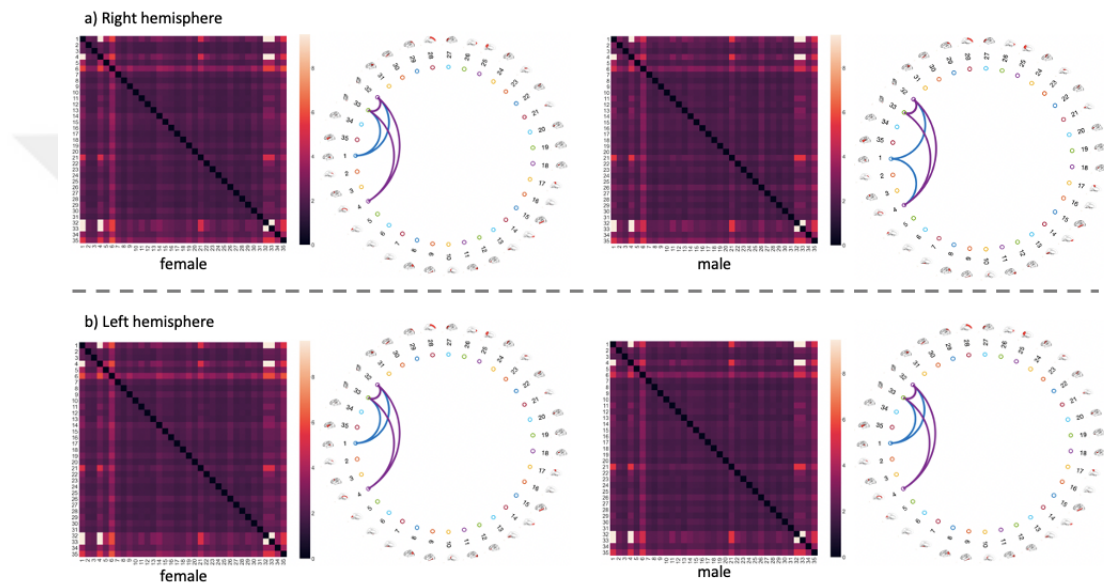


**Figure 4.10 :** *a) Average connectivity matrices across all the subjects of each class after multigraph integration with the respective top 5 connectivity weights using MICNet on left hemisphere dataset. b) Average connectivity matrices across all the subjects of each class after multigraph integration with the respective top 5 connectivity weights using MICNet on right hemisphere dataset. For a) and b), the two figures at the left and the two figures at the right correspond to the male and female class subjects, respectively. Each heatmap is obtained by computing the average of each connectivity of all subjects for a specific class after integration block. The heatmaps reflect the distributions of the assigned weights by the multigraph integration step. Circular graphs display the most important connectivities for each class based on the edge weights after integration.*

**Insights into the most representative cortical morphological regions** To identify brain regions marking gender differences, we extracted the weights characterizing the importance of brain regions to differentiate between male and female CMNs in the right and left hemispheres. Fig 4.11 displays the learned weights for the first

graph convolution layer after integration. These weights have more contribution in the pooling process of the classification block. Hence, they have the major contribution in the classification decision. Based on the results in Fig 4.11, MICNet showed that the top two discriminative ROIs distinguishing between genders in the left hemisphere are the precentral gyrus and rostral middle frontal.

The precentral gyrus is correlated with the control of the voluntary movements. As a sub-region of the frontal lobe, this sensory-motor region is responsible on the spontaneous activity of the body such as hand and face areas. Our findings are consistent with previous studies of [135], where men showed a volumetric increase in the white matter of the left precentral gyrus region due the biological changes of hormones in puberty . In females, however, there were no significant volumetric changes with age. Other studies [129] supporting our findings, showed that the maturation of white matter in the left pre-central gyrus in men may underlie the differences in semantic verbal ability. As a language sub-region, the left precentral gyrus may contribute to the increase in learning disabilities that are more seen in males than females. For example, boys are four times more likely than girls to stutter and language impairments have been found to occur 10 times more often to boys compared to girls [133]. Additionally, [129] reported that girls outperform boys during preschool and early years in articulation, longer sentences use, verbal fluency, and tests of grammar and spelling. In a language phonological task using fMRI, [133]reported that men showed greater activation in the precentral gyrus, whereas women showed more bilateral activation.

The second most discriminative region is the rostral middle frontal gyrus, which is widely known to be involved in the mental rotation task. The study of [131] supported our discovery of this region as a gender biomarker and showed that the networks involved in visual attention appear to be more strongly activated in the mental rotation tasks in men as compared to women. These findings suggested that men and women use similar neural pathways to analyze and solve the mental rotation task. In fact, male use a more automatic process when analyzing complex visual reasoning tasks while female use a more top-down process (frontal lobe functioning). Another study [136]

showed that men have an increased activation in areas that have been implicated for visual analysis (rostral middle frontal gyri, and middle occipital gyrus) compared to women while designing a cubic figure.

For the right hemisphere, our method showed that the top two discriminative regions are the superior parietal cortex and the pericalcarine cortex. The superior parietal cortex (SPC), is correlated with the conscious visual perception of individuals [135]. This focal region shows a difference in brain structure variability between genders which can be explained by gray matter density disparity in the parietal cortex between them. Other studies supported our findings, showing that SPC plays a key role in cognitive processes, in particular somatosensory and visuo-motor integration as well as visuo-spatial attention and memory [137]. The increase of the parietal gray and white matter in men compared to women is associated with bilateral superior parietal activations, leading to higher performance in visuo-spatial tasks for male [135]. Rightward lateralization had been described for intentional processes, movement planning, and visuo-motor transformations [137].

On the other hand, the second most discriminative brain regions (nodes), pericalcarine cortex, belongs to the primary sensory cortex which plays an important role in visual information [138]. Our findings were supported by [138], reporting that the pericalcarine cortex is associated with task-focused activity which requires both visuo-spatial perception and motor coordination. In particular, such tasks require a tight link between the spatial-temporal constraints and one's own bodily movement control. [136] demonstrated that the pericalcarine is a particularly strong source of visual gamma-band activity reporting that gamma peak frequency is higher in female than male subjects.

#### **4.2.2.3 Limitation and future directions**

Although our model outperformed baseline methods in the target brain multigraph classification task, it has a few limitations that could be overcome in future work. *First*, the metapaths generated during the integration can be of a suboptimized length. Alternatively, we can implement self-attention layers inspired by [139]

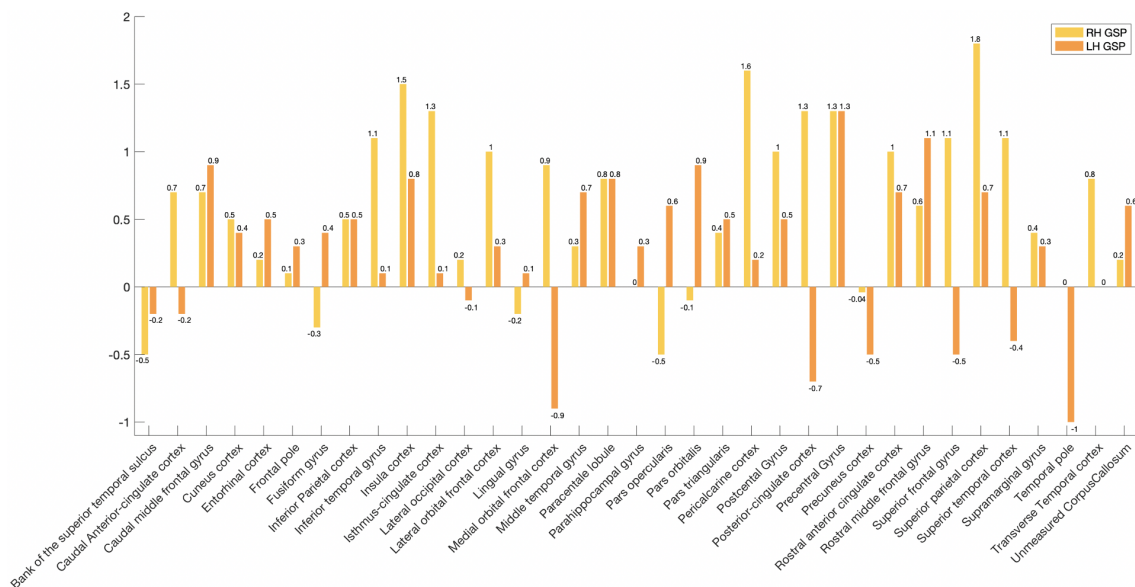


**Figure 4.11 :** Region-wise distribution of the learned discriminative weights in MICNet for both datasets (right hemisphere and left hemisphere). We extracted these weights from the first graph convolution layer of the classification block. These learned weights are obtained by the end-to-end learning process to deliver accurate prediction of classes. These weights reflect the most discriminative brain regions distinguishing between male and female classes.

and adapt it to our framework to help capture the most relevant combinations of edge weights of different lengths. *Second*, considering the high dimensionality of the brain connectomes, our evaluation dataset is considered relatively small. Alternatively, we intend to exploit the potential of data augmentation techniques and adapt it to the multigraph domain to sustain our model in terms of reproducibility and generalizability. *Finally*, despite the heterogeneity of the evaluation dataset, it contained only morphological connectivities. It would be more challenging if we add connectivity edges derived from other modalities such as structural connectivities [131] or functional connectivities [46] which will in turn increase the multigraph heterogeneity.

In summary, We introduce Multigraph Integration and Classifier Network (MICNet), the first end-to-end graph neural network based model for multigraph classification. First, we learn a single-view graph representation of a heterogeneous multigraph using a GNN based integration model. The integration process in our model helps tease apart the heterogeneity across the different views of the multigraph by generating

a subject-specific graph template while preserving its geometrical and topological properties. Second, we classify each integrated template using a geometric deep learning block which enables us to grasp the salient graph features. We train, in end-to-end fashion, these two blocks using a single objective function to optimize the classification performance. We evaluate our MICNet in gender classification using brain multigraphs derived from different cortical measures. We demonstrate that our MICNet significantly outperformed its variants thereby showing its great potential in multigraph classification.

### **4.3 Results and Discussion of Our Comparative Study of Connectional Brain Templates in Network Neuroscience**

#### **4.3.1 Experimental results**

##### **4.3.1.1 Evaluation datasets**

We conduct our comparison study between the graph fusion methods, which is based on the aforementioned CBT evaluation measures, using two datasets: the first datasets (M/F dataset) consists of 308 male subjects (M) and 391 female subjects (F) from the Brain Genomics Superstruct Project (GSP) dataset [97], aged between 21 and 23 years old; males ( $n = 308$ ;  $21.6 \pm 0.9$  years, mean  $\pm$  s.d.); females ( $n = 390$ ,  $21.6 \pm 0.8$  years, mean  $\pm$  s.d.). The second dataset (AD/LCMI dataset) is collected from the Alzheimer’s Disease Neuroimaging Initiative (ADNI) database GO public dataset [140] and includes 67 subjects (35 diagnosed with Alzheimer’s diseases (AD) and 32 with Late Mild Cognitive Impairment (LMCI)). For both datasets, each subject is represented by 4 cortical morphological brain graphs derived from maximum principal curvature, mean cortical thickness, mean sulcal depth, and average curvature measurements. For each hemisphere, cortical surface is reconstructed from T1-weighted MRI using FreeSurfer pipeline and parcellated into 35 cortical regions of interest (ROIs) using Desikan-Killiany cortical atlas [141]. The corresponding connectivity strength between two ROIs is derived by computing the pairwise of the absolute difference of their average cortical attribute as introduced in [29] (Table 4.6).

**Table 4.6 :** Data distribution for M/F and AD/LCMI datasets. Each view in the connectomic datasets contains 35 nodes, and 4 views are fully connected.

datasets	M/F		AD/LCMI	
	M	F	AD	LMCI
Number of subjects	615	781	70	64
Right hemisphere (RH)	308	391	35	32
Left hemisphere (LH)	308	391	35	32
mean $\pm$ std. age	21.6 $\pm$ 0.9	21.6 $\pm$ 0.8		
number of views	4	4	4	4

### 4.3.1.2 Parameter settings

We set all the hyperparameters for each graph fusion method using a grid search. For SNF [1], we empirically set the number of nearest neighbors to  $K = 20$  and the number of iterations  $N_t = 20$  for convergence. For NAG-FS [7] method, we set the number of cluster to  $N_c = 3$  for multiple kernels learning parameters. We also set the number of iterations to  $N_t = 20$  for SNF parameters. Concerning the number of nearest neighbors for both SNF and multiple kernels learning, we opted for setting them to  $K = 20$  which produce the best performance. For SM-netFusion [8] parameters, we tested it using  $N_c = 3$  clusters given the best result. For the cross-diffusion process parameters, we also set the number of iterations to  $N_t = 20$  for convergence. We fixed the number of closest neighbors  $K = 20$ . For SCA [9] parameters, we set the number of iterations to  $N_t = 20$  as it guarantees SNF convergence [1]. We set the number of nearest neighbors to  $K = 20$  and for the clustering we used  $N_c = 3$  clusters giving the best results. For MVCF-Net [10] parameters, we set the number of clusters to  $N_c = 3$  achieving the best results and the number of nearest neighbors to  $K = 5$  for K-Nearest Neighbor(KNN) algorithm as recommended in [10]. For netNorm [2] parameters, we set the the number of iterations used in SNF to  $N_t = 20$  to guarantee its convergence as recommended in [1]. We also empirically set the number of nearest neighbors to  $K = 20$ . For cMGINet [20] parameters, we set the number of clusters to  $N_c = 3$  and the number of kernels to 5 for the multiple kernel learning. We trained the cMGINet model using 300 epochs with hyperparameters  $\lambda = 0.3$  for scaling the subject-specific integration loss and the number of channels  $n_c = 2$ . For SNF, the number of nearest neighbors is set to  $N_t = 20$ . For DGN [11] parameters, we empirically set the hyperparameters to 3 edge-conditioned convolutional neural network layers with an edge-conditioned

filter learner neural network. These layers are separated by ReLU activation function and output embeddings with 36, 24 and 5 dimensions for each ROI in the multigraph brain networks, respectively. The DGN is trained using gradient descent with Adam optimizer and a learning rate of 0.0005. The number of random samples in the subject normalization loss function is fixed to 10.

### **4.3.1.3 Evaluation strategies**

We evaluate the performance of the single-view fusion methods set including SNF [1], NAG-FS [7], and SM-netFusion [8], and the multigraph fusion methods set including DGN [11], cMGI-Net [20], netNorm [2], MVCF-Net [10], and SCA [9], separately. For CBT generation, we employ as input dataset single-view networks for single-view fusion method and multi-view networks composed of 4 cortical morphological brain graphs for multigraph integration methods. To ensure the reproducibility and the generalizability of our evaluation results, we split each dataset into training and testing subsets using 5-fold cross-validation. We use the training subset to train the aforementioned 8 different models and to generate CBTs for both hemispheres(LH and RH) of 4 populations namely; AD, LMCI, M, and F. Next, we showcase each fusion method with four different evaluation tests on the left out testing subset: (1) centeredness, (2) biomarker discovery of most discriminative connections between two groups, (3) graph global-level similarity to the original dataset, (4) graph node-wise similarity, and (5) graph distance-base similarity.

## **4.3.2 Discussion**

### **4.3.2.1 CBT centeredness test**

We evaluated the centeredness of the estimated CBT by measuring its Frobenius distance to each tensor view of each subject in the population. According to the results in Figure 4.12 and Figure A.1, DGN considerably outperforms all benchmark multigraph fusion methods by achieving the minimum average Frobenius distance for all evaluation datasets (AD/LMCI and M/F datasets), for subpopulations (5-fold) and the mean over the folds in both hemispheres (RH and LH). For single-view fusion methods comparison, SM-netFusion slightly outperforms SNF and NAG-FS by attaining lower Frobenius distance value than the other methods. We note that

DGN and SM-netFusion significantly outperform other methods across all left-out folds and evaluation datasets. (Figure 4.12 and Figure A.1, two-tailed paired t-test, all  $p < 0.0001$ ). These results can be explained by the fact that unlike other single-view and multigraph fusion methods, DGN integrates a randomized weighted loss function which acts as a regularizer to minimize the distance between the population of multi-graph brain networks and the estimated CBT, thereby enforcing its centeredness. DGN also refines the estimated CBT using a post-training process based on the element-wise median of all training CBTs to select the most centered connections for the final CBT generation. Most importantly, it is trained in an end-to-end manner.

#### 4.3.2.2 CBT discriminativeness reproducibility test

In addition to being well-centered, we demonstrated that DGN generates a well-discriminative CBT able to easily spot both gender-distinctive brain regions and AD-LMCI-distinctive brain regions. This can be explained by the fact that DGN captures the most discriminative traits of a population of multigraph networks, acting as a connectional brain biomarkers. Particularly, we first spotted the top  $k$  ( $k = 10, 15, 20, 25$ ) most discriminative brain connectivities distinguishing between two populations (i.e., AD/LMCI) for both hemispheres using the estimated CBTs representing each class. Next, to evaluate the reproducibility of CBT-based discriminative ROIs, we trained a support vector machine (SVM) to learn how to classify two populations coupled with Multiple Kernel Learning (MKL) to learn a weight vector that scores the discriminativeness of each feature (i.e., ROI). Next, we computed the overlap between the most discriminative ROIs identified using inter-class CBT difference and those using MKL.

Table 4.7 displays the overlap in % between the top 10, 15, 20, and 25 discriminative ROIs identified using (i) MKL and (ii) the absolute difference between two estimated CBTs generated by all single-view and multigraph fusion methods, respectively, using both AD/LMCI datasets and M/F connectomic datasets. We demonstrated that DGN method reaches the highest overlap percentage comparing to other multigraph and single-view fusion methods between AD/LMCI datasets by achieving 14-32% and 20-46% boost in biomarker reproducibility against other methods in the left and the



**Figure 4.12 :** Centeredness comparison of connectional templates generated by **A)** single-view integration methods including network atlas-guided feature selection (NAG-FS) [7], similarity network fusion (SNF) [1], and supervised multi-topology network cross-diffusion (SM-netFusion) [8]; and **B)** multi-graph fusion methods including multi-view networks normalizer (netNorm) [2], SNF-Clustering-Average (SCA) [9], multi-view clustering and fusion (MVCF-Net) [10], cluster-based multi-graph integrator networks (cMGI-Net) [20], and deep graph normalizer (DGN) [11]. Charts illustrate the mean Frobenius distance between the connectional templates learned from the training sets and networks of the samples in the testing set using a 5-fold cross-validation strategy. We reported the average distance for each cross-validation fold as well as the average across folds (“Mean” bars on the right). For multi-graph fusion methods comparison, DGN achieved the lowest mean Frobenius distance to the population multi-view networks with a high statistical significance demonstrated by a two-tailed paired t-test (all  $p < 0.0001$ ) for DGN-SCA, DGN-netNorm, DGN-MVCFNet, and DGN-cMGI-Net pairs for AD-LH, AD-RH, LMCI-LH and LMCI-RH groups. LH: left hemisphere. RH: right hemisphere. AD: Alzheimer’s disease. LMCI: Late Mild Cognitive Impairment. As for single-view fusion methods comparison, SM-netFusion significantly achieved the lowest mean Frobenius distance to the population single-view networks (all  $p < 0.0001$ ) using two-tailed paired t-test for SM-netFusion-NAGFS, and SM-netFusion-SNF pairs for AD-LH, AD-RH, LMCI-LH and LMCI-RH datasets.

right hemispheres, respectively. Furthermore, DGN ranked first in reproducibility where it achieves 12-30% and 12-40% boost in identifying the most discriminative brain regions between genders against other methods in the left and right hemispheres, respectively, using M/F datasets (Table 4.7). The displayed results represent respectively the minimum and the maximum differences between the reproducibility rates of DGN and each of the other methods over the top  $k$  (10, 15, 20, and 20) discriminative ROIs distinguishing between AD and LMCI populations, and between male and female populations.

**Table 4.7 :** Matching rate in % between the top  $k$  (10, 15, 20, and 20) discriminative ROIs distinguishing between AD and LMCI populations, and between male and female populations identified by (i) MKL [4] and CBT-based single-view fusion methods and (ii) MKL [4] and CBT-based multigraph fusion methods for the right and left hemispheres (RH and LH).

Top $k$ (%) discriminative ROIs datasets		Matching rate (10 % )				Matching rate (15 % )				Matching rate (20 % )				Matching rate (25 % )			
		AD-LMCI		GSP		AD-LMCI		GSP		AD-LMCI		GSP		AD-LMCI		GSP	
Hemispheres		LH	RH	LH	RH	LH	RH	LH	RH	LH	RH	LH	RH	LH	RH	LH	RH
Single-view fusion methods	SNF [1]	0.3	0.1	0.1	0.1	0.2	0.13	0.33	0.4	0.5	0.5	0.5	0.5	0.68	0.68	0.68	0.64
	<b>SM-netFusion [8]</b>	<b>0.5</b>	<b>0.5</b>	<b>0.1</b>	<b>0.1</b>	<b>0.47</b>	<b>0.53</b>	<b>0.33</b>	<b>0.46</b>	<b>0.55</b>	<b>0.55</b>	<b>0.55</b>	<b>0.55</b>	<b>0.72</b>	<b>0.72</b>	<b>0.72</b>	<b>0.72</b>
	NAG-FS [7]	0.2	0.2	0	0.2	0.27	0.27	0.27	0.33	0.5	0.5	0.46	0.5	0.68	0.68	0.64	0.64
Multigraph fusion methods	SCA [9]	0.3	0.3	0.2	0.4	0.4	0.53	0.27	0.33	0.45	0.65	0.4	0.5	0.64	0.68	0.68	0.68
	MVCF-Net [10]	0.46	0.46	0.2	0.4	0.47	0.53	0.27	0.33	0.45	0.55	0.4	0.5	0.64	0.68	0.68	0.68
	netNorm [2]	0.3	0.4	0.2	0.4	0.4	0.53	0.33	0.4	0.55	0.6	0.5	0.5	0.72	0.64	0.7	0.64
methods	cMGINet [20]	0.2	0.4	0	0.1	0.4	0.47	0.27	0.33	0.55	0.65	0.4	0.45	0.72	0.72	0.64	0.68
	<b>DGN [11]</b>	<b>0.5</b>	<b>0.5</b>	<b>0.3</b>	<b>0.5</b>	<b>0.53</b>	<b>0.6</b>	<b>0.53</b>	<b>0.53</b>	<b>0.6</b>	<b>0.7</b>	<b>0.6</b>	<b>0.6</b>	<b>0.76</b>	<b>0.84</b>	<b>0.76</b>	<b>0.76</b>

### 4.3.2.3 CBT node-wise similarity comparison

#### *Hubness behaviour test*

Furthermore, we compared the performance of the graph fusion methods by evaluating the similarity of their generated brain templates at the node-wise scale. One way to do so is to quantify the topological properties of the CBTs using the following centrality measures: node strength, betweenness centrality, random-walk betweenness centrality, eigenvector centrality, weighted PageRank, Katz centrality, information centrality, and Laplacian centrality. Specifically, we evaluated the topological properties of the learned CBTs by comparing the likelihood of distribution of the aforementioned topological measures between the ground truth of multigraph brain population and the learned CBTs. We calculated the ground truth by averaging the distribution of topological measures of each network view of each testing subject. We display the average across five folds for each centrality metric in the form of distribution graphs for AD (LH), LMCI (LH), AD (RH), and LMCI (RH) populations (Figure

4.13) and for M (LH), F (LH), M (RH), and F (LH) populations (Figure A.2). As shown in Figure 4.13 and Figure A.2, the connectional brain template generated by DGN shows a striking similarity with the ground truth data in topological properties while other multigraph integration methods and all single-view fusion methods fail to preserve the multi-view and single-view connectomic data topology, respectively. This can be explained by the fact that DGN has the ability to capture much more complex topological patterns rather than the other fusion architectures. Specifically, DGN trains a GDL-based learning process for brain connection weights by blending a sequence of hidden nodes embeddings with the integrated connectivities while capturing complex patterns and non-linear variation across individuals. For easy interpretation and better visualization of the results, we computed the average of each centrality measure distribution across the ROIs, so that each distribution is represented by a single value. The results in Figure 4.14 (for AD/LMCI dataset) and Figure A.3 (for M/F dataset) confirm that DGN is the most topology preserving method in a population of multiview networks by closely nearing the average distribution of the ground truth multi-view brain networks. While SM-netFusion achieved the highest average distribution comparing to other single-view fusion methods.

Second, we extended the hubness comparison between the CBTs by integrating the Kullback-Liebler (KL) divergence metric which measures the dissimilarity between two given graphs by quantifying the information change between them. The main idea was to compute for each centrality metric the KL-divergence of (i) the ground truth distribution and (ii) each of the distributions derived from the connectional brain templates, learned within a 5-fold cross-validation strategy. Note that we normalized each distribution using the sum over all nodes to get a valid discrete probability distribution. Next, we reported the KL-divergence distribution resulting from all possible pair combinations of sub-populations (folds). We evaluated the performance of the graph fusion methods based on the lowest value of the average KL-divergence distribution and its standard deviation over all combinations of 5 sub-populations. A small divergence signifies similar distributions. Comparing to other multigraph fusion methods Figure 4.15 and Figure A.4 section B showed that DGN significantly outperforms other multigraph fusion methods on both evaluation datasets using the

left and right hemispheres and across all topological measures (two-tailed paired t-test  $p < 0.0001$ ) by achieving the minimum scores in both mean KL-divergence distribution and its dispersion for AD, LMCI, M, and F datasets. We demonstrated that DGN generates the most similar centrality measure distribution to the ground truth by preserving the complex patterns in a population of multi-view networks during the data integration process to generate more holistic and integral connectional templates. For the single-view fusion methods comparison, Figure 4.15 and Figure A.4 section A showed that SM-netFusion outperforms SNF and NAG-FS by achieving the minimum mean KL-divergence distribution in AD/LMCI dataset and M/F dataset, respectively, for both hemispheres.

Lastly, we compute a pairwise comparison between all combinations of the single-view and multigraph fusion methods, separately, using KL divergence. Specifically, for each topological measure, we computed the KL-divergence between a pair of average KL-divergence distributions derived from two selected methods. The resulting score reflects the topological dissimilarity between the pair of methods. Figure 4.16 and Figure A.5 display the KL-divergence between all possible pairs combination of single-view and multigraph fusion methods using AD/LMCI dataset and M/F dataset, respectively, for left and right hemispheres. Remarkably, DGN stands out again with the highest KL-divergence among the other multigraph fusion methods across all datasets and all centrality metrics, while SM-netFusion differs the most among other single-view fusion methods.

### ***Segregation behaviour test***

Another aspect to compare the performance of the graph fusion methods is by evaluating the segregation behavior of their generated CBTs. For that, we computed the local efficiency distribution across the ROIs of each connectional template (nodes graph) using 5-fold cross-validation. Then, we reported the average local efficiency distribution over all sub-populations (testing folds) for AD, LMCI using left and right hemispheres. For a fair comparison, we further computed the ground truth distribution by averaging the local efficiency that are independently calculated for

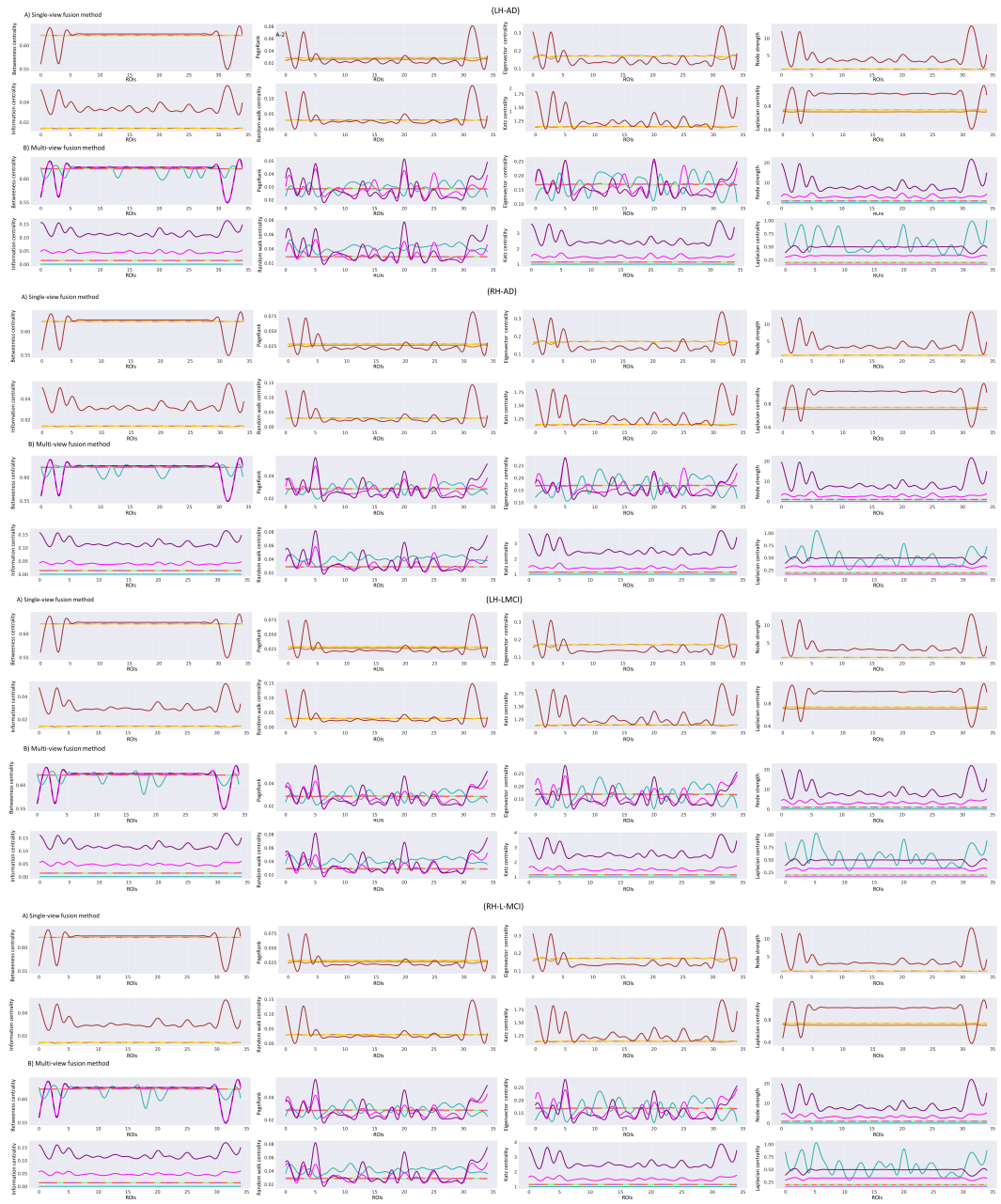


**Figure 4.13 :** Comparison of the average topological distributions across 5-fold cross-validation of PageRank [12], Katz centrality [13], node strength [14], random-walk centrality [15], information centrality [16], Laplacian centrality [17], eigenvector centrality [18], and betweenness centrality [19] of templates generated by **A)** SNF [1], NAG-FS [7], and SM-netFusion [8] against the ground truth distribution for a population of single-view network; and **B)** netNorm [2], SCA [9], MVCF-Net [10], cMGI-Net [20], and DGN [11] against the ground truth distribution for a population of multi-view network for AD and LMCI datasets in the left and right hemispheres.

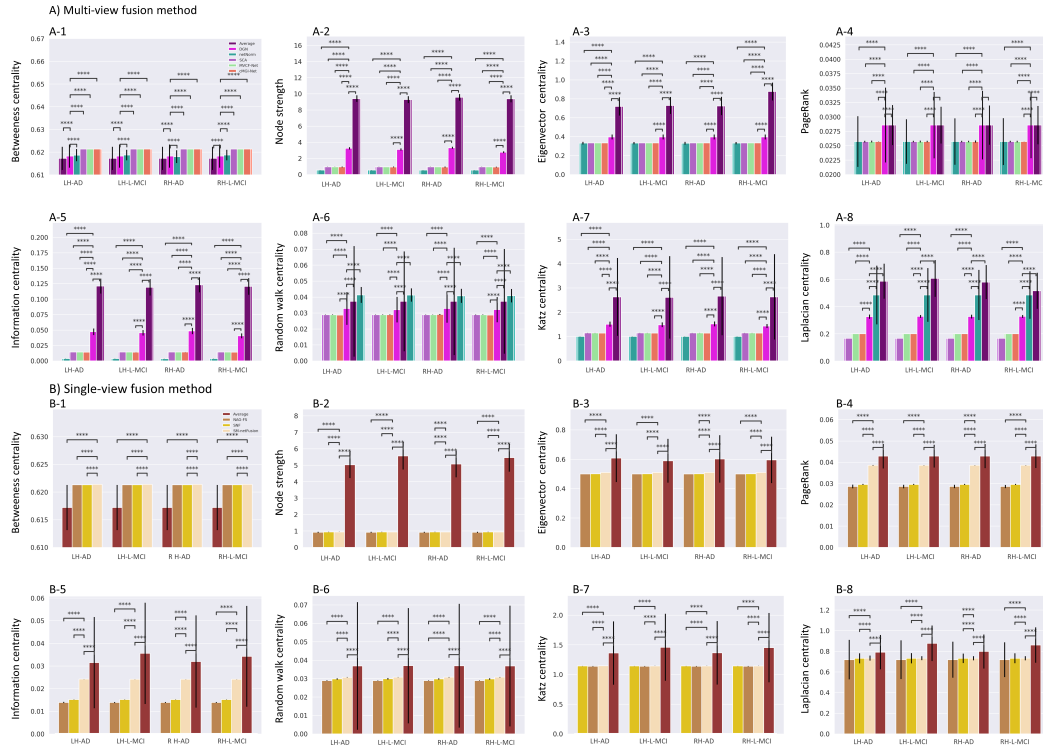


**Figure 4.14 :** This chart displays the average topological distributions of PageRank [12], Katz centrality [13], node strength [14], random-walk centrality [15], information centrality [16], Laplacian centrality [17], eigenvector centrality [18], and betweenness centrality [19] measures across the nodes (ROIs) of the learned templates generated by **A)** SNF [1], NAG-FS [7], and SM-netFusion [8] against the ground truth distribution of a population of single-view networks; and **B)** netNorm [2], SCA [9], MVCF-Net [10], cMGI-Net [20], and DGN [11] against the ground truth distribution of a population of multi-view network for the AD and LMCI datasets in the left and right hemispheres. For multi-graph fusion methods comparison, DGN achieved the highest average distribution comparing to the average distribution of other multigraph fusion methods with a high statistical significance demonstrated by a two-tailed paired t-test (all  $p < 0.0001$ ) for DGN-SCA, DGN-netNorm, DGN-MVCFNet, and DGN-cMGI-Net pairs for AD (LH), AD (RH), LMCI (LH) and LMCI (RH) groups, except for the random-walk centrality measures. For single-view fusion methods comparison, SM-netFusion significantly achieved the maximum average distribution comparing to SNF and NAG-FS for all centrality measures except the betweenness centrality and node strength for AD (LH), AD (RH), LMCI (LH) and LMCI (RH) datasets.

each view of each testing subject. Figure 4.17 and Figure A.7 showed that DGN has the most similar distribution with the ground truth for AD, LMCI, M, and F datasets using both hemispheres. While SM-netFusion displayed the closest distribution. For easy visualization of the results, we displayed the average local efficiency distribution over the ROIs for the ground truth brain networks and the learned CBT by different methods. Remarkably, Figure 4.18 and Figure A.8 section B confirmed that DGN achieves the highest average local efficiency over regions compared to other methods for AD (LH), AD (RH), LMCI (LH) and LMCI (RH) datasets. This can be explained by the fact that DGN aggregates the information passed by its neighbours while taking into consideration the multi-view attributes of its neighboring edges. This was done by integrating graph convolution layers which act as edge conditioned filter learner to learn deeper embeddings for each ROI. As results, the information is efficiently transferred to neighboring nodes while fusing the population of multigraph networks. For single-view fusion methods comparison, SM-netFusion slightly achieved the highest average local efficiency over regions comparing to SNF and NAG-FS for ASD/LMCI and M/F datasets (Figure 4.18 and Figure A.8 section A).

### ***Integration behaviour test***

Furthermore, we compared the integration behavior between the estimated connectional templates using the coefficient participation metric, which quantifies the connection strength (node's edges) between communities (modules) in the graph for ASD/LMCI and M/F datasets Figure 4.18 and Figure A.8. We computed the average participation coefficient across five folds for the CBTs generated by each graph fusion methods and the ground truth network data, respectively. We acquired the ground truth by averaging the participation coefficient measures which are separately calculated for each testing sample and for each view network. We demonstrated that DGN achieves the maximum average participation coefficient compared to other multigraph fusion methods, and the closest score to the ground truth with a high statistical significance demonstrated by a two-tailed paired t-test (all  $p < 0.0001$ ) for DGN-SCA, DGN-netNorm, DGN-MVCFNet, and DGN-cMGI-Net pairs for AD (LH), AD (RH), LMCI (LH) and LMCI (RH) groups (Figure 4.18 section B) as well as for F (LH), F (RH), M (LH) and M (RH) populations (Figure A.8 section B). This

can be explained by the fact that DGN learns the optimized integration of multigraph networks into a single representation population graph in an end-to-end manner using GNN-based integrator while taking into account the data heterogeneity and complementary information across views within the same multigraph. For single-view fusion method comparison, SM-netFusion significantly displayed the highest average participation coefficient comparing to SNF and NAG-FS for AD, LMCI, M, and F in both left and right hemispheres (Figure 4.18 and Figure A.8 section A).

#### **4.3.2.4 CBT global-level similarity test**

As for the evaluation of the global-level similarity of the learned brain connectional templates, we included modularity and global efficiency measures. We computed the average modularity and the average global efficiency over the random sample partitions of the learned CBTs by different fusion methods. Next, we calculated the modularity and the global efficiency for each view of each testing sample and we averaged them to acquire the measures of the ground truth. We demonstrated that DGN significantly outperforms other multigraph fusion methods across evaluation datasets (AD, LMCI, M, and F) for both hemispheres (Figure 4.18 and Figure A.8 section B), two-tailed paired t-test,  $p < 0.0001$ ). This result is the outcome of DGN learning process of fusing multigraph brain networks while preserving the connections strength in the entire graph structure across subjects, and thus preserving the brain graph communities. Specifically, DGN introduces a randomized weighted loss function (SLN) that optimizes connectivity weights of the generated CBT to ensure its representativeness in term of community structures. For the single-view fusion methods comparison, SM-netFusion significantly achieved the maximum average modularity comparing to SNF and NAG-FS for AD, LMCI, M, and F in both left and right hemispheres (Figure 4.18 and Figure A.8 section A), two-tailed paired t-test,  $p < 0.0001$ ).

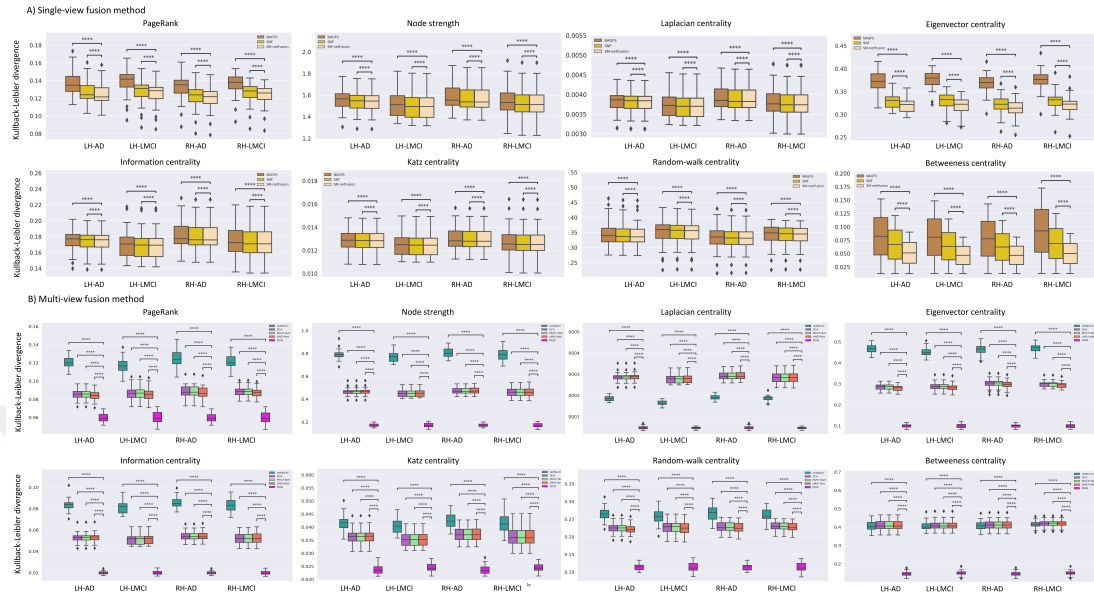


**Figure 4.15 :** Average of Kullback-Liebler divergence distribution across 5-fold cross validation between the ground truth distribution and the average topological distributions of the learned connectional templates generated by **A)** single-view fusion methods (SNF [1], NAG-FS [7], and SM-netFusion [8]); and **B)** multigraph fusion methods (SCA [9], netNorm [2], MVCF-Net [10], cMGI-Net [20], and DGN [11]). The topological measures include PageRank [12], Katz centrality [13], node strength [14], random-walk centrality [15], information centrality [16], Laplacian centrality [17], eigenvector centrality [18], and betweenness centrality [19]. Charts illustrate that for multi-graph fusion methods comparison, DGN achieved the minimum mean KL-divergence distribution and the narrowest dispersion range with a high statistical significance demonstrated by a two-tailed paired t-test (all  $p < 0.0001$ ) for DGN-SCA, DGN-netNorm, DGN-MVCFNet, and DGN-cMGI-Net pairs for AD-LH, AD-RH, LMCI-LH and LMCI-RH groups. For single-view fusion methods comparison, SM-netFusion significantly achieved the lowest mean KL-divergence distribution to the population single-view networks (all  $p < 0.0001$ ) using two-tailed paired t-test for SM-netFusion-NAGFS, and SM-netFusion-SNF pairs for AD-LH, AD-RH, LMCI-LH and LMCI-RH datasets. [Box plot legend: median (midline), box (25th and 75th percentiles), and whiskers (extrema)].



**Figure 4.16 :** Dissimilarity between the possible pairs combination of **A)** single-view and **B)** multigraph fusion methods using KL-divergence for the AD and LMCI in the left and the right hemispheres.

### 4.3.2.5 CBT distance-based similarity test

To evaluate the similarity between the estimated connectional templates by different methods, we computed both Hamming distance and Jaccard distance between all possible pairs combination of the learned connectional templates generated by single-view and multigraph fusion methods, separately, using AD, LMCI, M, and F for left and right hemispheres. Remarkably, the CBT learned by DGN method stands out with the highest Hamming and Jaccard distances among CBTs generated by other multigraph fusion methods across all datasets (Figure 4.19 and Figure A.6 section B). The large difference (dissimilarity) between DGN-based CBT and other integration methods-based CBTs can be explained by the fact that DGN, which is based on

is a geometric deep learning-based (GDL) architecture, normalizes a population of multigraph networks into single generic representation in end-to-end manner unlike other methods except cMGI-Net. Furthermore, the SNL introduced in DGN acts as a regularizer to the overfitting and the overlooking of the model while assigning weights to the views, thus helps to avoid view-biased CBT estimation to minimize the distance between the population and its estimated CBT unlike cMGI-Net. All those different components of DGN architecture promote the generation of distinct CBT unlike other connectional brain templates. For single-view fusion methods comparison, SM-netFusion differs the most among other single-view fusion methods for AD, LMCI, M, and F in both hemispheres (Figure 4.19 and (Figure A.6 section A)).

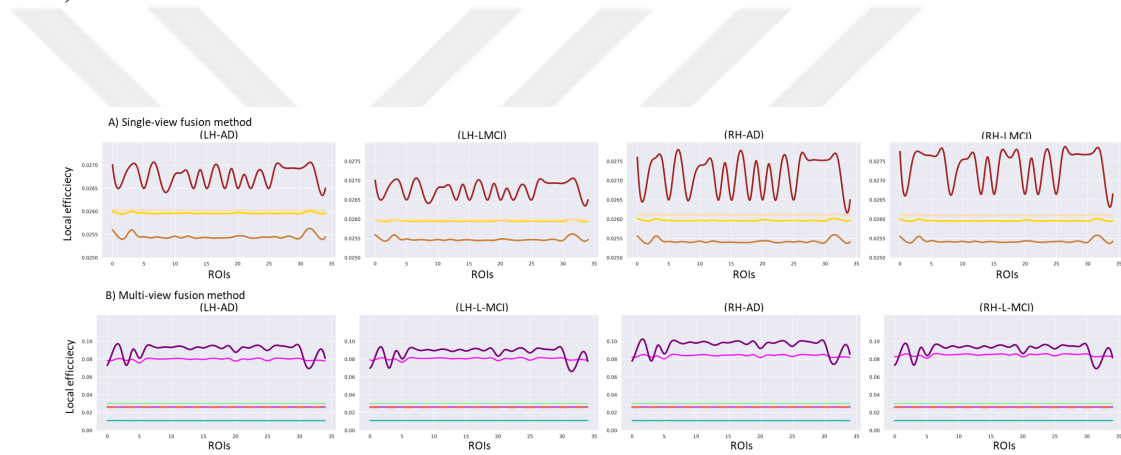


**Figure 4.17 :** Region-wise local efficiency distribution of connectional brain templates generated by **A)** SNF [1], NAG-FS [7], and SM-netFusion [8] against the ground truth distribution for single-view fusion methods comparison; and **B)** netNorm [2], SCA [9], MVCF-Net [10], cMGI-Net [20], and DGN [11] against the ground truth for multi-graph integration methods using 5-fold cross-validation for the AD and LMCI populations in the left and right hemispheres. For multi-graph fusion methods comparison, DGN achieved the most similar distribution to the ground truth while SM-netFusion displayed the closest distribution.

#### 4.3.2.6 Limitation and future directions

Although DGN outperformed other fusion models in the target brain multigraph integration task, it has a few limitations that could be overcome in future work. First, DGN is limited to static brain networks (fixed-time data points) and may not easily be adapted to more sophisticated network structures such as networks with

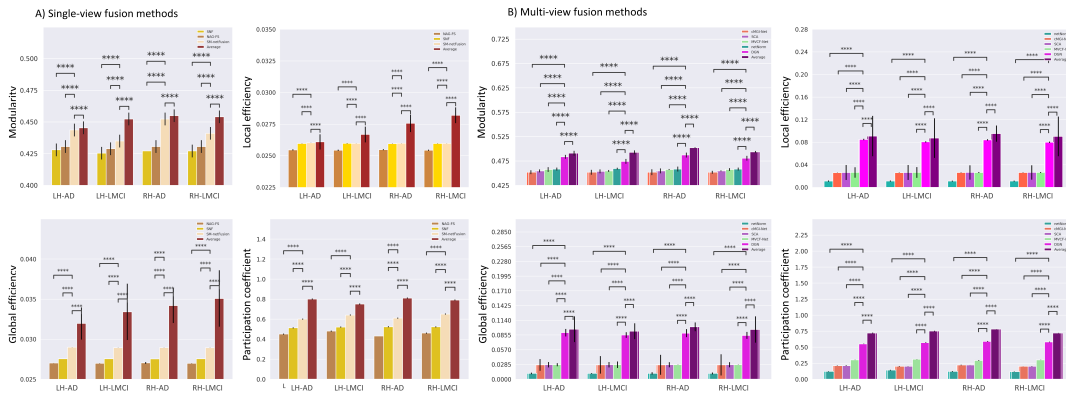


**Figure 4.18 :** Charts display the average local efficiency distribution across regions (ROIs), modularity, global efficiency, and participation coefficient of connectional brain templates estimated by **A)** single-view fusion methods (SNF [1], NAG-FS [7], and SM-netFusion [8]) and **B)** multigraph fusion methods (netNorm [2], SCA [9], MVCF-Net [10], cMGI-Net [20], and DGN [11]) against the ground truth for AD-LH, LMCI-LH, AD-RH, and LMCI-RH groups using 5-fold cross validation. Remarkably, DGN achieved the highest scores including average local efficiency distribution over regions, modularity, participation coefficient, and global efficiency comparing to other multigraph fusion methods with a high statistical significance demonstrated by a two-tailed paired t-test (all  $p < 0.0001$ ) for DGN-SCA, DGN-netNorm, DGN-MVCFNet, and DGN-cMGI-Net pairs for AD-LH, AD-RH, LMCI-LH and LMCI-RH groups. While for the single-view integration methods comparison, SM-netFusion significantly outperformed SNF and NAG-FS for AD and LMCI datasets in both hemispheres (all  $p < 0.0001$ ).

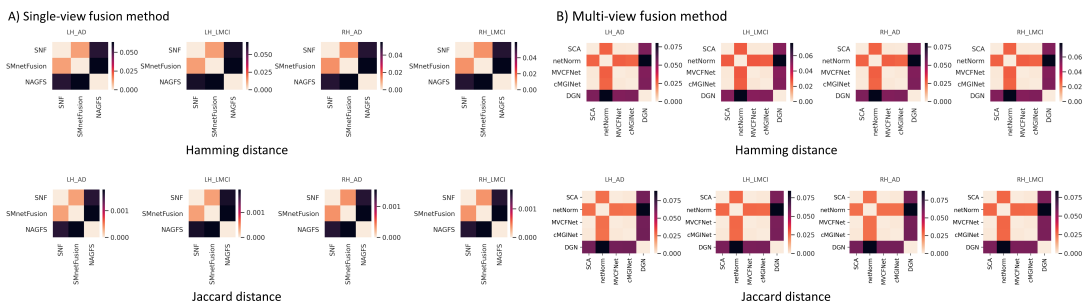


**Figure 4.19 :** Pairwise distance comparison of the learned connectional templates generated by **A)** single-view fusion methods (SNF [1], NAG-FS [7], and SM-netFusion [8]); and **B)** multigraph fusion methods (netNorm [2], SCA [9], MVCF-Net [10], cMGI-Net [20], and DGN [11]) using Hamming distance and Jaccard distance measures for AD and LMCI populations in the left and right hemispheres.

dynamic connectivity [142]. Alternatively, multimodal fusion models with flexible and powerful generic architecture can be developed to enable the evaluation of data with time-dependent brain multigraph population. For instance, geometric recurrent neural networks (RNNs) based on graph convolutional operations can be used to fuse dynamic brain networks derived from MRI measurements acquired at different time points to reveal the trajectory of neurological diseases [143]. Second, all comparative graph fusion methods including DGN, they assume that all network views contain the same number of nodes. Alternatively, DGN model can be extended to handle non-isomorphic graphs with varying numbers of nodes. For instance, [144] propose a generalization of GNNs, so-called k-dimensional GNNs (k-GNNs), which can take higher-order graph structures at multiple scales into account and maps any different graphs to different embeddings. Also inspired from GNNs and the Weisfeiler-Lehman (WL) graph isomorphism test, [54] proposed a powerful GNN-based model that distinguishes isomorphic and non-isomorphic graph structures by mapping them to different representations in the embedding space.

Furthermore, DGN is limited by generating single population-based CBT which may not be discriminative enough to disentangle two specific groups. One solution is to train an auxiliary GNN classifier which forces the fusion model to learn how to capture the most discriminative connectional traits differentiating between several brain network populations. Specifically, a classification task can be added to the fusion process to boost the differences between group connectional templates, and thus the learned templates can be useful to study specific population pairs (i.e., brain disorder, gender differences). Finally, we evaluated DGN on unimodal data for CBT generation. In the future work, we can generalize our comparison study to integrate multi-modal brain networks such as functional and structural brain networks at the same time while capitalizing on geometric deep learning for estimating holistic CBTs and investigating populations difference at functional and structural levels.

In summary, our comparison studies evaluating the performance of the learned brain connectional templates (CBTs) generated by single-view fusion methods and by multigraph fusion methods, separately, demonstrate that DGN outperforms other

multigraph fusion methods in terms of producing the most centered templates, preserving the complex topology of biological networks, and encapsulating the most unique traits of a population of multiview networks, which makes it easily distinguishable from other population templates. Additionally, we showed that the population-representative connectional template generated by DGN achieves the most similar graph structure with a population of multigraph networks at the local scale, the global scale, and distance-based scale. DGN proved its efficiency by estimating a connectional brain templates that fingerprint the population of multi-view brain networks. For example, DGN-connectional brain templates that fingerprint the population of multi-view brain networks derived from T1-weighted MRI scans have revealed a set of biomarkers for both Alzheimer's diseases and Late Mild Cognitive Impairment.

## 5. CONCLUSIONS

Gender may have a substantial influence on human cognitive functions, including emotion, memory, perception, etc., [145]. Men and women appear to have different ways to encode memories, sense emotions, recognize faces, solve certain problems, and make decisions. Since the brain controls cognition and behaviors, investigating the difference of men and women brains is an important underpinning to understand the pathophysiology of many neurological disorders, thus boosting neurological disorder diagnosis and prognosis as well as guiding clinicians in early symptomatic treatment strategies. In current clinical practice, structural brain imaging (CT or MRI) and functional brain methods, such as PET scanning of glucose metabolism were employed to detect the gender differences in the human brain, while gender-related morphological differences was overlooked.

On the other hand, despite the growing number of neuroimaging modalities, certain limitations could result in sacrificing some imaging modalities to have the most important one. In this thesis, we proposed a medical computer aided diagnosis tools enabling to address the key challenges related to brain networks collected from multiple morphological modality (i.e., multi-source data) in order to extract the most discriminative brain features (specific brain regions and connectivities) that differentiate between men and women as well as to boost gender prediction:

First, we proposed how to estimate representative and centered brain network atlases to generate gender fingerprinting, which can be leveraged to identify discriminative brain connectivities between men and women populations. To do so, we defined the first multiview cortical morphological networks clustering and Fusion Network (MVCF-Net) method which achieved the best results in terms of representativeness and centeredness of the generated brain template for each population in comparison to state-of-the-integration method (SCA) introduced in (Dhifallah et al. 2019). We

also used MVCF-Net to identify the most discriminative fingerprinting regions of the brain that distinguish between genders. To sum up, the estimation of centered brain network templates provides a new and exciting venue for better understanding a wide gender difference and easily and effectively spotting reliable biomarkers for improving diagnosis and prognosis of diseases related to gender. In our future work, we will improve the discriminative power of network atlases to distinguish between genders populations by integrating geometric deep learning approaches.

Second, we design the first end-to-end graph neural network-based model for multigraph classification using morphological brain data with the aim to boost genders classification performance. Our framework MICNet (multigraph integration and classifier network) learns a single-view graph representation of a heterogeneous multigraph brain networks prior to classification. While the integration block enables us to preserve the multigraph topological properties, the geometric deep learning-based classifier captures the most discriminative traits of the graph to predict the subject class. Our MICNet significantly outperformed baseline methods on the two-brain genomics superstruct project datasets, thereby showing its great potential in multigraph classification. In our future work, we will evaluate our framework on larger connectomic datasets by generating augmented multigraphs based on population-level integrated templates and eventually enhance the classification performance. Furthermore, we will extend our work to handle multimodal brain graphs covering a diverse range of edge types such as structural and functional connectivities. We also aim to further enhance our framework by implementing attention techniques for multigraphs enables us to preserve the multigraph topological properties.

Third, we review current graph fusion methods that estimate a representative map acting as a connectional fingerprint of single-view and multigraph brain networks populations. These methods integrate a population of heterogeneous brain connectivity networks into a unified representation, hence the concept of connectional brain template (CBT). Furthermore, we conducted a comparative study between the unimodal fusion methods and the multimodal integration methods, separately, by

evaluating the performance of their generated CBTs in terms of (1) well-centeredness (2) discriminativeness, and (3) topological soundness to the population at different scales including node-wise similarity, distance-based similarity, and global-based similarity. We demonstrated that the geometric deep learning architecture-based model, namely Deep Graph Normalizer (DGN) significantly outperforms other multigraph integration methods by generating well-centered, discriminative, and topologically sound connectional templates. Together, these criteria allow DGN to lead the discriminative power in discovering connectional fingerprints that disentangle the differences in brain connectivity between populations while preserving their topological patterns at both local and global graph-levels. In the future work, we can extend our comparison study to cover multi-modal brain networks such as functional and structural brain networks while capitalizing on geometric deep learning for estimating holistic CBTs and investigating populations difference at functional and structural levels. The importance of analyzing brain connectivity patterns in biological datasets which proliferate with unprecedented complexity and heterogeneity opens new frontiers to upgrade the capacity of multigraphs fusion methods to work on multimodal connectomic datasets to learn integral and holistic connectional templates of populations of multi-view networks. Geometric recurrent neural networks based on CNNs can be used to fuse dynamic graphs acquired at different time points to reveal the trajectory of neurological diseases. Also, multigraph fusion methods can be agnostic to the number of nodes using k-dimensional GNNs-based learning models which map non-isomorphic brain networks to different representations in the embedding space.



## REFERENCES

- [1] Wang, B., Mezlini, A.M., Demir, F., Fiume, M., Tu, Z., Brudno, M., Haibe-Kains, B. and Goldenberg, A. (2014). Similarity network fusion for aggregating data types on a genomic scale, *Nature methods*, 11(3), 333.
- [2] Dhifallah, S., Rekik, I., Initiative, A.D.N. et al. (2020). Estimation of connectional brain templates using selective multi-view network normalization, *Medical Image Analysis*, 59, 101567.
- [3] Kipf, T.N. and Welling, M. (2016). Semi-supervised classification with graph convolutional networks, *arXiv preprint arXiv:1609.02907*.
- [4] Varma, M. and Babu, B.R. (2009). More generality in efficient multiple kernel learning, *Proceedings of the 26th Annual International Conference on Machine Learning*, pp.1065–1072.
- [5] Nebli, A. and Rekik, I. (2020). Gender differences in cortical morphological networks, *Brain imaging and behavior*, 14(5), 1831–1839.
- [6] Yu, Y., Zhang, L.H. and Zhang, S. (2019). Simultaneous clustering of multiview biomedical data using manifold optimization, *Bioinformatics*, 35(20), 4029–4037.
- [7] Mhiri, I. and Rekik, I. (2020). Joint functional brain network atlas estimation and feature selection for neurological disorder diagnosis with application to autism, *Medical image analysis*, 60, 101596.
- [8] Mhiri, I., Mahjoub, M.A. and Rekik, I. (2020). Supervised Multi-topology Network Cross-Diffusion for Population-Driven Brain Network Atlas Estimation, *International Conference on Medical Image Computing and Computer-Assisted Intervention*, Springer, pp.166–176.
- [9] Dhifallah, S., Rekik, I., Initiative, A.D.N. et al. (2019). Clustering-based multi-view network fusion for estimating brain network atlases of healthy and disordered populations, *Journal of neuroscience methods*, 311, 426–435.
- [10] Chaari, N., Akdağ, H.C. and Rekik, I. (2020). Estimation of gender-specific connectional brain templates using joint multi-view cortical morphological network integration, *Brain Imaging and Behavior*, 1–20.
- [11] Gurbuz, M.B. and Rekik, I. (2020). Deep Graph Normalizer: A Geometric Deep Learning Approach for Estimating Connectional Brain Templates, *International Conference on Medical Image Computing and Computer-Assisted Intervention*, Springer, pp.155–165.

- [12] **Xing, W. and Ghorbani, A.** (2004). Weighted pagerank algorithm, *Proceedings. Second Annual Conference on Communication Networks and Services Research, 2004.*, IEEE, pp.305–314.
- [13] **Katz, L.** (1953). A new status index derived from sociometric analysis, *Psychometrika*, 18(1), 39–43.
- [14] **Barrat, A., Barthelemy, M., Pastor-Satorras, R. and Vespignani, A.** (2004). The architecture of complex weighted networks, *Proceedings of the national academy of sciences*, 101(11), 3747–3752.
- [15] **Newman, M.E.** (2005). A measure of betweenness centrality based on random walks, *Social networks*, 27(1), 39–54.
- [16] **Stephenson, K. and Zelen, M.** (1989). Rethinking centrality: Methods and examples, *Social networks*, 11(1), 1–37.
- [17] **Qi, X., Fuller, E., Wu, Q., Wu, Y. and Zhang, C.Q.** (2012). Laplacian centrality: A new centrality measure for weighted networks, *Information Sciences*, 194, 240–253.
- [18] **Newman, M.E.** (2008). The mathematics of networks, *The new palgrave encyclopedia of economics*, 2(2008), 1–12.
- [19] **Brandes, U.** (2001). A faster algorithm for betweenness centrality, *Journal of mathematical sociology*, 25(2), 163–177.
- [20] **Demir, U., Gharsallaoui, M.A. and Rekik, I.**, (2020). Clustering-Based Deep Brain MultiGraph Integrator Network for Learning Connectional Brain Templates, Uncertainty for Safe Utilization of Machine Learning in Medical Imaging, and Graphs in Biomedical Image Analysis, Springer, pp.109–120.
- [21] **De Courten-Myers, G.M.** (1999). The human cerebral cortex: gender differences in structure and function, *Journal of Neuropathology and Experimental Neurology*, 58(3), 217–226.
- [22] **Luders, E., Rex, D., Narr, K., Woods, R., Jancke, L., Thompson, P., Mazziotta, J. and Toga, A.** (2003). Relationships between sulcal asymmetries and corpus callosum size: gender and handedness effects, *Cerebral Cortex*, 13(10), 1084–1093.
- [23] **Luders, E., Narr, K.L., Thompson, P.M., Rex, D.E., Woods, R.P., DeLuca, H., Jancke, L. and Toga, A.W.** (2006). Gender effects on cortical thickness and the influence of scaling, *Human brain mapping*, 27(4), 314–324.
- [24] **Im, K., Lee, J.M., Seo, S.W., Kim, S.H., Kim, S.I. and Na, D.L.** (2008). Sulcal morphology changes and their relationship with cortical thickness and gyral white matter volume in mild cognitive impairment and Alzheimer’s disease, *Neuroimage*, 43(1), 103–113.
- [25] **Gong, G., Rosa-Neto, P., Carbonell, F., Chen, Z.J., He, Y. and Evans, A.C.** (2009). Age-and gender-related differences in the cortical anatomical network, *Journal of Neuroscience*, 29(50), 15684–15693.

- [26] **Yan, C., Gong, G., Wang, J., Wang, D., Liu, D., Zhu, C., Chen, Z.J., Evans, A., Zang, Y. and He, Y.** (2011). Sex-and brain size-related small-world structural cortical networks in young adults: a DTI tractography study, *Cerebral cortex*, 21(2), 449–458.
- [27] **Van Essen, D. and Drury, H.** (1997). Structural and functional analyses of human cerebral cortex using a surface-based atlas, *Journal of Neuroscience*, 17(18), 7079–7102.
- [28] **Lisowska, A. and Rekik, I.** (2019). Alzheimer’s Association AbbVie, Alzheimer’s Drug Discovery Foundation, Araclon Biotech, Inc. Bio-Clinica, Biogen, Bristol-Myers Squibb Company, Inc. CereSpir, Cogstate, et al. Joint pairing and structured mapping of convolutional brain morphological multiplexes for early dementia diagnosis, *Brain connectivity*, 9(1), 22–36.
- [29] **Mahjoub, I., Mahjoub, M.A. and Rekik, I.** (2018). Brain multiplexes reveal morphological connective biomarkers fingerprinting late brain dementia states, *Scientific reports*, 8(1), 1–14.
- [30] **Soussia, M. and Rekik, I.** (2018). Unsupervised manifold learning using high-order morphological brain networks derived from T1-w MRI for autism diagnosis, *Frontiers in neuroinformatics*, 12, 70.
- [31] **Seidlitz, J., Váša, F., Shinn, M., Romero-Garcia, R., Whitaker, K.J., Vértes, P.E., Wagstyl, K., Reardon, P.K., Clasen, L., Liu, S. et al.** (2018). Morphometric similarity networks detect microscale cortical organization and predict inter-individual cognitive variation, *Neuron*, 97(1), 231–247.
- [32] **Tyan, Y.S., Liao, J.R., Shen, C.Y., Lin, Y.C. and Weng, J.C.** (2017). Gender Differences in the Structural Connectome of the Teenage Brain Revealed by Diffusion Tensor Imaging, , 28(1), 17–25.
- [33] **Jiang, R., Calhoun, V.D., Fan, L., Zuo, N., Jung, R., Qi, S., Lin, D., Li, J., Zhuo, C., Song, M. et al.** (2020). Gender differences in connectome-based predictions of individualized intelligence quotient and sub-domain scores, *Cerebral Cortex*, 30(3), 888–900.
- [34] **Dadashkarimi, J., Gao, S., Yeagle, E., Noble, S. and Scheinost, D.** (2019). A mass multivariate edge-wise approach for combining multiple connectomes to improve the detection of group differences, *International Workshop on Connectomics in Neuroimaging*, Springer, pp.64–73.
- [35] **Bassett, D.S. and Sporns, O.** (2017). Network neuroscience, *Nature neuroscience*, 20(3), 353–364.
- [36] **Van Essen, D.C. and Glasser, M.F.** (2016). The human connectome project: progress and prospects, *Cerebrum: the Dana forum on brain science*, volume2016, Dana Foundation.

- [37] **Verma, J., Gupta, S., Mukherjee, D. and Chakraborty, T.** (2019). Heterogeneous edge embedding for friend recommendation, *European Conference on Information Retrieval*, Springer, pp.172–179.
- [38] **Sporns, O., Tononi, G. and Kötter, R.** (2005). The human connectome: a structural description of the human brain, *PLoS Comput Biol*, *1*(4), e42.
- [39] **Lisowska, A., Rekik, I., AbbVie, A.A., Foundation, A.D.D., Biotech, A., Bio-Clinica, I., Biogen, Company, B.M.S., CereSpir, I., Cogstate et al.** (2019). Joint pairing and structured mapping of convolutional brain morphological multiplexes for early dementia diagnosis, *Brain connectivity*, *9*(1), 22–36.
- [40] **Georges, N., Mhiri, I., Rekik, I., Initiative, A.D.N. et al.** (2020). Identifying the best data-driven feature selection method for boosting reproducibility in classification tasks, *Pattern Recognition*, *101*, 107183.
- [41] **Watts, D.J. and Strogatz, S.H.** (1998). Collective dynamics of ‘small-world’ networks, *nature*, *393*(6684), 440–442.
- [42] **Fornito, A.** (2016). Graph theoretic analysis of human brain networks, FMRI techniques and protocols, Springer, pp.283–314.
- [43] **Soussia, M. and Rekik, I.** (2019). 7 Years of Developing Seed Techniques for Alzheimer’s Disease Diagnosis Using Brain Image and Connectivity Data Largely Bypassed Prediction for Prognosis, *International Workshop on Predictive Intelligence In Medicine*, Springer, pp.81–93.
- [44] **Bunke, H. and Riesen, K.** (2011). Recent advances in graph-based pattern recognition with applications in document analysis, *Pattern Recognition*, *44*(5), 1057–1067.
- [45] **Kondor, R. and Pan, H.** (2016). The multiscale laplacian graph kernel, *Advances in Neural Information Processing Systems*, pp.2990–2998.
- [46] **Mhiri, I., Khalifa, A.B., Mahjoub, M.A. and Rekik, I.** (2020). Brain graph super-resolution for boosting neurological disorder diagnosis using unsupervised multi-topology connectional brain template learning, *Medical Image Analysis*, *65*, 101768.
- [47] **Defferrard, M., Bresson, X. and Vandergheynst, P.** (2016). Convolutional neural networks on graphs with fast localized spectral filtering, *Advances in neural information processing systems*, pp.3844–3852.
- [48] **Duvenaud, D.K., Maclaurin, D., Iparraguirre, J., Bombarell, R., Hirzel, T., Aspuru-Guzik, A. and Adams, R.P.** (2015). Convolutional networks on graphs for learning molecular fingerprints, *Advances in neural information processing systems*, pp.2224–2232.
- [49] **Bronstein, M.M., Bruna, J., LeCun, Y., Szlam, A. and Vandergheynst, P.** (2017). Geometric deep learning: going beyond euclidean data, *IEEE Signal Processing Magazine*, *34*(4), 18–42.

- [50] **Scarselli, F., Gori, M., Tsoi, A.C., Hagenbuchner, M. and Monfardini, G.** (2008). The graph neural network model, *IEEE Transactions on Neural Networks*, 20(1), 61–80.
- [51] **Simonovsky, M. and Komodakis, N.** (2017). Dynamic edge-conditioned filters in convolutional neural networks on graphs, *Proceedings of the IEEE conference on computer vision and pattern recognition*, pp.3693–3702.
- [52] **Zhang, Y., Pal, S., Coates, M. and Ustebay, D.** (2019). Bayesian graph convolutional neural networks for semi-supervised classification, *Proceedings of the AAAI Conference on Artificial Intelligence*, volume 33, pp.5829–5836.
- [53] **Hamilton, W., Ying, Z. and Leskovec, J.** (2017). Inductive representation learning on large graphs, *Advances in neural information processing systems*, pp.1024–1034.
- [54] **Xu, K., Hu, W., Leskovec, J. and Jegelka, S.** (2018). How powerful are graph neural networks?, *arXiv preprint arXiv:1810.00826*.
- [55] **Zhang, M., Cui, Z., Neumann, M. and Chen, Y.** (2018). An end-to-end deep learning architecture for graph classification, *Thirty-Second AAAI Conference on Artificial Intelligence*.
- [56] **Li, J., Zhang, S., Liu, T., Ning, C., Zhang, Z. and Zhou, W.** (2020). Neural inductive matrix completion with graph convolutional networks for miRNA-disease association prediction, *Bioinformatics*, 36(8), 2538–2546.
- [57] **Ying, Z., You, J., Morris, C., Ren, X., Hamilton, W. and Leskovec, J.** (2018). Hierarchical graph representation learning with differentiable pooling, *Advances in neural information processing systems*, pp.4800–4810.
- [58] **Ingalhalikar, M., Smith, A., Parker, D., Satterthwaite, T.D., Elliott, M.A., Ruparel, K., Hakonarson, H., Gur, R.E., Gur, R.C. and Verma, R.** (2014). Sex differences in the structural connectome of the human brain, *Proceedings of the National Academy of Sciences*, 111(2), 823–828.
- [59] **Zhou, C., Zemanová, L., Zamora, G., Hilgetag, C.C. and Kurths, J.** (2006). Hierarchical organization unveiled by functional connectivity in complex brain networks, *Physical review letters*, 97(23), 238103.
- [60] **Honey, C.J., Kötter, R., Breakspear, M. and Sporns, O.** (2007). Network structure of cerebral cortex shapes functional connectivity on multiple time scales, *Proceedings of the National Academy of Sciences*, 104(24), 10240–10245.
- [61] **Honey, C.J., Sporns, O., Cammoun, L., Gigandet, X., Thiran, J.P., Meuli, R. and Hagmann, P.** (2009). Predicting human resting-state functional connectivity from structural connectivity, *Proceedings of the National Academy of Sciences*, 106(6), 2035–2040.

- [62] **Bolla, K.I., Eldreth, D., Matochik, J. and Cadet, J.** (2004). Sex-related differences in a gambling task and its neurological correlates, *Cerebral cortex*, 14(11), 1226–1232.
- [63] **Spelke, E.S.** (2005). Sex differences in intrinsic aptitude for mathematics and science?: a critical review., *American Psychologist*, 60(9), 950.
- [64] **Koch, K., Pauly, K., Kellermann, T., Seiferth, N.Y., Reske, M., Backes, V., Stöcker, T., Shah, N.J., Amunts, K., Kircher, T. et al.** (2007). Gender differences in the cognitive control of emotion: An fMRI study, *Neuropsychologia*, 45(12), 2744–2754.
- [65] **Keller, K. and Menon, V.** (2009). Gender differences in the functional and structural neuroanatomy of mathematical cognition, *Neuroimage*, 47(1), 342–352.
- [66] **Derntl, B., Finkelmeyer, A., Eickhoff, S., Kellermann, T., Falkenberg, D.I., Schneider, F. and Habel, U.** (2010). Multidimensional assessment of empathic abilities: neural correlates and gender differences, *Psychoneuroendocrinology*, 35(1), 67–82.
- [67] **Zaidi, Z.F.** (2010). Gender differences in human brain: a review, *The open anatomy journal*, 2(1).
- [68] **Wada, J.A., Clarke, R. and Hamm, A.** (1975). Cerebral hemispheric asymmetry in humans: Cortical speech zones in 100 adult and 100 infant brains, *Archives of neurology*, 32(4), 239–246.
- [69] **Petrov, D., Ivanov, A., Faskowitz, J., Gutman, B., Moyer, D., Villalon, J., Jahanshad, N. and Thompson, P.** (2017). Evaluating 35 methods to generate structural connectomes using pairwise classification, *International Conference on medical Image Computing and Computer-Assisted Intervention*, Springer, pp.515–522.
- [70] **Rekik, I., Li, G., Lin, W. and Shen, D.** (2017). Estimation of brain network atlases using diffusive-shrinking graphs: application to developing brains, *International conference on information processing in medical imaging*, Springer, pp.385–397.
- [71] **Acosta-Mendoza, N., Gago-Alonso, A., Carrasco-Ochoa, J.A., Martínez-Trinidad, J.F. and Medina-Pagola, J.E.** (2017). Extension of canonical adjacency matrices for frequent approximate subgraph mining on multi-graph collections, *International Journal of Pattern Recognition and Artificial Intelligence*, 31(08), 1750025.
- [72] **Wu, J., Hong, Z., Pan, S., Zhu, X., Cai, Z. and Zhang, C.** (2014). Multi-graph-view learning for graph classification, *2014 IEEE International Conference on Data Mining*, IEEE, pp.590–599.
- [73] **Geng, X., Wu, X., Zhang, L., Yang, Q., Liu, Y. and Ye, J.** (2019). Multi-modal graph interaction for multi-graph convolution network in urban spatiotemporal forecasting, *arXiv preprint arXiv:1905.11395*.

- [74] **Yun, S., Jeong, M., Kim, R., Kang, J. and Kim, H.J.** (2019). Graph transformer networks, *Advances in Neural Information Processing Systems*, pp.11983–11993.
- [75] **Bullmore, E. and Sporns, O.** (2009). Complex brain networks: graph theoretical analysis of structural and functional systems, *Nature reviews neuroscience*, *10*(3), 186–198.
- [76] **Fornito, A., Zalesky, A. and Breakspear, M.** (2015). The connectomics of brain disorders, *Nature Reviews Neuroscience*, *16*(3), 159–172.
- [77] **Guan, W.j., Ni, Z.y., Hu, Y., Liang, W.h., Ou, C.q., He, J.x., Liu, L., Shan, H., Lei, C.l., Hui, D.S. et al.** (2020). Clinical characteristics of coronavirus disease 2019 in China, *New England journal of medicine*, *382*(18), 1708–1720.
- [78] **Bassett, D.S. and Sporns, O.** (2017). Network neuroscience, *Nature neuroscience*, *20*(3), 353–364.
- [79] **Zhang, S., Zhao, H. and Ng, M.K.** (2015). Functional module analysis for gene coexpression networks with network integration, *IEEE/ACM transactions on computational biology and bioinformatics*, *12*(5), 1146–1160.
- [80] **Absil, P.A., Mahony, R. and Sepulchre, R.** (2009). *Optimization algorithms on matrix manifolds*, Princeton University Press.
- [81] **Pearl, J.** (2014). *Probabilistic reasoning in intelligent systems: networks of plausible inference*, Elsevier.
- [82] **Wang, B., Ramazzotti, D., De Sano, L., Zhu, J., Pierson, E. and Batzoglou, S.** (2018). SIMLR: A tool for large-scale genomic analyses by multi-kernel learning, *Proteomics*, *18*(2), 1700232.
- [83] **Huang, W., Bolton, T.A., Medaglia, J.D., Bassett, D.S., Ribeiro, A. and Van De Ville, D.** (2018). A graph signal processing perspective on functional brain imaging, *Proceedings of the IEEE*, *106*(5), 868–885.
- [84] **Yu, Q., Du, Y., Chen, J., Sui, J., Adalē, T., Pearlson, G.D. and Calhoun, V.D.** (2018). Application of graph theory to assess static and dynamic brain connectivity: Approaches for building brain graphs, *Proceedings of the IEEE*, *106*(5), 886–906.
- [85] **Christmas, W.J., Kittler, J. and Petrou, M.** (1995). Structural matching in computer vision using probabilistic relaxation, *IEEE Transactions on pattern analysis and machine intelligence*, *17*(8), 749–764.
- [86] **Luo, B. and Hancock, E.R.** (2001). Structural graph matching using the EM algorithm and singular value decomposition, *IEEE Transactions on Pattern Analysis and Machine Intelligence*, *23*(10), 1120–1136.

- [87] **Mheich, A., Hassan, M., Khalil, M., Gripon, V., Dufor, O. and Wendling, F.** (2017). SimiNet: a novel method for quantifying brain network similarity, *IEEE transactions on pattern analysis and machine intelligence*, 40(9), 2238–2249.
- [88] **Shimada, Y., Hirata, Y., Ikeguchi, T. and Aihara, K.** (2016). Graph distance for complex networks, *Scientific reports*, 6(1), 1–6.
- [89] **Wilson, R.C. and Zhu, P.** (2008). A study of graph spectra for comparing graphs and trees, *Pattern Recognition*, 41(9), 2833–2841.
- [90] **Guimera, R., Mossa, S., Turttschi, A. and Amaral, L.N.** (2005). The worldwide air transportation network: Anomalous centrality, community structure, and cities' global roles, *Proceedings of the National Academy of Sciences*, 102(22), 7794–7799.
- [91] **Latora, V. and Marchiori, M.** (2001). Efficient behavior of small-world networks, *Physical review letters*, 87(19), 198701.
- [92] **Gao, X., Xiao, B., Tao, D. and Li, X.** (2010). A survey of graph edit distance, *Pattern Analysis and applications*, 13(1), 113–129.
- [93] **Levandowsky, M. and Winter, D.** (1971). Distance between sets, *Nature*, 234(5323), 34–35.
- [94] **Newman, M.E. and Girvan, M.** (2004). Finding and evaluating community structure in networks, *Physical review E*, 69(2), 026113.
- [95] **Achard, S. and Bullmore, E.** (2007). Efficiency and cost of economical brain functional networks, *PLoS Comput Biol*, 3(2), e17.
- [96] **O'Keefe, T., Petrov, V., Buckner, R., Holmes, A. and Fariello, G.** (2012). The informatics backbone of the brain genomics superstruct project open data release, *The annual International Neuroinformatics Coordinating Facility Congress, Munich, Germany*.
- [97] **Holmes, A.J., Hollinshead, M.O., O'keefe, T.M., Petrov, V.I., Fariello, G.R., Wald, L.L., Fischl, B., Rosen, B.R., Mair, R.W., Roffman, J.L. et al.** (2015). Brain Genomics Superstruct Project initial data release with structural, functional, and behavioral measures, *Scientific data*, 2(1), 1–16.
- [98] **Fischl, B., Van Der Kouwe, A., Destrieux, C., Halgren, E., Ségonne, F., Salat, D.H., Busa, E., Seidman, L.J., Goldstein, J., Kennedy, D. et al.** (2004). Automatically parcellating the human cerebral cortex, *Cerebral cortex*, 14(1), 11–22.
- [99] **Fischl, B.** (2012). FreeSurfer, *Neuroimage*, 62(2), 774–781.
- [100] **Witelson, S.F. and Pallie, W.** (1973). Left hemisphere specialization for language in the newborn: Neuroanatomical evidence of asymmetry, *Brain*, 96(3), 641–646.

- [101] **Tian, L., Wang, J., Yan, C. and He, Y.** (2011). Hemisphere-and gender-related differences in small-world brain networks: a resting-state functional MRI study, *Neuroimage*, 54(1), 191–202.
- [102] **Amunts, K., Armstrong, E., Malikovic, A., Hömke, L., Mohlberg, H., Schleicher, A. and Zilles, K.** (2007). Gender-specific left–right asymmetries in human visual cortex, *Journal of Neuroscience*, 27(6), 1356–1364.
- [103] **Takahashi, R., Ishii, K., Kakigi, T. and Yokoyama, K.** (2011). Gender and age differences in normal adult human brain: Voxel-based morphometric study, *Human brain mapping*, 32(7), 1050–1058.
- [104] **Yang, X., Peng, Z., Ma, X., Meng, Y., Li, M., Zhang, J., Song, X., Liu, Y., Fan, H., Zhao, L. et al.** (2017). Sex differences in the clinical characteristics and brain gray matter volume alterations in unmedicated patients with major depressive disorder, *Scientific reports*, 7(1), 1–8.
- [105] **Diano, M., Tamietto, M., Celegnin, A., Weiskrantz, L., Tatu, M.K., Bagnis, A., Duca, S., Geminiani, G., Cauda, F. and Costa, T.** (2017). Dynamic changes in amygdala psychophysiological connectivity reveal distinct neural networks for facial expressions of basic emotions, *Scientific reports*, 7(1), 1–13.
- [106] **Yu, K., Wang, X., Li, Q., Zhang, X., Li, X. and Li, S.** (2018). Individual morphological brain network construction based on multivariate euclidean distances between brain regions, *Frontiers in human neuroscience*, 12, 204.
- [107] **Chiron, C., Leboyer, M., Leon, F., Jambaque, L., Nuttin, C. and Syrota, A.** (1995). SPECT of the brain in childhood autism: evidence for a lack of normal hemispheric asymmetry, *Developmental Medicine & Child Neurology*, 37(10), 849–860.
- [108] **Proverbio, A.M., Brignone, V., Matarazzo, S., Del Zotto, M. and Zani, A.** (2006). Gender and parental status affect the visual cortical response to infant facial expression, *Neuropsychologia*, 44(14), 2987–2999.
- [109] **Proverbio, A.M., Mazzara, R., Riva, F. and Manfredi, M.** (2012). Sex differences in callosal transfer and hemispheric specialization for face coding, *Neuropsychologia*, 50(9), 2325–2332.
- [110] **Good, C.D., Johnsrude, I., Ashburner, J., Henson, R.N., Friston, K.J. and Frackowiak, R.S.** (2001). Cerebral asymmetry and the effects of sex and handedness on brain structure: a voxel-based morphometric analysis of 465 normal adult human brains, *Neuroimage*, 14(3), 685–700.
- [111] **Cheng, Y., Chou, K.H., Decety, J., Chen, I.Y., Hung, D., Tzeng, O.L. and Lin, C.P.** (2009). Sex differences in the neuroanatomy of human mirror-neuron system: a voxel-based morphometric investigation, *Neuroscience*, 158(2), 713–720.

- [112] **Clower, D.M., West, R.A., Lynch, J.C. and Strick, P.L.** (2001). The inferior parietal lobule is the target of output from the superior colliculus, hippocampus, and cerebellum, *Journal of Neuroscience*, 21(16), 6283–6291.
- [113] **Radua, J., Phillips, M.L., Russell, T., Lawrence, N., Marshall, N., Kalidindi, S., El-Hage, W., McDonald, C., Giampietro, V., Brammer, M.J. et al.** (2010). Neural response to specific components of fearful faces in healthy and schizophrenic adults, *Neuroimage*, 49(1), 939–946.
- [114] **Xu, C., Li, C., Wu, H., Wu, Y., Hu, S., Zhu, Y., Zhang, W., Wang, L., Zhu, S., Liu, J. et al.** (2015). Gender differences in cerebral regional homogeneity of adult healthy volunteers: a resting-state fMRI study, *BioMed research international*, 2015.
- [115] **Hyde, J.S. and Linn, M.C.** (1988). Gender differences in verbal ability: a meta-analysis., *Psychological bulletin*, 104(1), 53.
- [116] **Kimura, D.** (1997). Sex, sexual orientation and sex hormones influence human cognitive function, *Biomedical Reviews*, 7, 33–39.
- [117] **Rahman, Q., Wilson, G.D. and Abrahams, S.** (2004). Sex, sexual orientation, and identification of positive and negative facial affect, *Brain and cognition*, 54(3), 179–185.
- [118] **Crespo-Facorro, B., Roiz-Santiañez, R., Pérez-Iglesias, R., Mata, I., Rodríguez-Sánchez, J.M., Tordesillas-Gutiérrez, D., de la Foz, V.O.G., Tabarés-Seisdedos, R., Sánchez, E., Andreasen, N. et al.** (2011). Sex-specific variation of MRI-based cortical morphometry in adult healthy volunteers: the effect on cognitive functioning, *Progress in Neuro-Psychopharmacology and Biological Psychiatry*, 35(2), 616–623.
- [119] **Naito, E., Kinomura, S., Geyer, S., Kawashima, R., Roland, P.E. and Zilles, K.** (2000). Fast reaction to different sensory modalities activates common fields in the motor areas, but the anterior cingulate cortex is involved in the speed of reaction, *Journal of Neurophysiology*, 83(3), 1701–1709.
- [120] **Allen, L.S., Richey, M.F., Chai, Y.M. and Gorski, R.A.** (1991). Sex differences in the corpus callosum of the living human being, *Journal of Neuroscience*, 11(4), 933–942.
- [121] **Clements-Stephens, A.M., Rimrodt, S.L. and Cutting, L.E.** (2009). Developmental sex differences in basic visuospatial processing: differences in strategy use?, *Neuroscience letters*, 449(3), 155–160.
- [122] **Chen, C., Ng, M.K. and Zhang, S.** (2017). Block spectral clustering methods for multiple graphs, *Numerical Linear Algebra with Applications*, 24(1), e2075.
- [123] **Rubin, L.H., Yao and Li** (2017). Sex differences in associations of arginine vasopressin and oxytocin with resting-state functional brain connectivity, *Journal of neuroscience research*, 95(1-2), 576–586.

- [124] **McGlone, J.** (1980). Sex differences in human brain asymmetry: A critical survey, *Behavioral and brain sciences*, 3(2), 215–227.
- [125] **Stone, V.E., Nisenson, L., Eliassen, J.C. and Gazzaniga, M.S.** (1996). Left hemisphere representations of emotional facial expressions, *Neuropsychologia*, 34(1), 23–29.
- [126] **Kovalev, V.A., Kruggel, F. and von Cramon, D.Y.** (2003). Gender and age effects in structural brain asymmetry as measured by MRI texture analysis, *NeuroImage*, 19(3), 895–905.
- [127] **Tranel, D., Damasio, H., Denburg, N.L. and Bechara, A.** (2005). Does gender play a role in functional asymmetry of ventromedial prefrontal cortex?, *Brain*, 128(12), 2872–2881.
- [128] **Fischl, B., Salat, D.H., Van Der Kouwe, A.J., Makris, N., Ségonne, F., Quinn, B.T. and Dale, A.M.** (2004). Sequence-independent segmentation of magnetic resonance images, *Neuroimage*, 23, S69–S84.
- [129] **Rasmussen, P.M., Hansen, L.K., Madsen, K.H., Churchill, N.W. and Strother, S.C.** (2012). Model sparsity and brain pattern interpretation of classification models in neuroimaging, *Pattern Recognition*, 45(6), 2085–2100.
- [130] **Liang, X., Zhao, C., Jin, X., Jiang, Y., Yang, L., Chen, Y. and Gong, G.** (2021). Sex-related human brain asymmetry in hemispheric functional gradients, *NeuroImage*, 117761.
- [131] **Wen, H., Liu, Y., Rekik, I., Wang, S., Chen, Z., Zhang, J., Zhang, Y., Peng, Y. and He, H.** (2017). Multi-modal multiple kernel learning for accurate identification of Tourette syndrome children, *Pattern Recognition*, 63, 601–611.
- [132] **Boddaert, N., Chabane, N., Gervais, H., Good, C., Bourgeois, M., Plumet, M., Barthelemy, C., Mouren, M., Artiges, E., Samson, Y. et al.** (2004). Superior temporal sulcus anatomical abnormalities in childhood autism: a voxel-based morphometry MRI study, *Neuroimage*, 23(1), 364–369.
- [133] **de Salas-Quiroga, A., García-Rincón, D., Gómez-Domínguez, D., Valero, M., Simón-Sánchez, S., Paraíso-Luna, J., Agualeles, J., Pujadas, M., Muguruza, C., Callado, L.F. et al.** (2020). Long-term hippocampal interneuronopathy drives sex-dimorphic spatial memory impairment induced by prenatal THC exposure, *Neuropsychopharmacology*, 45(5), 877–886.
- [134] **Diekhof, E.K., Keil, M., Obst, K.U., Henseler, I., Dechent, P., Falkai, P. and Gruber, O.** (2012). A functional neuroimaging study assessing gender differences in the neural mechanisms underlying the ability to resist impulsive desires, *Brain research*, 1473, 63–77.
- [135] **Filimon, F., Nelson, J.D., Hagler, D.J. and Sereno, M.I.** (2007). Human cortical representations for reaching: mirror neurons for execution, observation, and imagery, *Neuroimage*, 37(4), 1315–1328.

- [136] **Van Schuerbeek, P., Baeken, C., De Raedt, R., De Mey, J. and Luybaert, R.** (2011). Individual differences in local gray and white matter volumes reflect differences in temperament and character: a voxel-based morphometry study in healthy young females, *Brain Research*, 1371, 32–42.
- [137] **Culham, J.C., Cavina-Pratesi, C. and Singhal, A.** (2006). The role of parietal cortex in visuomotor control: what have we learned from neuroimaging?, *Neuropsychologia*, 44(13), 2668–2684.
- [138] **Hirjak, D., Thomann, A.K., Kubera, K.M., Wolf, R.C., Jeung, H., Maier-Hein, K.H. and Thomann, P.A.** (2017). Cortical folding patterns are associated with impulsivity in healthy young adults, *Brain imaging and behavior*, 11(6), 1592–1603.
- [139] **Vaswani, A., Shazeer, N., Parmar, N., Uszkoreit, J., Jones, L., Gomez, A.N., Kaiser, Ł. and Polosukhin, I.** (2017). Attention is all you need, *Advances in neural information processing systems*, 30, 5998–6008.
- [140] **Weiner, M.W., Veitch, D.P., Aisen, P.S., Beckett, L.A., Cairns, N.J., Cedarbaum, J., Donohue, M.C., Green, R.C., Harvey, D., Jack Jr, C.R. et al.** (2015). Impact of the Alzheimer’s disease neuroimaging initiative, 2004 to 2014, *Alzheimer’s & Dementia*, 11(7), 865–884.
- [141] **Desikan, R.S., Ségonne, F., Fischl, B., Quinn, B.T., Dickerson, B.C., Blacker, D., Buckner, R.L., Dale, A.M., Maguire, R.P., Hyman, B.T. et al.** (2006). An automated labeling system for subdividing the human cerebral cortex on MRI scans into gyral based regions of interest, *Neuroimage*, 31(3), 968–980.
- [142] **Bessadok, A., Mahjoub, M.A. and Rekik, I.** (2021). Graph Neural Networks in Network Neuroscience, *arXiv preprint arXiv:2106.03535*.
- [143] **Ezzine, B.E. and Rekik, I.** (2019). Learning-guided infinite network atlas selection for predicting longitudinal brain network evolution from a single observation, *International Conference on Medical Image Computing and Computer-Assisted Intervention*, Springer, pp.796–805.
- [144] **Morris, C., Ritzert, M., Fey, M., Hamilton, W.L., Lenssen, J.E., Rattan, G. and Grohe, M.** (2019). Weisfeiler and leman go neural: Higher-order graph neural networks, *Proceedings of the AAAI Conference on Artificial Intelligence*, volume 33, pp.4602–4609.
- [145] **Cahill, L.** (2006). Why sex matters for neuroscience, *Nature reviews neuroscience*, 7(6), 477–484.

## **APPENDICES**

**APPENDIX A** :Additional experiments provided on Brain Genomics Superstruct Project (GSP) dataset.





## APPENDIX A:

Additional experiments provided on Brain Genomics Superstruct Project (GSP) dataset.

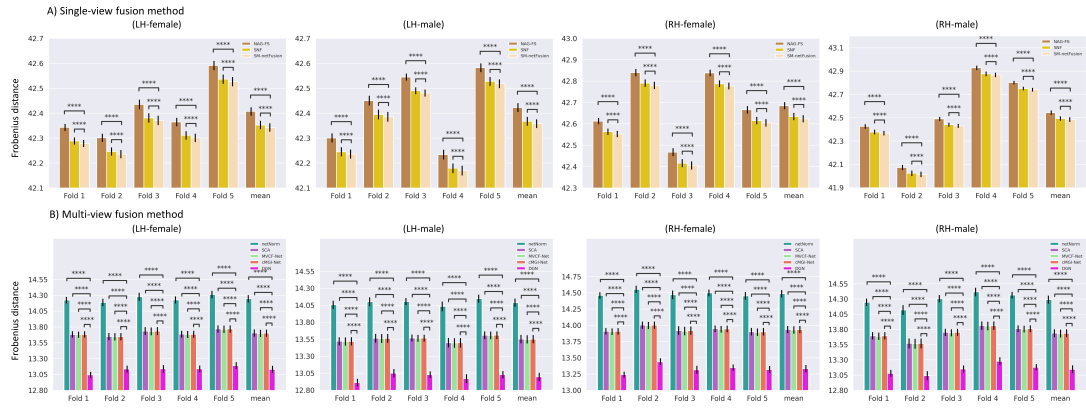


**Figure A.1 :** Centeredness comparison of connectional templates generated by **A)** single-view integration methods including network atlas-guided feature selection (NAG-FS) [7], similarity network fusion (SNF) [1], and supervised multi-topology network cross-diffusion (SM-netFusion) [8]; and **B)** multi-graph fusion methods including multi-view networks normalizer (netNorm) [2], cluster-based network fusion (SCA) [9], multi-view clustering and fusion (MVCF-Net) [10], cluster-based multi-graph integrator networks (cMGI-Net) [20], and deep graph normalizer (DGN) [11]. Charts illustrate the mean Frobenius distance between the connectional templates learned from the training sets and networks of the samples in the testing set using a 5-fold cross-validation strategy. We reported the average distance for each cross-validation fold as well as the average across folds (“Mean” bars on the right). For multi-graph fusion methods comparison, DGN achieved the lowest mean Frobenius distance to the population multi-view networks with a high statistical significance demonstrated by a two-tailed paired t-test (all  $p < 0.0001$ ) for DGN-SCA, DGN-netNorm, DGN-MVCFNet, and DGN-cMGI-Net pairs for M-LH, M-RH, F-LH and F-RH groups. LH: left hemisphere. RH: right hemisphere. M: Male population. F: Female population. As for single-view fusion methods comparison, SM-netFusion significantly achieved the lowest mean Frobenius distance to the population single-view networks (all  $p < 0.0001$ ) using two-tailed paired t-test for SM-netFusion-NAGFS, and SM-netFusion-SNF pairs for M-LH, M-RH, F-LH and F-RH datasets.

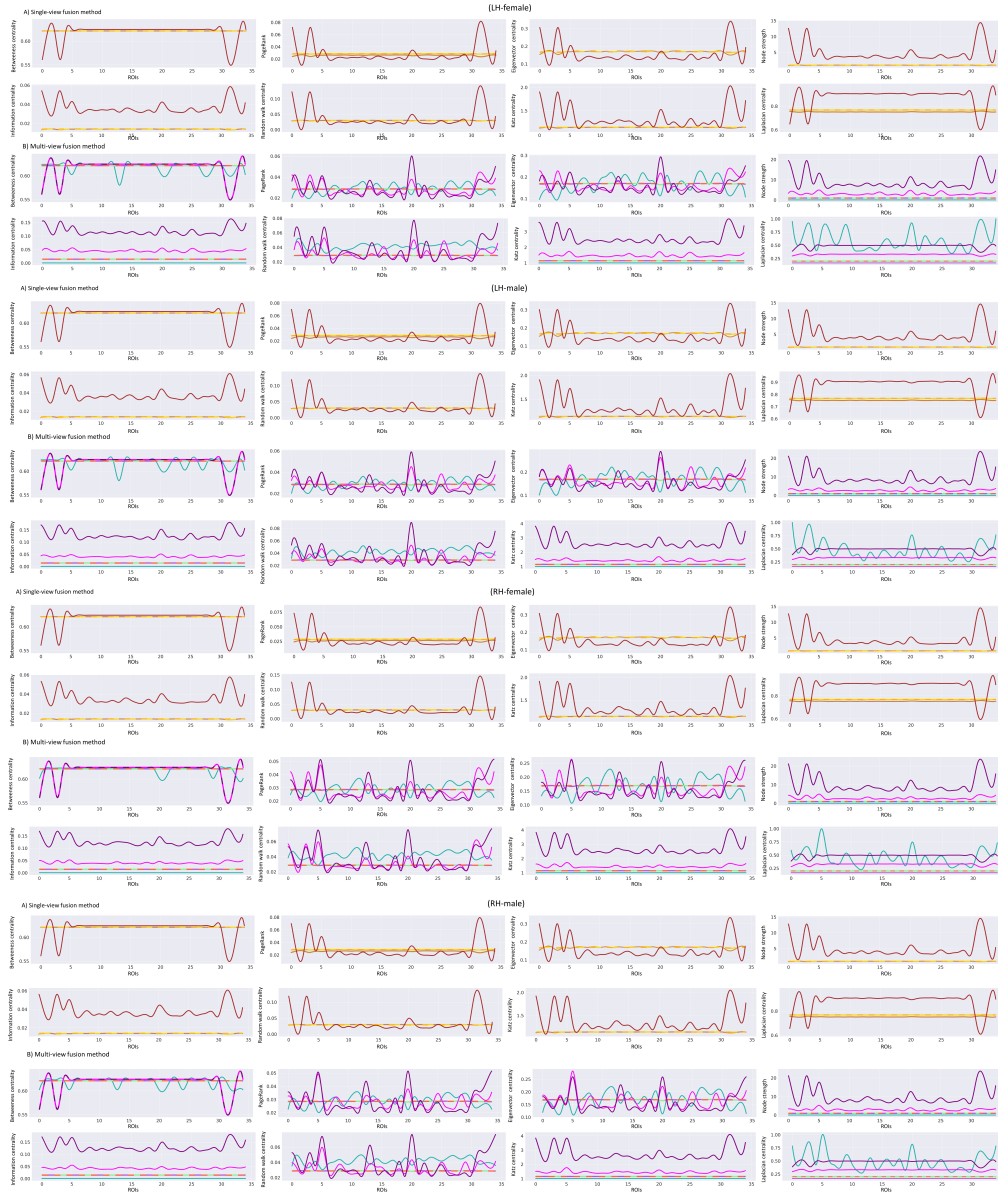


**Figure A.2 :** Comparison of the average topological distributions across 5-fold cross-validation of PageRank [12], Katz centrality [13], node strength [14], random-walk centrality [15], information centrality [16], Laplacian centrality [17], eigenvector centrality [18], and betweenness centrality [19] of templates generated by **A)** SNF [1], NAG-FS [7], and SM-netFusion [8] against the ground truth distribution for a population of single-view network; and **B)** netNorm [2], SCA [9], MVCF-Net [10], cMGI-Net [20], and DGN [11] against the ground truth distribution for a population of multi-view network for M and F datasets in the left and right hemispheres.

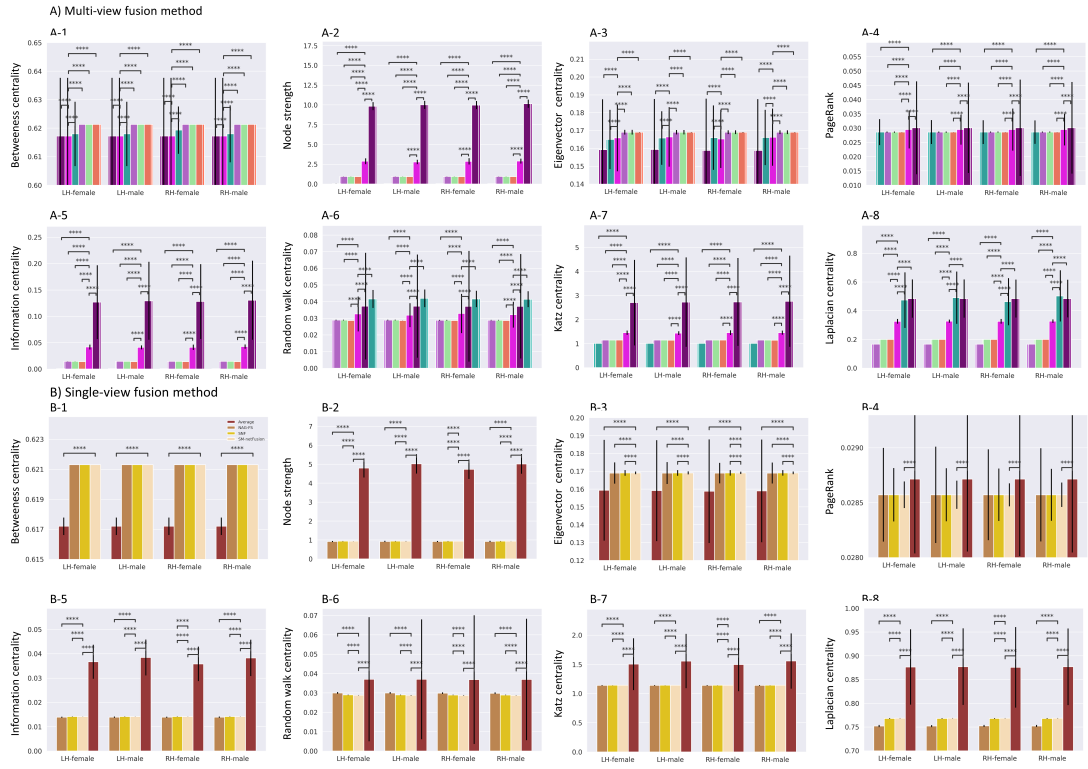


**Figure A.3 :** This chart displays the average topological distributions of PageRank [12], Katz centrality [13], node strength [14], random-walk centrality [15], information centrality [16], Laplacian centrality [17], eigenvector centrality [18], and betweenness centrality [19] measures across the nodes (ROIs) of the learned templates generated by **A)** SNF [1], NAG-FS [7], and SM-netFusion [8] against the ground truth distribution of a population of single-view networks; and **B)** netNorm [2], SCA [9], MVCF-Net [10], cMGI-Net [20], and DGN [11] against the ground truth distribution of a population of multi-view network for the M and F datasets in the left and right hemispheres. For multi-graph fusion methods comparison, DGN achieved the highest average distribution comparing to the average RH distribution of other multigraph fusion methods with a high statistical significance demonstrated by a two-tailed paired t-test (all  $p < 0.0001$ ) for DGN-SCA, DGN-netNorm, DGN-MVCFNet, and DGN-cMGI-Net pairs for M (LH), M (RH), F (LH) and F (RH) groups, except for the random-walk centrality measures. For single-view fusion methods comparison, SM-netFusion significantly achieved the maximum average distribution comparing to SNF and NAG-FS for all centrality measures except the betweenness centrality and node strength for M (LH), M (RH), F (LH) and F (RH) datasets.

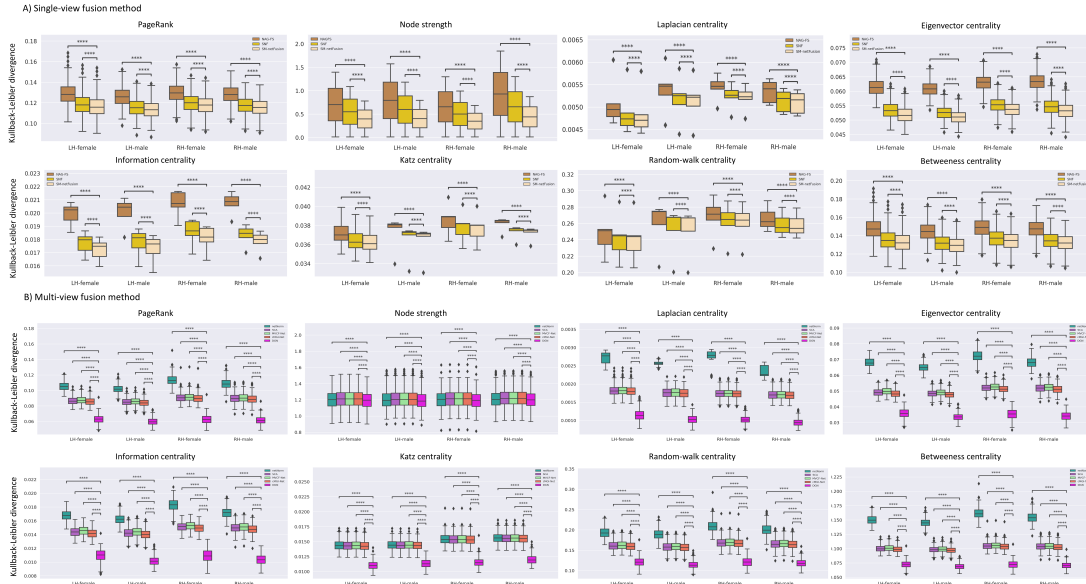


**Figure A.4 :** Average of Kullback-Liebler divergence distribution across 5-fold cross validation between the ground truth distribution and the average topological distributions of the learned connectional templates generated by **A)** single-view fusion methods (SNF [1], NAG-FS [7], and SM-netFusion [8]); and **B)** multigraph fusion methods (SCA [9], netNorm [2], MVCF-Net [10], cMGI-Net [20], and DGN [11]). The topological measures include PageRank [12], Katz centrality [13], node strength [14], random-walk centrality [15], information centrality [16], Laplacian centrality [17], eigenvector centrality [18], and betweenness centrality [19]. Charts illustrate that for multi-graph fusion methods comparison, DGN achieved the minimum mean KL-divergence distribution and the narrowest dispersion range with a high statistical significance demonstrated by a two-tailed paired t-test (all  $p < 0.0001$ ) for DGN-SCA, DGN-netNorm, DGN-MVCFNet, and DGN-cMGI-Net pairs for M-LH, M-RH, F-LH and F-RH groups. For single-view fusion methods comparison, SM-netFusion significantly achieved the lowest mean KL-divergence distribution to the population single-view networks (all  $p < 0.0001$ ) using two-tailed paired t-test for SM-netFusion-NAGFS, and SM-netFusion-SNF pairs for M-LH, M-RH, F-LH and F-RH datasets. [Box plot legend: median (midline), box (25th and 75th percentiles), and whiskers (extrema).]

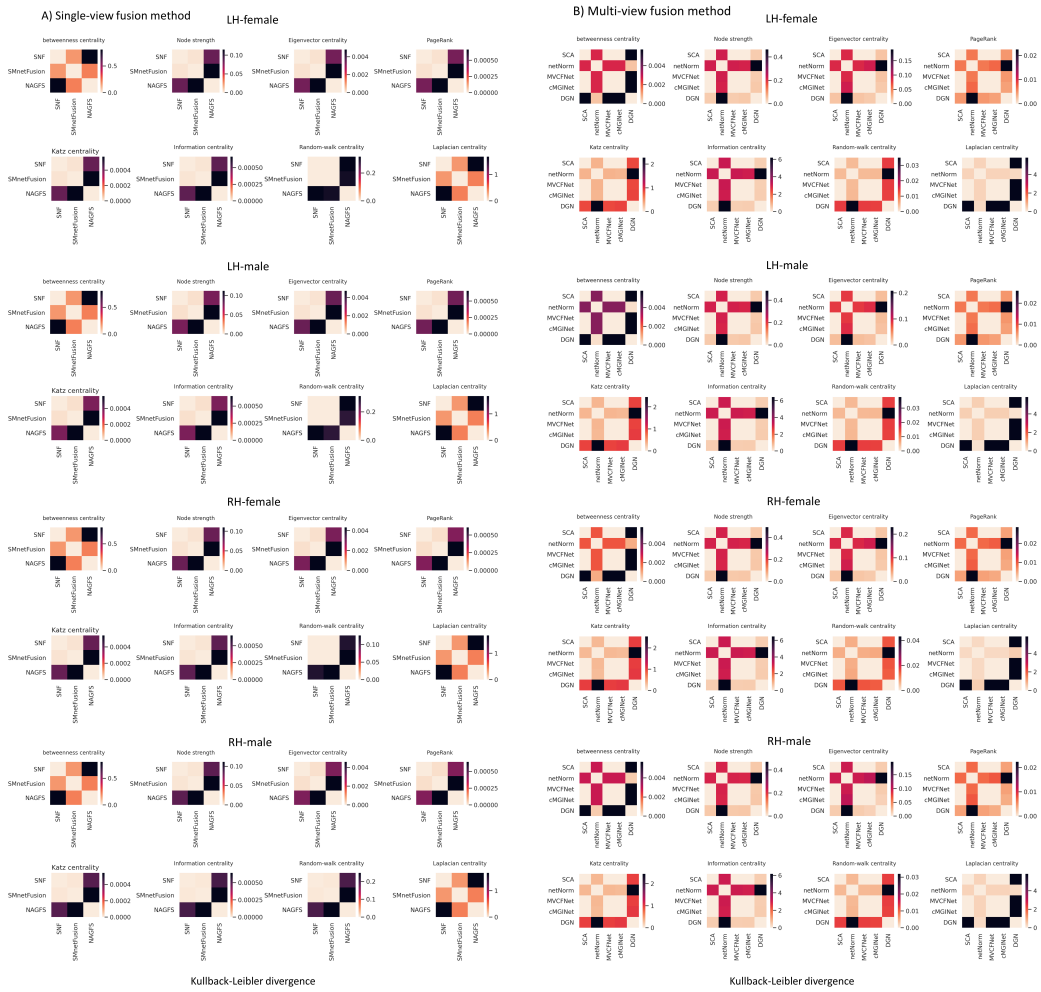


**Figure A.5 :** Dissimilarity between the possible pairs combination of **A)** single-view and **B)** multigraph fusion methods using KL-divergence for the M and F in the left and the right hemispheres.

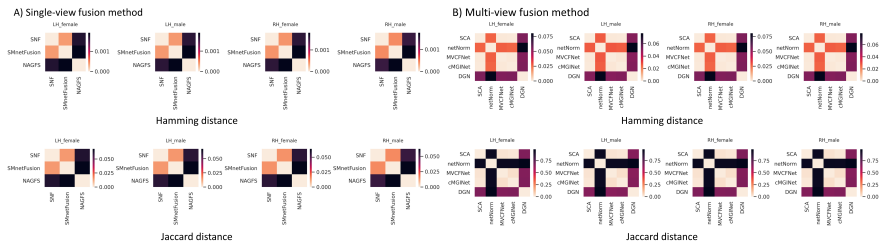


**Figure A.6 :** Pairwise distance comparison of the learned connective templates generated by **A)** single-view fusion methods (SNF [1], NAG-FS [7], and SM-netFusion [8]); and **B)** multigraph fusion methods (netNorm [2], SCA [9], MVCF-Net [10], cMGI-Net [20], and DGN [11]) using Hamming distance and Jaccard distance measures for M and F populations in the left and right hemispheres.

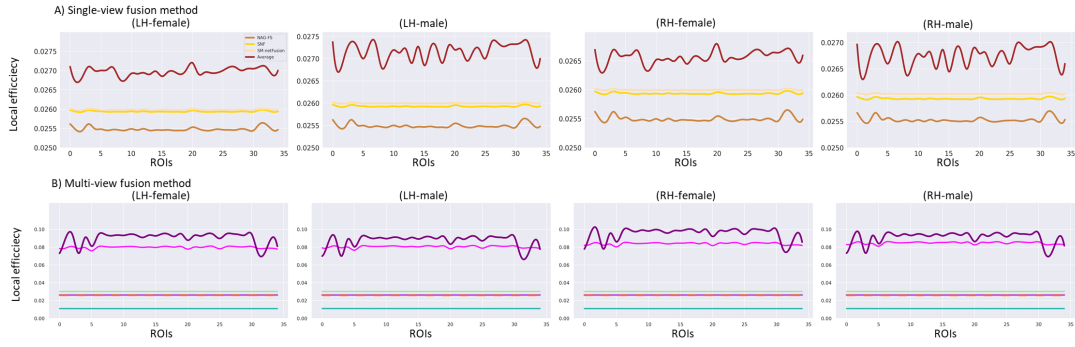


**Figure A.7 :** Region-wise local efficiency distribution of connectional brain templates generated by **A)** SNF [1], NAG-FS [7], and SM-netFusion [8] against the ground truth distribution for single-view fusion methods comparison; and **B)** netNorm [2], SCA [9], MVCF-Net [10], cMGI-Net [20], and DGN [11] against the ground truth for multi-graph integration methods using 5-fold cross-validation for the M and F populations in the left and right hemispheres. For multi-graph fusion methods comparison, DGN achieved the most similar distribution to the ground truth while SM-netFusion displayed the closest distribution.

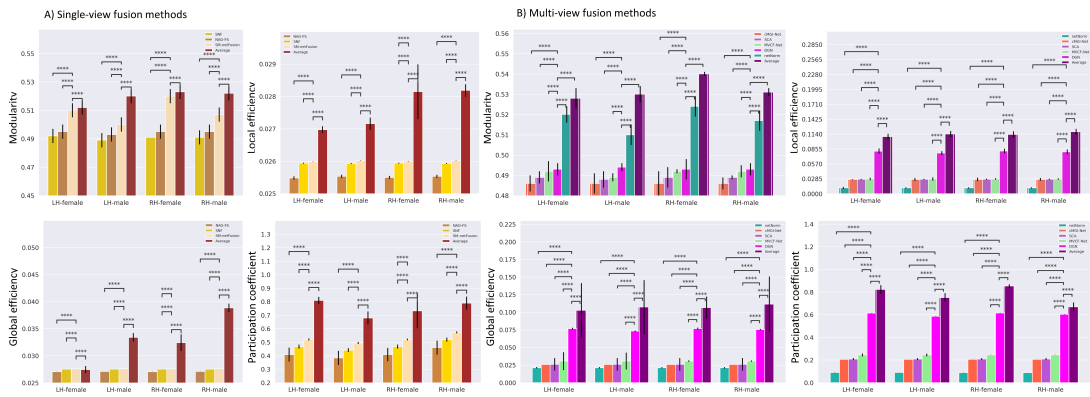


**Figure A.8 :** Charts display the average local efficiency distribution across regions (ROIs), modularity, global efficiency, and participation coefficient of connectional brain templates estimated by **A)** single-view fusion methods (SNF [1], NAG-FS [7], and SM-netFusion [8]) and **B)** multigraph fusion methods (netNorm [2], SCA [9], MVCF-Net [10], cMGI-Net [20], and DGN [11]) against the ground truth for M-LH, F-LH, M-RH, and F-RH groups using 5-fold cross validation. Remarkably, DGN achieved the highest scores including average local efficiency distribution over regions, modularity, participation coefficient, and global efficiency comparing to other multigraph fusion methods with a high statistical significance demonstrated by a two-tailed paired t-test (all  $p < 0.0001$ ) for DGN-SCA, DGN-netNorm, DGN-MVCFNet, and DGN-cMGI-Net pairs for M-LH, M-RH, F-LH and F-RH groups. While for the single-view integration methods comparison, SM-netFusion significantly outperformed SNF and NAG-FS for M and F datasets in both hemispheres (all  $p < 0.0001$ ).

## CURRICULUM VITAE

**Name Surname** : Nada CHAARI

### EDUCATION

- **Ph.D.** : 2021, Istanbul Technical University, Faculty of Management Engineering, Department of Management Engineering
- **B.Sc.** : 2016, National Engineering School of Tunis, Department of Industrial Engineering

### PUBLICATIONS, PRESENTATIONS AND PATENTS ON THE THESIS:

- **Chaari, N., Camgöz Akdağ, H., Rekik, I.** 2021. Estimation of gender-specific connectional brain templates using joint multi-view cortical morphological network integration. *Brain Imaging and Behavior*, 15(4), 2081-2100. **(Published)**
- **Chaari, N., Gharsallaoui, M. A., Camgöz Akdağ, H., Rekik, I.** 2021. Multigraph Classification using Learnable Integration Network with Application to Gender Fingerprinting. *Neural Networks*. **(Submitted)**
- **Chaari, N., Camgöz Akdağ, H., Rekik, I.** 2021. Comparative Study of Connectional Brain Templates in Network Neuroscience. **(Ready for submission)**